DEVELOPMENT OF A RADIATIVE TRANSPORT BASED, FLUORESCENCE-ENHANCED, FREQUENCY-DOMAIN SMALL ANIMAL IMAGING SYSTEM

A Dissertation

by

JOHN C. RASMUSSEN

Submitted to the Office of Graduate Studies of
Texas A&M University
in partial fulfillment of the requirements for the degree of

DOCTOR OF PHILOSOPHY

December 2006

Major Subject: Chemical Engineering

DEVELOPMENT OF A RADIATIVE TRANSPORT BASED, FLUORESCENCE-ENHANCED, FREQUENCY-DOMAIN SMALL ANIMAL IMAGING SYSTEM

A Dissertation

by

JOHN C. RASMUSSEN

Submitted to the Office of Graduate Studies of
Texas A&M University
in partial fulfillment of the requirements for the degree of

DOCTOR OF PHILOSOPHY

Approved by:

Chair of Committee,	Eva M. Sevick-Muraca
Committee Members,	Michael A. Bevan
	Daniel F. Shantz
	Gerard L. Coté
Head of Department,	N. K. Anand

December 2006

Major Subject: Chemical Engineering

ABSTRACT

Development of a Radiative Transport Based, Fluorescence-Enhanced,
Frequency-Domain Small Animal Imaging System. (December 2006)
John C. Rasmussen, B.S., University of Oklahoma
Chair of Advisory Committee: Dr. Eva M. Sevick-Muraca

Herein we present the development of a fluorescence-enhanced, frequency-domain radiative transport reconstruction system designed for small animal optical tomography. The system includes a time-dependent data acquisition instrument, a radiative transport based forward model for prediction of time-dependent propagation of photons in small, non-diffuse volumes, and an algorithm which utilizes the forward model to reconstruct fluorescent yields from air/tissue boundary measurements.

The major components of the instrumentation include a charge coupled device camera, an image intensifier, signal generators, and an optical switch. Time-dependent data were obtained in the frequency-domain using homodyne techniques on phantoms with 0.2% to 3% intralipid solutions.

Through collaboration with Transpire, Inc., a fluorescence-enhanced, frequency-domain, radiative transport equation (RTE) solver was developed. This solver incorporates the discrete ordinates, source iteration with diffusion synthetic acceleration, and linear discontinuous finite element differencing schemes, to predict accurately the fluence of excitation and emission photons in diffuse and transport limited systems. Additional techniques such as the first scattered distributed source method and integral

transport theory are used to model the numerical apertures of fiber optic sources and detectors.

The accuracy of the RTE solver was validated against diffusion and Monte Carlo predictions and experimental data. The comparisons were favorable in both the diffusion and transport limits, with average errors of the RTE predictions, as compared to experimental data, typically being less than 8% in amplitude and 7% in phase. These average errors are similar to those of the Monte Carlo and diffusion predictions.

Synthetic data from a virtual mouse were used to demonstrate the feasibility of using the RTE solver for reconstructing fluorescent heterogeneities in small, non-diffuse volumes. The current version of the RTE solver limits the reconstruction to one iteration and the reconstruction of marginally diffuse, frequency-domain experimental data using RTE was not successful. Multiple iterations using a diffusion solver successfully reconstructed the fluorescent heterogeneities, indicating that, when available, multiple iterations of the RTE based solver should also reconstruct the heterogeneities.

DEDICATION

To Jennifer and the kids

ACKNOWLEDGEMENTS

Throughout the past few years, many people have had an important impact on my life and the progress of this dissertation. First, I would like to thank my advisor, Dr. Eva M. Sevick-Muraca who has always believed in me and my potential. She has encouraged me to explore many research areas in the Photon Migration Laboratories and allowed me attend multiple short courses, professional conferences, and other meetings which have broadened my understanding of molecular imaging and the possibilities it presents as a diagnostic and therapeutic tool. Eva has always been a wonderful example of boundless optimism and professional and ethical conduct in the face of daunting odds.

I would also like to thank Dr. Amit Joshi for his valuable comments and contributions throughout the duration of this study. I particularly thank him for his efforts in the development of reconstruction techniques which implemented the instrumentation and forward algorithm presented herein. Thanks also to Todd Wareing, John McGhee, and Greg Failla of Transpire Inc. who were intrigued when we first contacted them about adapting their radiative transport solver, Atilla®, for use in fluorescence imaging. They spent many hours modifying and developing code with no guarantee of compensation for their time and effort. Without them, this dissertation would not have been possible. I would also like to thank Dr. Tianshu Pan for developing the Monte Carlo code and patiently producing the various Monte Carlo simulations presented throughout this dissertation.

I would also like to thank past and present members of my committee including, Drs. Michael Bevan, David Ford, Lihong Wang, Daniel Shantz, and Gerard Coté for

their support and suggestions during this research. I also thank Dr. Tahir Cagin for agreeing to be a substitute committee member during my final defense.

I also thank all the past and present members of the Photon Migration Laboratories for their friendships and support through the past few years. I have learned from everyone of them and value their diverse perspectives on both life and science. I particularly thank Drs. Kristen Adams and Sarabjoyt Dali for their help in proofing this document.

I am also sincerely grateful for my wife, Jennifer, for her unwavering love and support throughout this process. She has always believed in me even when there seemed to be no end in sight. Thanks also to my wonderful children, Jessica, Jacob, and Jared. Lastly, I would like to thank my parents for their love and support throughout the years, without them I would not be the person I am today.

NOMENCLATURE

Abbreviations

ART	Algebraic Reconstruction techniques
ATP	Adenosine triphosphate
CCD	Charge coupled device
CT	Computed tomography
CW	Continuous wave
DSA	Diffuse synthetic acceleration
FD	Frequency domain
FDA	Food and Drug Administration
FFT	Fast Fourier transform
ICCD	Intensified charge coupled device
ICG	Indocyanine green
LD	Linear discontinuous
MOBIIR	Model based-iterative image reconstruction
MRI	Magnetic Resonance Imaging
NIR	Near infrared
PET	Positron emission tomography
PMT	Photomultiplier tube
RF	Radio frequency

RTE	Radiative transport equation
SPECT	Single photon emission computed tomography
TD	Time domain

Alphanumeric symbols

c	Speed of light
D	Diffusion coefficient
e^-	Electron
E, E'	Energy
f	Unknown attenuation properties in Radon function (ART)
$\overline{F}$	Set of pixels (ART)
g	Anisotropy
H	Initial guess in ART
H	Transport operator
H_D	Diffusion transport operator
I	Number of nodes in a grid (mesh)
I_{AC}	Amplitude intensity
I_{DC}	Average amplitude intensity
J	Jacobian matrix
J	Matrix of weight factors (ART)
j	Square root of -1

m	Emission (subscript or superscript)
m	Neutron mass
m	Number of unknowns (ART)
M	Total number of source iterations
n	Neutron density
n	Number of source detector pairs (ART)
N	Total number of discrete ordinate angles
p	Photon
P	Probability (Monte Carlo)
P	Radon function (ART)
P^*	Set of all projection data (ART)
P_l	Legendre polynomial
P_n	Scattering order in RTE solver
r	Position vector
R_m	Correction term in DSA method
s	Step size (Monte Carlo)
S, s	Source term
t	Time
v	Neutron speed
w_n	Weight
x	Excitation (subscript or superscript)
x	Position along x axis

Xe^-	Multiplied electrons
x_i	Not sure
y	Position along y axis
z	Position along z axis

Greek symbols

Δ_i	
μ_{ax}	Absorption coefficient
$\mu_{ax,f}$	Absorption coefficient of fluorophore
θ	Angle
Φ_i	Angle integrated flux (diffusion)
$\tilde{\phi}$	Angular photon fluence
φ	Azimuthal angle (Monte Carlo)
θ	Deflection angle (Monte Carlo)
$\hat{\Omega}$	Direction of travel
μ	Discrete ordinate angle
τ	Fluorophore lifetime
ω	Frequency
γ	Index of refraction mismatch parameter
μ_s'	Isotropic scattering coefficient

δ_{ij}	Kroneker delta
μ	Optical property being reconstructed (ART)
θ	Phase
Ψ	Photon fluence
ϕ_l	Polynomial
ϕ	Quadrature formula
ε	Quantum efficiency of fluorophore
ξ	Random number (Monte Carlo)
ζ	Random number (Monte Carlo)
ϕ	Scalar (angle integrated) photon flux
μ_s	Scattering coefficient
σ_s	Scattering cross section
Σ_s	Scattering cross section
σ_l	Scattering moment
μ_t	Sum of scattering and absorption coefficients
σ_t	Total cross section
Σ_t	Total cross section
λ	Wavelength

TABLE OF CONTENTS

Page

Page

LIST OF FIGURES

FIGURE Page

FIGURE Page

FIGURE Page

LIST OF TABLES

I. INTRODUCTION

Recently individualized medicine has been promised and achieved using molecularly targeted cancer therapies. These therapies, such as Genentech's Herceptin®, Novarti's Gleevac®, and Imclone's Erbitux®, target cancer cells that over express an epitope not common in normal tissues. The future of individualized molecular medicine depends upon finding disease mechanisms and markers for designing diagnostic and therapeutic agents that specifically target diseased tissues and avoid normal tissues.

The time and money that must be devoted to each potential molecular drug is staggering. According to a report done by Bain & Company in 2003, the total cost to discover, develop, and market one successful drug reached $1.7 billion after taking into account the resources spent on unsuccessful compounds.[1] A large portion of this cost is spent in pre-clinical (animal) trials mandated by the Food and Drug Administration (FDA). Prior to gaining approval from the FDA, each drug candidate must go through extensive testing to determine its *in vivo* pharmacological properties, including its therapeutic value, toxicity, and pharmacokinetic distribution throughout the body. The compound must effectively treat the targeted malady without undue toxicity to normal tissue. The byproducts formed as the drug is metabolized must also be identified and the movement of the drug and its metabolites through the body tracked.

This dissertation follows the style of Medical Physics.

Currently, the bulk of agent discovery research is performed on small animals such as mice and rats. To obtain pharmacokinetic information, a statistically significant number of small animals must be sacrificed at specific time periods after the compound has been administered in order to access biodistribution. The cadaver is frozen and processed using histological techniques and, in many cases, chemical methodologies such as high performance liquid chromatography (HPLC) are needed to determine the location and concentration of the compound in the tissue. These techniques are costly in time, money, and animal life, especially since the majority of compounds do not make it out of animal testing.

To counter the ever increasing costs, new approaches to obtaining pharmacological data are being researched. One area of great interest is small animal imaging to dynamically track the distribution of agents *in vivo*. Many imaging modalities, such as x-ray computed tomography (CT), magnetic resonance imaging (MRI), ultrasound, and nuclear imaging, which were originally developed for use on humans are being produced in sizes convenient for imaging small animals. However, of these established modalities, only nuclear imaging has the sensitivity needed to provide information at the level required for molecular imaging. Nuclear techniques require the radiolabeling of compounds and the tomographic reconstruction of their emissions to provide a 3-D image of the biodistribution of the radioisotope. Another modality, optical tomographic imaging, has been proposed and is in the developmental stages. This modality uses a near infrared (NIR) fluorophore to create a signal and takes advantage of the low absorptive properties of tissues in the NIR portion (750-

900 nm) of the electromagnetic spectrum to tomographically reconstruct the biodistribution of a labeled drug candidate.

Optical tomography has the potential for molecular resolution, meaning that the location of a fluorophore can be identified by determining the source of its fluorescence emission. Using this principle, investigative drugs may be conjugated to a NIR fluorophore and administered to the small animal. Excitation light is used to excite the fluorophore and the resulting emission light can be detected. Using tomographic reconstruction techniques, the origin of the fluorescence can be determined, thus providing a new method for tracing the movement of the investigative drug in the body. While the presence of the conjugated fluorophore may impact the pharmacokinetics of the investigative drug, targeting NIR conjugates may be useful in assessing changes in the therapeutic disease target in response to the new drug as suggested by the studies of Kwon *et al*.[2] Optical tomography may ultimately reduce the loss of animal life and time spent on histological studies resulting in lower development costs and quicker development times for molecular diagnostic and therapeutic agents. A brief introduction to those imaging modalities now used and/or being developed for small animal imaging is presented below.

Small Animal Tomography

There are many imaging systems currently available or under development that enable the tomographic reconstruction of small animals. These include x-ray CT,[3, 4] MRI,[5, 6] ultrasound,[7] nuclear imaging,[8-11] and optical imaging.[12, 13] However, many of these modalities (i.e. CT, MRI, and ultrasound) only reflect structural or functional

differences and are not sensitive enough to provide needed information for molecular imaging due to the high concentration (typically milli-molars) of contrast agent needed. While some MRI contrast agents such as mono-crystalline iron oxide nano-compounds may be used in nano-molar concentrations, only nuclear and optical imaging require contrast agent concentrations to be on the order of pico-molars with sufficient sensitivity to provide information at the molecular level. In the case of nuclear imaging, the photon detected is a result of a nuclear decay process at the atomic level; in optical imaging the photons detected originate from the relaxation of fluorescent molecules or generation of luminescent photons from photochemical reactions. The capacity to obtain molecular information is also enhanced by the ability to conjugate the respective molecular (nuclear and/or optical) probes to targeting antibodies or proteins which preferentially bind to disease markers within the body.[14-17] Research is underway to combine nuclear and/or optical molecular imaging techniques with CT, MRI, or ultrasound in order to obtain molecular and structural information simultaneously.[18-20]

Nuclear Imaging

There are several different nuclear imaging modalities commonly used on small animals. The simplest uses a gamma camera to detect the gamma-ray photons emitted when a radioisotope decays. A gamma camera consists of an array of collimators, a scintillation crystal, and an array of photomultiplier tubes (PMT). The collimators permit rays traveling in the desired direction to hit the scintillation crystal. When the gamma ray interacts with the crystal a burst of light is produced which is

detected by the PMT's. One of the advantages of nuclear imaging is the ability to image deep tissues due to the relatively low attenuation of the high energy photons by tissues. Also, as an established procedure, the instruments and supplies are readily available and the techniques are well known. Many carrier agents have been developed which allow the researcher to target specific organs in the body. However, scintigraphy images are of low spatial resolution (2-D) and gamma ray emitting materials (Technetium 99m being the most common) also have a half life associated with them, thus once the atom has emitted a single photon, it can no longer provide useful information. Figure 1 shows a nuclear image of a mouse imaged at M.D. Anderson Cancer Clinic (MDACC) using a gamma camera with a medium energy collimator. The exposure time was fifteen minutes, 24 hours after the administration of a radioisotope labeled RGD-IRDye800 contrast agent.

Another type of gamma imaging is single photon emission computed tomography (SPECT). SPECT uses multiple gamma cameras to collect gamma rays at different angles (projections) around the animal. Filtered backprojection algorithms

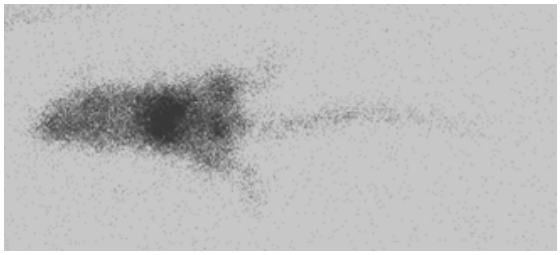

Figure 1: Gamma image of a mouse (15 minute exposure time) 24 hours post administration of radioisotope labeled RGD-IRDye800 contrast agent. (Courtesy of Jessica Houston)

similar to those used in x-ray computed tomography are used to reconstruct the data in two or three dimensions.

The third modality of nuclear imaging is positron emission tomography (PET). In this modality, a radioisotope that emits a positron (beta particle) is used. Almost immediately after the positron is emitted, it interacts with a nearby electron and they annihilate to produce two photons (gamma rays) traveling 180° from each other. If both photons are detected near simultaneously, then the event is recorded in the projection data. After sufficient photon counts are detected, filtered backprojection algorithms are used to reconstruct the data in two or three dimensions.

Optical Imaging

In optical tomography, near-infrared light (750-900 nm) is typically used as the means to probe deep, clinically relevant tissue volumes. In this range, the absorption of light is minimized in tissue, as shown in Figure 2, and the light can propagate through several centimeters of tissue before it is extinguished. The propagation of light through tissue is governed by the optical scattering and absorption properties, and optical tomography is based on the variation or contrast of these properties in tissues. Some researchers have developed the instrumentation and algorithms necessary to reconstruct the endogenous or inherent distribution of optical properties in tissues for applications such as assessing tissue perfusion and oxygenation.[21-23] However, for molecular imaging, a contrast agent must be introduced into the tissue such that molecular events can be detected. The two most common methods used to detect optical contrast agents in small animals are bioluminescence and fluorescence.

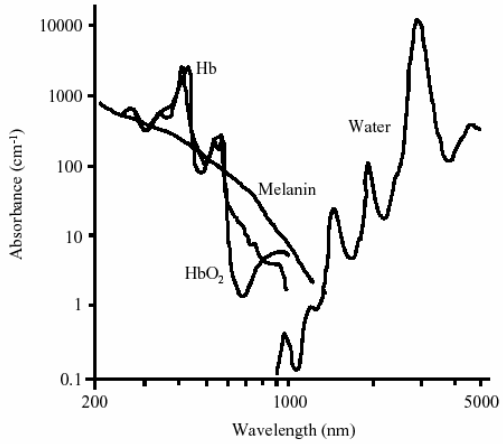

Figure 2: Absorbance spectra of common components of the body. (adapted from Lim and Soter[24])

Bioluminescence involves the generation of light as a byproduct of a chemical reaction within an organism; a well known example is the glow produced by fireflies. As will be discussed in more detail below, to obtain bioluminescence from a small animal, the required chemicals must be introduced into the mouse. Typically this involves modifying its DNA such that it expresses the enzyme required for the reaction to occur. When bioluminescence is desired, the mouse is injected with the chemical substrate and when the substrate and enzyme react, light is released. The emitted signal is very weak and absolute darkness is required for detection. To date, the use of bioluminescence imaging has largely been limited to planar imaging; however research is underway to develop reconstruction algorithms for bioluminescent tomography.[25]

The most common way of introducing exogenous contrast is through the use of fluorescence. Fluorescence photons are produced by fluorescent molecules through a

process by which an excitation photon is absorbed and subsequently reemitted at a lower energy or color. Data collected at both the excitation and emission wavelengths as well as the time lag due to the radiative lifetime of the fluorophore provide ample information for tomographic reconstruction. Because of the multiply scattered nature of the detected light, backprojection techniques commonly used in nuclear imaging have limited applicability and, as will be discussed later, more complex reconstruction algorithms are required. Originally developed for large tissue volumes, fluorescence optical imaging is being investigated as a means to assess the biodistribution and efficacy of drugs *in vivo* in small animals. This dissertation addresses the development of the instrumentation and associated algorithms needed for the adaptation of optical tomography to small animal tomography.

Organization of Dissertation

In this dissertation we seek to develop and assess the instrumentation and algorithms required for tomographic reconstruction in small animals. The central aims include the: (i) development of a time-dependent, radiative transport based forward model of light propagation in small animals (in collaboration with Transpire, Inc.), (ii) validation of the RTE forward model against the accepted diffusion and Monte Carlo models, (iii) development of instrumentation suitable for experimental validation of the RTE forward model, (iv) adaptation of instrumentation for small animal optical tomography, and (v) actual reconstruction of targets from experimental data using a reconstruction algorithm developed in the Division of Molecular Imaging at Baylor

College of Medicine. This dissertation is organized into sections as detailed in Figure 3.

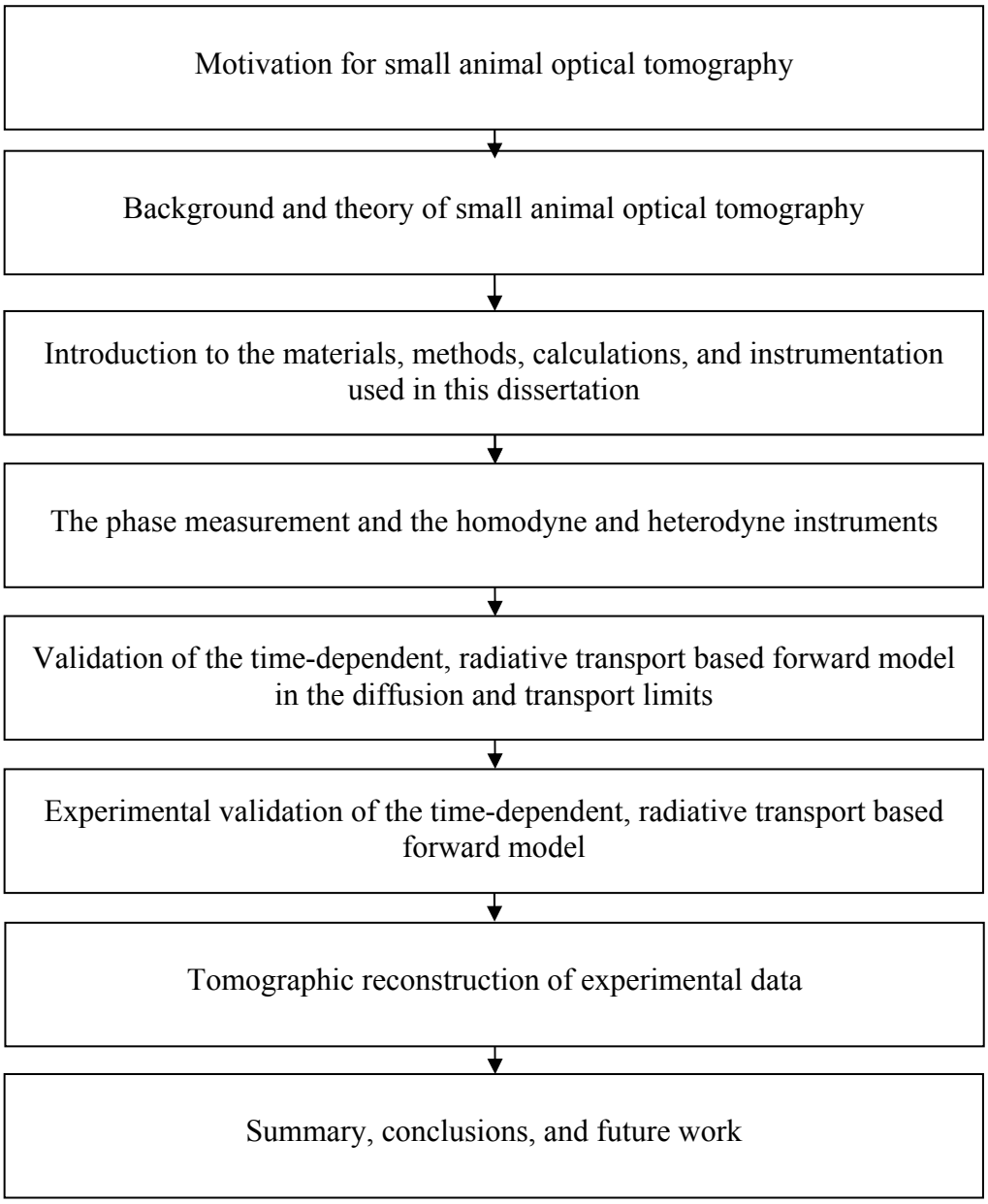

Figure 3: Organization of the dissertation.

II. BACKGROUND AND THEORY

This section provides the background information of the basis of small animal optical tomography including the nature and propagation of light, the optical properties which provide reconstructable contrast in tissues, the types of optical instrumentation commonly used to interrogate tissue, the methods commonly used to model light propagation in tissues, and the basic algorithms used for image reconstruction. A table detailing the current state of the art of small animal optical tomography as indicated in the literature is also presented.

Nature of Light

Light is a form of electromagnetic radiation which possesses both wave and particle like characteristics.[26] An electromagnetic 'particle' or photon is a massless and chargeless packet of energy that propagates through space as a wave. Electromagnetic waves consist of an electrical component ($\vec{E}$) and a magnetic component ($\vec{M}$) that are interdependent and vary in time as shown in Figure 4. Electromagnetic radiation is classified according to its wavelength (λ) or the distance between its peaks. As illustrated in Figure 5, electromagnetic wavelengths range from radio waves ($\lambda > 1$ m) to gamma rays ($\lambda < 10^{-12}$ m) and include visible light which is the small portion of the spectrum detected by the human eye. The wavelength of the radiation is dependent on its energy (E) as described by $E = ch/\lambda$, where c is the speed of light in a vacuum (2.998×10^{10} cm/s) and h is Plank's constant (4.13566×10^{-15} eV/s). As the energy of the wave increases, the wavelength decreases and vice versa. The frequency of the wave is defined as the ratio of the speed of light and its

wavelength. When the field, $\vec{R}$, resulting from $\vec{E}$ and $\vec{M}$ is fixed in space, the wave is defined as linearly polarized. The speed of light in a medium is determined by the ratio c/n where n is the refractive index of the medium through which the light is propagating. For more detailed information about the nature of light, the reader is referred to Hecht.[26]

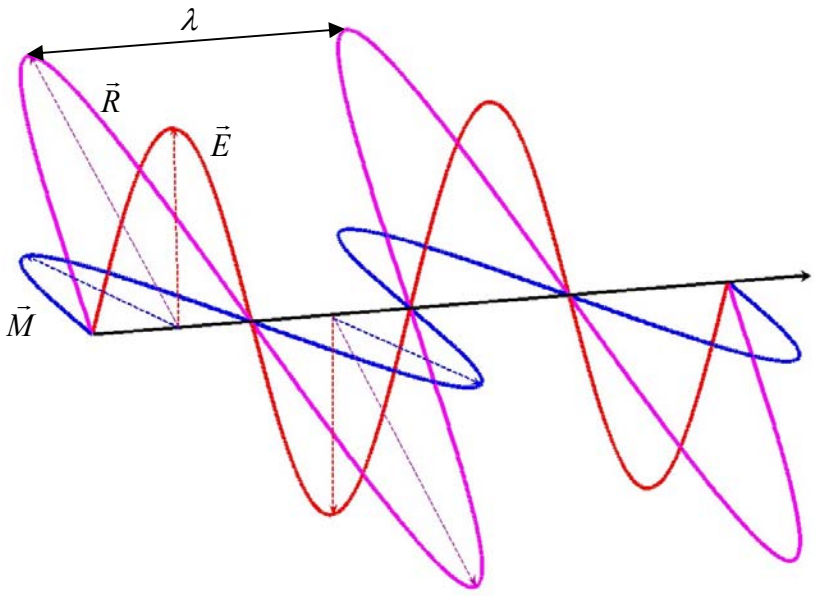

Figure 4: Schematic illustrating the wavelike propagation of electromagnetic radiation. $\vec{E}$ is the electric component, $\vec{M}$ is the magnetic component, and $\vec{R}$ is the resulting electromagnetic field.

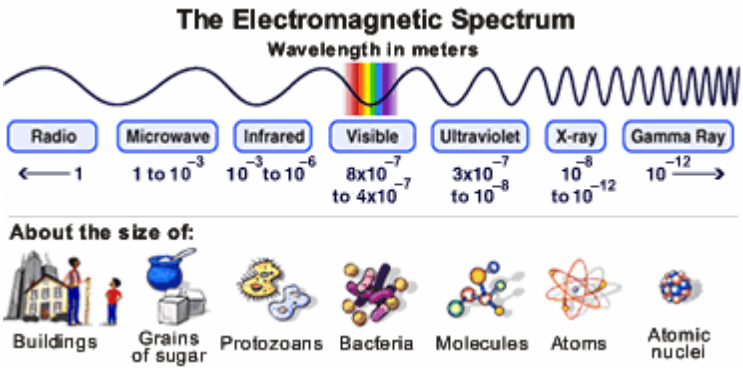

Figure 5: The electromagnetic spectrum. (reproduced with permission from http://hubblesite.org/reference_desk/faq/all.php.cat=light)

Propagation of Light

As light propagates, it interacts with the atoms and molecules it encounters. When a photon collides with a molecule, it is absorbed causing the molecule's electron cloud to enter a ground state vibration and then is immediately reemitted isotropically at the same wavelength and energy. This process is referred to as scattering and the amount of scatter is dependent on the photon's wavelength and the molecule's size. When molecules are in proximity to one another, the apparent direction of scatter depends on the cumulative interference of the scattered photon waves. If no apparent scatter occurs and the light continues to travel in the original direction it is called forward scattered, likewise if it seems to travel back the way it came, then it is back scattered. Absorption occurs when a photon absorbed by a molecule and converted to heat.

As light propagates through materials, the scattering and absorption of the molecules or particles cause the phase of the wave to shift, resulting in an apparent

change in the speed of the light. This effect is quantified by the refractive index (n) which is defined as the ratio of the speed of light in a vacuum and the apparent speed of light in the material. As light propagates from one type of material to another with a different refractive index, it refracts (enters into the second material), reflects (bounces of second medium back into the first medium) or both as shown in Figure 6. The angle of reflection is always equal to the angle of incidence, θ_1. The angle of refraction, θ_2, depends on the angle of incidence and the refractive indexes of the material as defined by Snell's Law below:

$$n_1 \sin\theta_1 = n_2 \sin\theta_2 \qquad \textbf{(1)}$$

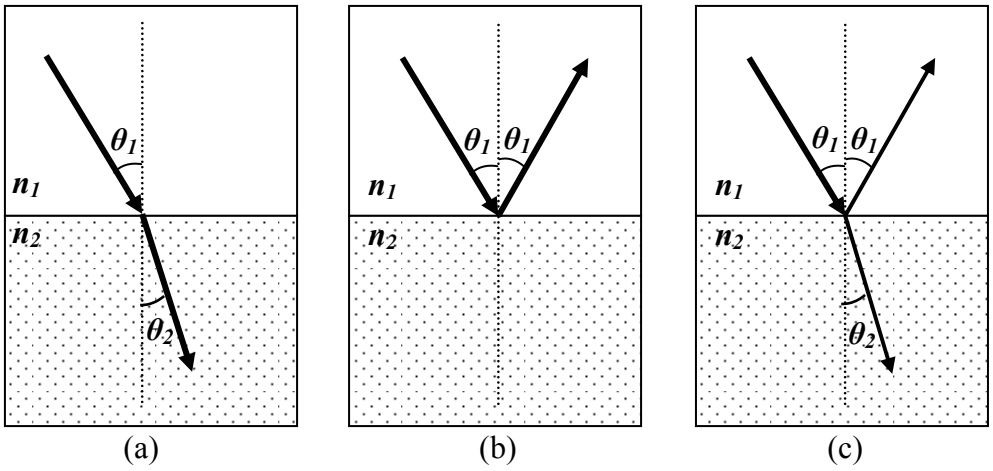

Figure 6: Refraction (a), reflection (b), and reflection and refraction (c) of light between two materials with differing indexes of refraction.

The cumulative propagation of light in tissues is quantified through its scattering coefficient (μ_s), anisotropy factor (g), and absorption coefficient (μ_a). As light propagates through tissue it encounters many sub-cellular structures with different indexes of refraction causing the light to scatter or change its direction of travel. The inverse of the mean distance a photon travels between scattering events is defined as the scattering coefficient. The average direction of scatter is quantified by the anisotropy factor, which is the mean of the cosine of the all the scattered angles ($g = \langle \cos\theta \rangle$). The isotropic scattering coefficient, μ_s', is related to μ_s by $\mu_s' = \mu_s(1-g)$ and describes the effective mean scatter path length if all the photons were scattered isotropically. The absorption coefficient is the inverse of the mean distance a photon travels before it is absorbed by chromophores present in the tissue.

Optical Contrast for Tomography

All forms of medical imaging rely on the contrast or dissimilarity between the region of interest and the surrounding or background tissues. In optical imaging the contrast is provided by endogenous or exogenous factors. Endogenous contrast arises from the scattering of light as it propagates through sub-cellular structures with inherently different refractive indexes and/or from the absorption of light due to chromophores within the cell.[27] The most commonly used endogenous contrast is that produced by the deoxygenation of hemoglobin in blood. As illustrated previously in Figure 2, the absorption of oxyhemoglobin and deoxyhemoglobin differ by an order of magnitude in the near-infrared region of their absorption spectra, and optical data has successfully been used to tomographically reconstruct the hemodynamics in rodent

brains,[22, 23] human foreheads,[21] and human breast.[28] Differences in scattering also impact the propagation of light through tissue, particularly where clear fluids act as voids in tissues. For example, Hielscher *et al.* investigated the differences in contrast in the fingers of a patient with rheumatoid arthritis.[29] In these cases the imaged contrast resulted when the healthy, clear synovial fluid in the joint turned to a grayish, turbid substance as the disease progressed.

Bioluminescence occurs when photons are released as a result of biochemical processes in tissues. In small animals, cells are genetically manipulated to express a 'reporter gene' which produces the enzyme luciferase. Exogenous luciferin, the 'reporter probe,' is then introduced into the mouse and, when in the presence of luciferase, oxidizes with adenosine triphosphate (ATP) and oxygen to produce light (~600 nm) as illustrated in Figure 7. Because the luciferin reacts only in the presence of luciferase, bioluminescent images typically have high signal to background ratios but low photon counts. Research utilizing bioluminescence techniques is increasing rapidly,[29-33] as yet however, tomography based on bioluminescence is largely undeveloped.[25]

Exogenous contrast involves the use of an agent, such as a fluorophore, that is introduced into the body. Unlike bioluminescence, the fluorescence process depends on the excitation of a molecule due to the absorption of a photon. When the molecule undergoes radiative relaxation it emits a photon at a lower energy (thus longer wavelength) as illustrated in the Jablonski diagram illustrated in Figure 8. Fluorescent

luciferin + luciferase + ATP →
luciferyl adenylate-luciferase + pyrophosphate

luciferyl adenylate-luciferase + O_2 →
oxyluciferin + luciferase + AMP + light

Figure 7: Pathway of a photochemical reaction commonly used in bioluminescent studies.

probes do not have a half life associated with them and can theoretically emit up to 10^{10} more photons per second than similar concentrations of a radioisotope.[30] The time lag between absorption and emission or lifetime associated with the fluorescence process also provides additional contrast which may be used in the tomographic reconstruction of fluorophore concentration. Fluorophores can also be conjugated to proteins or antibodies providing opportunities to specifically bind to markers often overexpressed on diseased tissues.[14-16]

Auto-fluorescence is fluorescence due to naturally occurring fluorophores in the animal or its food and can be a major source of noise, particularly at visible wavelengths. Another significant source of noise in fluorescence imaging is excitation light leakage through the optical filters.[31]

Despite a lower signal to noise ratio as compared to bioluminescence, fluorescence imaging is rapidly expanding in popularity and application, due in part to of the ability to obtain or synthesize fluorophores across the entire visible spectrum and into the near infrared. NIR dyes are particularly useful because their excitation

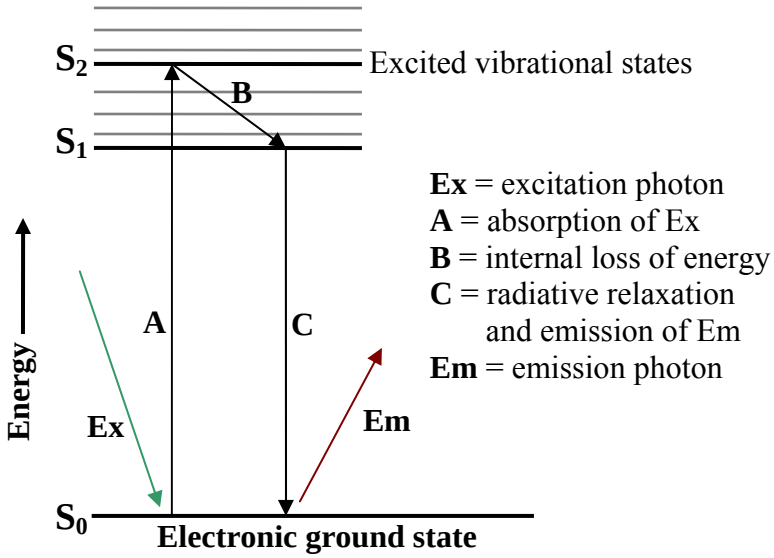

Figure 8: Schematic of a Jablonski diagram illustrating the fluorescence process.

and emission wavelengths generally do not produce large autofluorescence signals and tend to lie in the low absorption portion of the tissue spectra such that deep tissue penetration is possible.

These properties make fluorescence enhanced optical tomography a potentially powerful tool in determining the biodistribution of drug candidates *in vivo*, however due to the scattered nature of light propagation in tissues, the tomographic reconstruction of optical signals often require more complex algorithms than nuclear imaging.

Imaging Instrumentation

The instrumentation used in optical imaging can be split into three basic groups as defined by the nature of the light source: (i) continuous wave (CW) with a steady state light, (ii) time-domain (TD) with pulsed light, and (iii) frequency-domain

(FD) with intensity modulated light. Figure 9 illustrates the type of input signal each of these three types of light sources would introduce to the sample as well as the type of signal one would detect. FD and TD techniques provide data with time of flight information which proves particularly useful in tomographic reconstructions. With the exception of the signal generators required to modulate the light source and detector, the actual instrumentation is similar for CW and FD. TD techniques however seek to count individual photons based on their arrival time and, as such, require more sophisticated instruments as opposed to CW or FD which do not rely on time gating or single photon counting techniques. However, TD and FD techniques ultimately provide the same information, and one can use fast Fourier transform (FFT) techniques to go from the time to the frequency domain and vice versa. Optical tomography generally uses iterative algorithms to obtain 3-D reconstructions from data acquired from one of the three detection techniques.

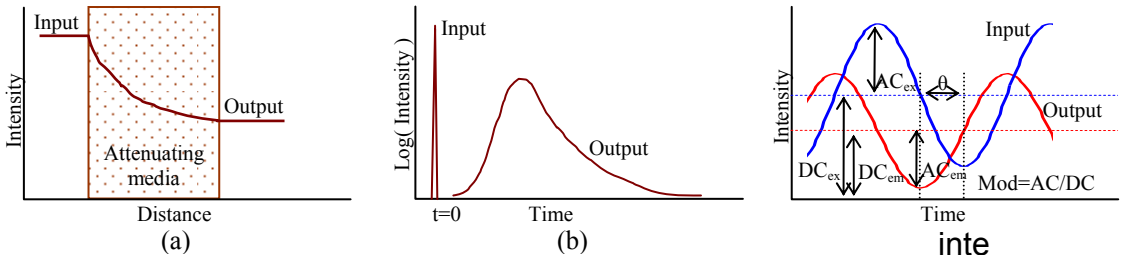

Figure 9: Examples of type of input signal for (a) continuous wave or steady state, (b) time-domain, and (c) frequency-domain imaging and the corresponding output signal acquired**.**

Forward Models of Light Propagation

Radiative Transport Equation

The general Boltzmann transport equation, or, as more commonly known in the optics community, the radiative transport equation (RTE) is a balance equation describing the propagation of energetic particles (such as neutrons and photons) in a system. The derivation of this equation is treated in detail by Duderstadt and Hamilton[32] and will not be discussed here. Therein the RTE is derived specifically for neutron transport in nuclear reactors, but it is analogous to any radiative transport process including optical photons. The formulation is shown below in the notation of Duderstadt and Hamilton.[32]

$$\frac{\partial n\left(\vec{r},E,\hat{\Omega},t\right)}{\partial t}+v\hat{\Omega}\cdot\nabla n\left(\vec{r},E,\hat{\Omega},t\right)+v\sigma_t\left(\vec{r}\right)n\left(\vec{r},E,\hat{\Omega},t\right)= \int_{4\pi}d\hat{\Omega}'\int_0^{\infty}dE'v'\sigma_s\left(\vec{r},E'\rightarrow E,\hat{\Omega}'\rightarrow\hat{\Omega}\right)n\left(\vec{r},E',\hat{\Omega}',t\right)+s\left(\vec{r},E,\hat{\Omega},t\right) \quad \textbf{(2)}$$

Where $n\left(\vec{r},E,\hat{\Omega},t\right)$ is the angular neutron density at position $\vec{r}$ and energy E, moving in direction $\hat{\Omega}$ at time t; E' is the energy from which a neutron is scattered to energy E; $\hat{\Omega}'$ is the direction of motion from which a neutron is scattered into $\hat{\Omega}$; v is the speed ($v=\left(2E/m\right)^{1/2}$ where m is particle mass; σ_s is the scattering cross section; σ_t is the total cross section (scattering plus absorption); and s is the source term.

The terms on the left hand side of equation (2) account for (i) the change in the angular neutron density over time, (ii) the movement of neutrons across the system boundaries (often referred to as the streaming operator), and (iii) the attenuation of neutrons due to collisions (absorption and scattering). The terms on the right take into

account (i) the gain of neutrons at E and $\hat{\Omega}$ due to scatter from E' and $\hat{\Omega}'$ and (ii) the gain due to a neutron source.

Equation (2) is linear in the angular fluence and has seven independent variables ($\vec{r}(x,y,z),\theta,\phi,E,t$). Typically in reality, the cross sections are generally complex and, as such, the RTE has limited analytical solutions. Several numerical techniques have been developed to obtain accurate numerical solutions; to date, the most commonly used is the discrete ordinate (S_N) method. While discrete-ordinates specifically refers to the angular discretization method, it also commonly refers to a class of solvers that discretize the RTE in space (via finite-difference, finite-volume, or finite-element methods), angle (discrete-ordinates), and energy (or in optical tomography, the wavelength of light) thereby reducing the RTE to a set of linear equations which can be solved iteratively.[33] For brevity, a general description of these discretization methods is presented for the steady-state, within-group (single energy), 1-D RTE written as:

$$\mu\frac{\partial}{\partial x}\psi(x,\mu)+\sigma_t(x)\psi(x,\mu)=\int_{-1}^{1}\sigma_s(x,\mu'\rightarrow\mu)\psi(x,\mu')d\mu'+s(x,\mu) \qquad \textbf{(3)}$$

Where ψ is the angular particle density, x is the spatial position; and μ is the cosine of the angle with a range of $-1\le\mu\le1$; and μ' is the cosine of the angle from which the photon is scattered. The description and nomenclature of these methods largely follows that presented by Lewis and Miller[33] and the reader is referred to their text for more detailed information.

Treatment of Scatter

Prior to discussing the discretization of equation (3)(3) we need to develop a method to treat the scattering term in a manner suitable for efficient computation. By convention, the scattering cross section, $\sigma_s(x,\mu' \to \mu)$, is typically expanded using Legendre polynomials and can be expressed as:

$$\sigma_s(x,\mu_o) = \sum_{l=0}^{L}(2l+1)P_l(\mu_o)\sigma_l(x) \tag{4}$$

where $\mu_o = \mu' \to \mu = \hat{\Omega}' \cdot \hat{\Omega} = \cos\theta$, L is the scattering degree, P_l is the Legendre polynomial,

$$P_l(\mu) = \frac{1}{2^l l!}\frac{d^l}{d\mu^l}\left(\mu^{2-1}\right)^l \tag{5}$$

and $\sigma_l(x)$ is the scattering moment and is calculated using the Legendre expansion's orthogonality properties:

$$\sigma_l(x) = \frac{1}{2}\int_{-1}^{1}\sigma_s(x,\mu_o)P_l(\mu_o)d\mu_o \tag{6}$$

The order of the Legendre polynomial represents the order of scattering. For example, when the Legendre polynomial is zeroeth order (P_0), equation (4) models isotropic scatter while first order and higher polynomials model increasingly anisotropic, or forward peaked scatter.

Recognizing that $\int_{-1}^{1}\psi(x,\mu)d\mu = \phi(x)$ and expanding $\phi(x)$ with Legendre polynomials, we obtain the Legendre moments

$$\phi_l(x) = \frac{1}{2}\int_{-1}^{1} P_l(\mu)\psi(x,\mu)d\mu \,. \tag{7}$$

Substituting equations (4) and (7) into equation (3) yields the 1-D form that will be discretized:

$$\mu\frac{\partial}{\partial x}\psi(x,\mu) + \sigma_t(x)\psi(x,\mu) = \sum_{l=0}^{L}(2l+1)P_l(\mu_o)\sigma_l(x)\phi_l(x) + s(x,\mu) \tag{8}$$

Discrete Ordinates Approximation

In the discrete ordinates approximation, we pick a finite number of angles (N) with direction cosine μ_n and solve the RTE only at those angles. Any particles scattering outside of these angles are forced into the nearest neighboring angles and equation (8) becomes a set of N equations:

$$\mu_n\frac{\partial}{\partial x}\psi_n(x) + \sigma_t(x)\psi_n(x) = \sum_{l=0}^{L}(2l+1)\sigma_l(x)P_l(\mu_n)\phi_l(x) + s(x,\mu_n), \quad n = 1,2,...,N \tag{9}$$

where $\psi_n(x) = \psi(x,\mu_n)$, and the number and distribution of the angles are governed by the angular quadrature chosen for the problem.

Angular Quadrature

The angular quadrature is the set of angles over which the RTE will be solved via the discrete ordinates method. While any quadrature set can be developed and used, care should be taken to choose a quadrature which is capable of accurately modeling the physics of the problem. Generally a 1-D quadrature of order N has *N* ordinates μ_n on the interval of $-1 \le \mu \le 1$ with corresponding weights w_n. The weights

are positive, and on the interval -1 ≤ μ ≤ 1 sum to 2. The scalar flux is approximated by the weight normalized quadrature formula

$$\phi(x) = \frac{1}{2}\sum_{n=0}^{N} w_n \psi_n(x), \tag{10}$$

and the Legendre moments are approximated by

$$\phi_l(x) = \frac{1}{2}\sum_{n=0}^{N} w_n P_l(x) \psi_n(x). \tag{11}$$

To account for the equal importance of particles flowing in the positive and negative x direction, an even number of ordinates symmetric about μ=0 is typically used. This is due to the fact that when an odd number of ordinates are used, the ordinate $\mu_{(N+1)/2} = 0$ lies perpendicular to the x axis and its derivative disappears from the discrete ordinates equations introducing discontinuities and further ambiguity when boundary conditions are set. To avoid this problem, the ordinates are generally required to satisfy the following requirements

$$\begin{aligned} &\mu_n > 0, \\ &\mu_{N+1-n} = -\mu_n, \ n = 1,2,...,\frac{N}{2} \\ &w_{n+1-n} = w_n. \end{aligned} \tag{12}$$

In 1-D problems, the Legendre and double Legendre are the most commonly used quadrature formulas. In the Legendre formula, the angular fluence is approximated by

$$\psi(x,\mu) \approx \sum_{l=0}^{L} (2l+1)\phi_l(x) P_l(\mu), \tag{13}$$

where ϕ_l is the same unknown as the Legendre moments given in the scattering term of equation (9). The quadrature ordinates are the roots to the polynomial

$$P_N(\mu_n) = 0, \qquad n = 1,2,...,N \tag{14}$$

and the weights are the solution to the series of equations provided by

$$\frac{1}{2}\sum_{n=1}^{N} w_n P_l(\mu_n) = \delta_{l0}, \qquad l = 0,1,...,N-1 \tag{15}$$

where δ_{ij} is the Kronecker delta and is defined as

$$\delta_{ij} = \begin{cases} 1, & i = j \\ 0, & i \neq j. \end{cases} \tag{16}$$

In the double Legendre quadrature formula the expansion of the angular fluence is split over the interval $-1 \leq \mu < 0$ and $0 < \mu \leq 1$ as

$$\psi(x,\mu) \approx \begin{cases} \sum_{l=0}^{N} (2l+1)\phi_l^{+}(x) P_l(2\mu - 1), & \mu > 0 \\ \sum_{l=0}^{N} (2l+1)\phi_l^{-}(x) P_l(2\mu + 1), & \mu < 0. \end{cases} \tag{17}$$

The unknown flux is expressed as

$$\phi_l^{\pm}(x) = \pm \int_0^{+1} d\mu (2\mu \mp 1)\psi(x,\mu) \tag{18}$$

and the ordinates are determined from the solutions of

$$\begin{aligned} P_{(N-2)/2}(2\mu_n + 1) &= 0, \qquad n = 1,2,...,\frac{N}{2} \\ P_{(N-2)/2}(2\mu_n - 1) &= 0, \qquad n = \frac{N}{2}+1, \frac{N}{2}+2,...,N \end{aligned} \tag{19}$$

while the weights are determined by

$$\sum_{n=1}^{N/2} w_n P_l(2\mu_n + 1) = \delta_{l0}, \qquad l = 0,..., \frac{N-2}{2}$$
$$\sum_{n=N/2+1}^{N} w_n P_l(2\mu_n - 1) = \delta_{l0}, \qquad l = 0,..., \frac{N-2}{2}. \tag{20}$$

Boundary Conditions

The boundary conditions most often used in RTE solvers are the reflective and vacuum boundaries. When even numbers of ordinates are used, the reflective boundary condition can be expressed as

$$\psi_n(0) = \psi_{N+1-n}(0), \qquad n = 1,2,..., \frac{N}{2} \tag{21}$$

and the vacuum boundary at $x=a$ can be expressed as

$$\psi_n(a) = 0, \qquad n = \frac{N}{2}+1, \frac{N}{2}+2,..., N\ . \tag{22}$$

Source Iteration

After angular discretization, the equations must be spatially discretized. To discretize the 1-D equation, we introduce an iteration index, m, to equation (9) to obtain

$$\mu_n \frac{\partial}{\partial x}\psi_n^{m+1}(x) + \sigma_t(x)\psi_n^{m+1}(x) = q_n^m(x) \tag{23}$$

and

$$q_n^m(x) = \sum_{l=0}^{L}(2l+1)\sigma_l(x)P_l(\mu_n)\phi_l^m(x) + s(x,\mu_n) \tag{24}$$

which are written in a form such that the iteration can take place on the scattering source q_n^m. This approach, commonly called source iteration is almost exclusively used for the solution of the discrete ordinates because of its ability to efficiently solve for ψ when the scattering source (equation (24)) is known. If we take the initial fluence (in terms of iterations, i.e. *m*=0) to be

$$\psi^0 = 0, \tag{25}$$

we see that ϕ_l^0 (equation (11)) is also zero and thus the only remaining portion of the scattering source (equation (24)) is the uncollided fluence due to the source term *s*. We express the (*m*+1)th iterate as the sum

$$\psi^{m+1} = \sum_{m=0}^{M} \psi^m , \tag{26}$$

substitute into equations (23) and (24), and combine them to obtain

$$\sum_{m=0}^{M} \left[\mu_n \frac{\partial}{\partial x} + \sigma_t^m(x) \right] \psi_n^m(x) = \sum_{m=0}^{M-1} \sum_{l=0}^{L} (2l+1) \sigma_l^m(x) P_l(\mu_n) \phi_l^m(x) + s(x, \mu_n). \tag{27}$$

Thus, the first iteration (*m*=1) represents the solution for the first set of collisions, while, the second iteration (*m*=2) represents the solution for the second set of collisions and so on. From this physical representation, we can gain an understanding of how quickly the source iteration converges. When absorption dominates source iteration converges quickly, however, when scatter dominates convergence can

become prohibitively slow. Acceleration techniques have been developed to improve the convergence rate, and will be discussed later.

Spatial Discretization

Spatial discretization involves the division of the spatial variable into a grid with I mesh nodes as shown in Figure 10 for the 1-D case. The cross sections are constant across each element and the value of center node in each element is

$$x_i = \frac{1}{2}\left(x_{i+1/2} + x_{i-1/2}\right). \tag{28}$$

To simplify the notation in the following equations, we will drop the scattering iteration notation (m). Integrating equations (23) and (24) from $x_{i-1/2}$ to $x_{i+1/2}$ we get

$$\mu_n\left[\psi_{i+1/2,n} - \psi_{i=1/2,n}\right] + \sigma_{t,i}\Delta_i\psi_{in} = \Delta_i q_{in} \tag{29}$$

and

$$q_{in} = \sum_{l=0}^{L}(2l+1)\sigma_{li}(x)P_l(\mu_n)\phi_{li} + s_{in} \tag{30}$$

where $\Delta_i \equiv x_{i+1/2} - x_{i-1/2}$, $\psi_{in} = \psi_n(x_i)$, $\sigma_{li} = \sigma_l(x_i)$, $\phi_{li} = \phi_l(x_i)$, and $s_{in} = s(x_i, \mu_n)$.

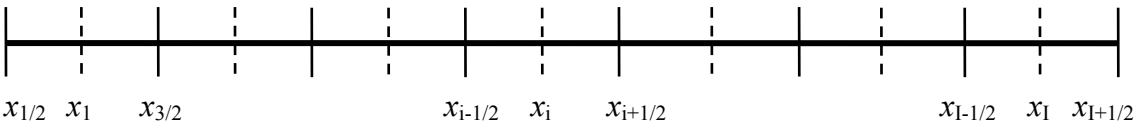

Figure 10: Spatial discretization of a 1-D domain.

To solve the spatially discretized equations, we need an auxiliary equation to relate the $\psi_{i\pm1/2,n}$ and ψ_{in}. There are a variety of auxiliary equations available, with one of the most common ones being the diamond difference relation:

$$\psi_{in} = \frac{1}{2}\left(\psi_{i+1/2,n} + \psi_{i-1/2,n}\right). \tag{31}$$

The fluence can then be found by substituting this equation into equation (29) and constructing an appropriate algorithm to solve the equations. This typically includes separating the positive and negative μ_n directions, and performing sweeps from one side of the spatial domain to the other in the same direction as the particle movement.

Two of the major advantages of this method include its low memory requirements due to the sweeping nature of the algorithm and the second order accuracy (in terms of spatial truncation) of its solutions. However, it has a major drawback in that when there is exponential attenuation in the cross sections, the diamond differencing scheme introduces negative fluxes. To avoid this effect, the mesh element sizes must be smaller than the free mean path of the particle,[34, 35] significantly increasing calculation times. Alternatively, the negative-flux-fixup, in which negative fluxes are set to zero, can be used, but this approach degrades the accuracy of the solution and also increases computation time.

Other differencing schemes have been developed which guarantee positive flux values. The step method is perhaps the simplest alternative. In this method, equation (31) is replaced by

$$\begin{aligned} \psi_{i+1/2,n} &= \psi_{in}, \quad \mu_n > 0 \\ \psi_{i-1/2,n} &= \psi_{in}, \quad \mu_n < 0 \end{aligned} . \tag{32}$$

While this scheme always provides positive fluxes, it is less accurate than the diamond differencing scheme at larger element sizes and regardless of step size is only first order accurate.

The linear discontinuous method is another attractive alternative to the diamond differencing scheme. In this method the flux is assumed to be a linear function which is discontinuous at the edges of the elements as illustrated in Figure 11.

The auxiliary equation in this case is given as

$$\psi_{in}(x) = \frac{1}{\Delta}\left\{\psi^{R}_{i+1/2,n}\left(x_{i+1/2} - x\right) + \psi^{L}_{i+1/2,n}\left(x - x_{i-1/2,n}\right)\right\}. \tag{33}$$

While somewhat more complicated than diamond differencing, this method is more accurate and less prone to producing negative fluxes.

Acceleration

Source iteration has often been employed as a method of choice to iteratively solve the discrete ordinate equations.[36-38] While powerful in void-like or highly absorptive regions, convergence of the source iteration method is prohibitively slow in

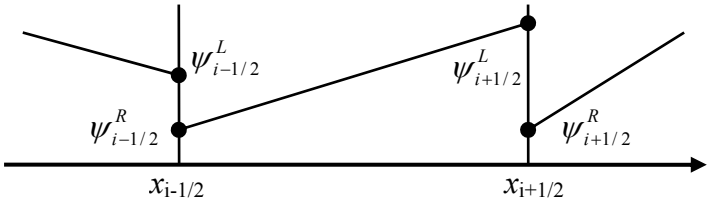

Figure 11: Linear discontinuous differencing method.

regimes in which scatter dominates (such as biological tissues).[39] Acceleration techniques have been developed to increase the convergence rate of source iteration. Synthetic diffuse acceleration is a class of accelerators that uses the lower order diffusion approximation to accelerate the convergence rate of the numerical transport solution. For simplicity in illustrating this principle, we assume isotropic scatter and isotropic source. Rewriting the RTE in operator notation for the *m*-th iteration we get

$$H\psi_m^* = S + \sigma_s \phi_{m-1} \tag{34}$$

where

$$H\psi = \left[\hat{\Omega} \cdot \vec{\nabla} + \sigma_t\right]\psi \,. \tag{35}$$

The transport corrected diffusion equation can also be written in operator notation for the *m*-th iteration to obtain

$$H_D \phi_m = S' - R_m \,. \tag{36}$$

where

$$H_D = -\vec{\nabla} \cdot D\vec{\nabla} + \sigma_r \tag{37}$$

and *R* is the correction term

$$R_m^* = \vec{\nabla} \cdot J_m^* + \vec{\nabla} \cdot D\vec{\nabla}\phi_m^* , \tag{38}$$

with

$$\phi_m^* = \int \psi_m^* d\mu \tag{39}$$

and

$$J_m^* = \int \mu \psi_m^* d\mu \,. \tag{40}$$

As in the notation of Hielscher *et al.*,[40] the asterisk indicates those quantities which are determined using the angular flux (ψ) obtained from the transport equation, while the scalar flux (ϕ) is determined from the diffusion equation. The acceleration process then takes place by solving equation (34) for ψ_m^* using the known scalar flux (ϕ_{m-1}) from the previous iteration or, if acceleration is wanted in the first iteration (m=0), the correction term (R) can be set to zero and equation (36) can be solved for ϕ_0. After obtaining ψ_m^*, the diffusion equation (equation (36)) can be used to obtain ϕ_m and the process is repeated until convergence is achieved. It has been shown that the numerical solution acquired using DSA is the same as that obtained using asymptotic expansion techniques which describes how analytic transport theory transitions to analytic diffusion theory.[34]

While this technique can significantly accelerate the convergence of the discrete ordinates method, its accuracy is dependent on the consistency between the discretized diffusion and RTE equations.[41] Because of this, DSA can be difficult to implement in multi-dimensions and for some spatial discretization schemes.

Until recently, computers capable of numerically solving the full RTE deterministically were not readily available, and robust but time consuming stochastic

techniques such as Monte Carlo or an approximation, such as the diffusion approximation which could be solved numerically, provided the most efficient means of estimating its solution.

Monte Carlo

The Monte Carlo approach uses statistical or stochastic methods to simulate the physical processes described by the radiative transport equation. In this approach the physical processes of scattering and absorption, which govern light transport, are described in terms of probability density functions. Simulations are carried out by sampling the probability density functions using random numbers and an approximate solution to the RTE is obtained when a statistically significant number of random samples are taken. While each code implementing Monte Carlo for photon propagation has its own unique characteristics, most, if not all, follow the same basic algorithm as shown in Figure 12. The following description describes the basic algorithm as employed by Jacques and Wang[42] in their Monte Carlo code for time-invariant, multi-layered systems. Briefly, a packet of 'photons' with a weight of one is launched into the system. The distance or step size, *S*, that the packet will travel is determined by $S = s\mu_t = -\ln(\zeta)\mu_t$ where ζ is a random number and μ_t is the total extinction coefficient and is the sum of the absorption and scattering coefficients. Prior to moving the packet, the code verifies whether the packet will encounter a boundary (internal or external) during its movement. If a boundary is to be crossed, the photons are moved to the boundary and their transmission or reflection is determined by Snell's law. If the packet does not encounter a boundary then the

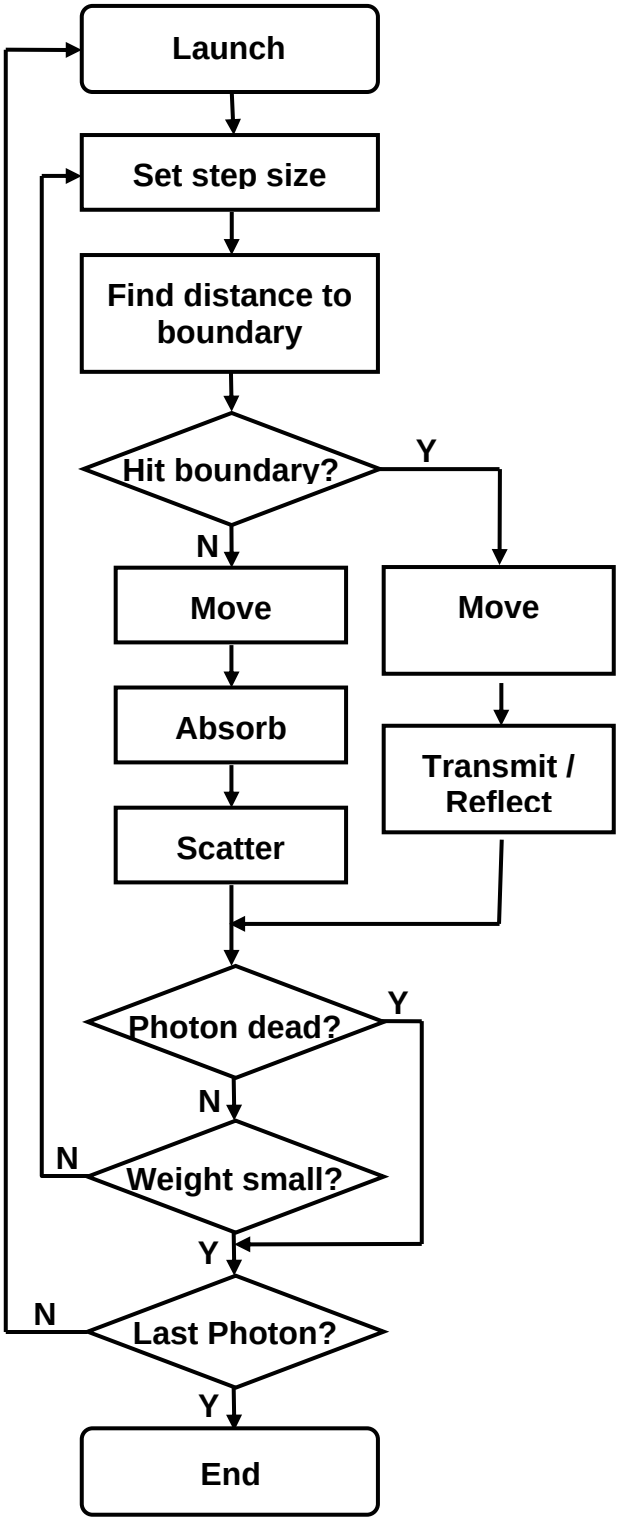

Figure 12: Illustration of a typical Monte Carlo algorithm (adapted from Wang *et al.*[43]).

photons are moved, and a portion of the weight is 'absorbed' (stored in the grid) as determined by the ratio μ_a/μ_t. The scattered direction in which the remaining portion of the packet will travel is determined by calculating a deflection angle and an azimuthal angle, φ. The deflection angle, θ, with a range of $0 \le \theta < \pi$ is determined using the following probability density function based on the Henyey-Greenstein function.

$$\cos\theta = \begin{cases} \frac{1}{2g}\left[1+g^2-\left(\frac{1-g^2}{1-g\_2g\xi}\right)^2\right] & if\ g \neq 0 \\ 2\xi - 1 & if\ g = 0 \end{cases} \quad \textbf{(41)}$$

where g is the anisotropy factor and equals $\langle\cos\theta\rangle$, and ξ is a random number. The azimuthal angle is distributed uniformly between 0 and 2π and is sampled by $\varphi = 2\pi\xi$. After the boundary interaction or scattering angle is calculated, the weight of the packet is tested to determine if sufficient photons remain to warrant continued propagation. If sufficient weight remains, a new step size is calculated and the procedure repeats itself. If the remaining weight is too small to it is stored to the grid and another photon packet is launched. This process continues until the solution is stable, and the addition of photon packets does not change the relative measurements.

Monte Carlo provides a powerful tool to model the physical processes which govern particle transport across simple or complex spatial geometries and is considered the 'gold standard' by many. However, due to the random nature of Monte Carlo, large numbers of photons are needed to obtain statistically significant results. The number of photons and subsequently the amount of time and computer resources

needed increase as the complexity of the system increases often leading to computation times of hours or even days.

Diffusion Approximation

In the biomedical optics community, much of the current research is done on optically thick tissues where photons multiply scatter prior to detection. In these situations, the radiative transport equation itself is generally too cumbersome and expensive for direct application; instead, the diffusion approximation is used (see Duderstadt & Hamilton[32] for the general derivation). In this approximation, it is assumed that all the photons are of the same energy and that they multiply scatter in the medium prior to absorption or detection. The diffusion equation is shown in equation (42).

$$-\nabla\cdot\left[D_x(\vec{r})\nabla\Phi_x(\vec{r},\omega)\right]+\left[\left(\mu_{a_{xi}}+\mu_{a_{xf}}\right)(\vec{r})+\frac{i\omega}{c_x}\right]\Phi_x(\vec{r},\omega)=S\delta(\vec{r}-\vec{r}_s) \tag{42}$$

where Φ_i is the angle integrated photon flux and D_i is the optical diffusion coefficient and is given by:

$$D_i=\frac{1}{3\left(\mu_{a_i}+\mu_{s_i}(1-g)\right)} \tag{43}$$

In our labs, the diffusion equation is generally solved using a partial current boundary condition described by,

$$\Phi_{x,m}(\vec{r},\omega)+2\gamma D_{x,m}(\vec{r})\frac{\partial\Phi_{x,m}(\vec{r},\omega)}{\partial n}=0 \tag{44}$$

where γ is the index-mismatch parameter which describes the portion of the light at the boundary which is reflected back into the system.[44, 45] S is the excitation light source term and for computational ease, is generally modeled as an isotropic point source. The limits of the diffusion approximation require that the isotropic scattering coefficient ($\mu_s' = \mu_s(1-g)$) be much greater than the absorption coefficient such that $\mu_s' \geq 10\mu_a$, and that the detector be far away from the source (>10 mean free paths). These limits generally hold true for large tissue volumes such as human breast tissue. Small animals such as mice have a wide range of optical properties in a small volume including diffusive regions such as the skin ($\mu_s' = 62cm^{-1}$, $\mu_a = 2.8cm^{-1}$) and highly absorptive regions such as the liver ($\mu_s' = 5.8cm^{-1}$, $\mu_a = 5.7cm^{-1}$) where the diffusion equation is not valid.[46] Because of the wide range of optical properties and the small volumes of interest, *the diffusion approximation is not strictly valid in mice*.

Tomographic Reconstruction Algorithms

In Merriam-Webster's Medical Dictionary, tomography is defined as "a method of producing a three-dimensional image of the internal structures of a solid object (as the human body) by the observation and recording of the differences in the effects on the passage of waves of energy impinging on those structures."[47] The type of algorithm used in tomography depends greatly on the manner by which the energy propagates through the solid object. One of the easiest and most straightforward empirically based algorithms is the filtered backprojection technique commonly employed in x-ray CT.

Backprojection

Backprojection is based on the fact that x-rays pass through soft tissues in a straight line with relatively little scattering. To obtain the data needed to reconstruct the internal structure, a set of x-ray beams is sent through the object and detected on the opposite side. The x-ray source and detector are rotated around the object to collect data at multiple angles around the object. The attenuated x-ray data, commonly called projection data, is then used to construct an attenuation map of the internal structure of the object being imaged. Backprojection is a well known technique and is described in detail in the literature.[48, 49] The majority of backprojection algorithms are based on the Radon function, $P(\theta,t)$, shown in equation (45) for a parallel beam geometry:

$$P(\theta,t)=\int_{-\infty}^{\infty}\int_{-\infty}^{\infty} f(x,y)\delta(x\cos\theta+y\sin\theta-t)dxdy\,. \tag{45}$$

In this equation, $f(x,y)$ describes the attenuation properties of the object (the unknown) and $\delta(x\cos\theta+y\sin\theta-t)$ is a delta function which limits the integration to points which lie on the line (the path of the x-ray) described by $x\cos\theta+y\sin\theta=t$.

To acquire a backprojected image, the inverse Fourier transform of the projection function is taken to obtain:

$$f(x,y)=\frac{1}{4\pi^2}\int\int P^*(\theta,t)\exp^{(i(\theta x+ty))}\,dxdy \tag{46}$$

where: $P^*(\theta,t)$ is the set of all projection functions. This algorithm can be implemented by simply dividing up the object into a finite number of pixels (2-D) or

voxels (3-D) and then "smearing" or adding the detected value of each beam to each pixel or voxel that it traversed while passing through the object. The summation of the projections results in an attenuation map of the interior of the object. To enhance the accuracy of this algorithm, a weight or filter function is often included in equation (46) to assign portions of the detected value to each pixel. The major advantage to this algorithm is that it is very fast to implement and can be used to generate clinical images in real time. Some efforts have been made to implement backprojection to optical tomography.[50-53] In optical tomography however, the light no longer propagates in straight lines, which convolutes the backprojected image.

Iterative approaches

When diffraction, refraction, or scattering events significantly alter the path of a photon through the object, iterative algorithms are generally needed to tomographically reconstruct the internal structure. These algorithms consist of two problems, the forward problem and the inverse problem and have been called model based-iterative image reconstruction (MOBIIR) algorithms.[12] In the forward problem, a spatial distribution of optical properties is assumed, and the resulting measurements at the surface of the object are predicted. These measurements are then passed to the inverse problem where they are used to determine a new spatial distribution of the optical properties. The updated distribution is then passed back to the forward problem, and the process is iteratively repeated until the predicted measurements match the experimental values. The resulting spatial distribution represents the tomographic structure of the object.

Because the number of known measurements is typically less than the number of unknowns, the inverse problem is ill-posed or underdetermined with noise sensitive, non-unique solutions. The various approaches developed to solve the inverse problem can generally be broken down into two basic formulations, integral and differential. The following sections offer a brief introduction to these formulations, for a more detailed treatment see Hawrysz *et al*.[13] and Arridge.[54]

Integral Inversions

In the integral inversion formulation, we assume that the optical properties in the object are uniform (estimated with *a priori* knowledge of the object) and that a small perturbation in the optical properties causes a change in the detected signal at the surface boundary. The measured signal for each source and detector pair can then be expressed as an equation summing the small, weighted perturbations throughout the object. The weighting factors are calculated using a forward model assuming that, with the exception of the small perturbations, the optical properties are uniform throughout the object, an approach commonly known as the Born approximation.[13] The main advantage to this approach is that the excitation and emission profiles are decoupled, and the inverse problem is reduced to a set of linear equations which can be solved to obtain the optical property map of the object.

The set of equations can be expressed in matrix form as $\Phi = J\mu$. Where the matrix Φ (n x 1) represents the detected fluxes for the source/detector pairs (n), J (n x m) represents the weight factors (m is number of unknowns in the system), and μ (m x 1) is the optical property map which is being reconstructed. Pseudo inversion seeks to

invert the rectangular matrix J by multiplying J by its transpose to obtain an invertible square matrix of dimension (n x n). Singular value decomposition seeks to convert matrix J to an identity matrix which can then be easily solved for μ. Some of the drawbacks to these techniques are the instabilities produced in the solution by measurement noise and by errors generated in the forward problem. Regularization techniques, in which additional parameters are introduced, help stabilize the solution to the inversion problem.[13] Another linear technique used to solve the set of linear equations is the algebraic reconstruction technique (ART) as discussed below.

Algebraic Reconstruction Techniques

Algebraic reconstruction techniques do not require direct matrix manipulation; instead the measurement data is treated as a type of projection similar to the projections acquired in x-ray CT. As with CT, the projections are distributed back through an image from detector to source; however, due to the variation of the path from the source to the detector, iterative methods are needed obtain a correct distribution of the projection throughout the object. A description of the basic technique utilized in ART is discussed in Kak and Slaney,[49] and is briefly presented here in a two dimensional case.

Suppose the object of interest, $f(x, y)$ is superimposed with a square grid (see Figure 13) and that the value of pixel f_i is constant within the i_{th} pixel. Each projection (p_i) or measurement is represented as a "ray sum," a line with a finite thickness as illustrated in Figure 13. In this simplistic case, the contribution (denoted by the weight factor w_{ij}) of the j^{th} pixel to the i^{th} ray sum are geometrically calculated based

on the ratio of the area of the pixel covered by the line, and the total area of the pixel. The relationship between the projection and the pixels is described by:

$$\sum_{j=1}^{N} w_{ij} f_j = p_i, \qquad i = 1, 2, ..., M \tag{47}$$

where M is the total number of rays, and N is the total number of pixels.

A grid with N pixels has N degrees of freedom. Therefore an object represented by $(f_1,f_2,\ldots,f_N)$ may be considered to be a single point in an N-dimensional space. In this space, each of the expanded equations from equation (47) represents a hyperplane. When a unique solution to those equations exists, the intersection of all these planes is a single point giving that solution. The solution is found by iteratively seeking this point. This is best illustrated by considering the case of only two variables f_1 and f_2 satisfying the following equations:

$$\begin{aligned} w_{11} f_1 + w_{12} f_2 &= p_1 \\ w_{21} f_1 + w_{22} f_2 &= p_2 . \end{aligned} \tag{48}$$

Make an initial guess for all f_j denoted as $f_j^{(0)}$ where $\vec{f}^{(i)} = \left[f_1^{(i)}, f_2^{(i)}, ..., f_N^{(i)} \right]$ vectorially represents all the N values of f_j for the i^{th} iteration:

$$\vec{f}^{(i)} = \vec{f}^{(i-1)} - \frac{\left(\vec{f}^{(i-1)} \cdot \vec{w}_i - p_i \right)}{\vec{w}_i \cdot \vec{w}_i} \vec{w}_i \tag{49}$$

where $\vec{w}_i = \left(w_{i1}, w_{i2}, ..., \vec{w}_{iN} \right)$ and $\vec{w}_i \cdot \vec{w}_i$ is the dot product of $\vec{w}_i$ with itself. Figure 14 shows the schematic representing the iterative process for equation (49). An initial guess shown as $\vec{f}^{(0)}$ is made and then projected back onto the hyperplane represented by the first equation to obtain $\vec{f}^{(1)}$ which in turn is projected back onto the hyperplane

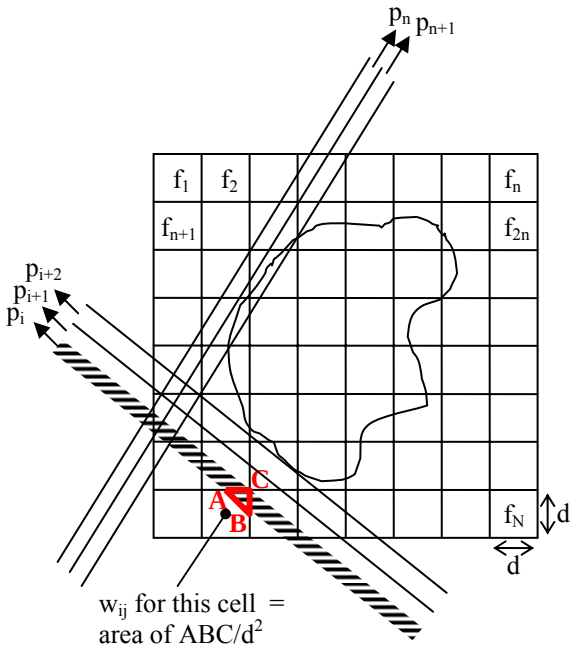

Figure 13: Illustration of a basic algebraic reconstruction approach (Adapted from Kak and Slaney[49])

represented by the second equation to obtain $\vec{f}^{(2)}$. The iterations project on the hyperplanes until they converge to the point at which they intersect. More complex variations of ART include those that use a forward model such as the diffusion approximation or the radiative transport equation to calculate the weight factors as opposed to the geometric ratio discussed above.

Differential formulations

Differential formulation is another common class of inversion algorithms. In this formulation, the error between the measured values and the predicted values is minimized. This is done by adjusting the optical properties iteratively until the

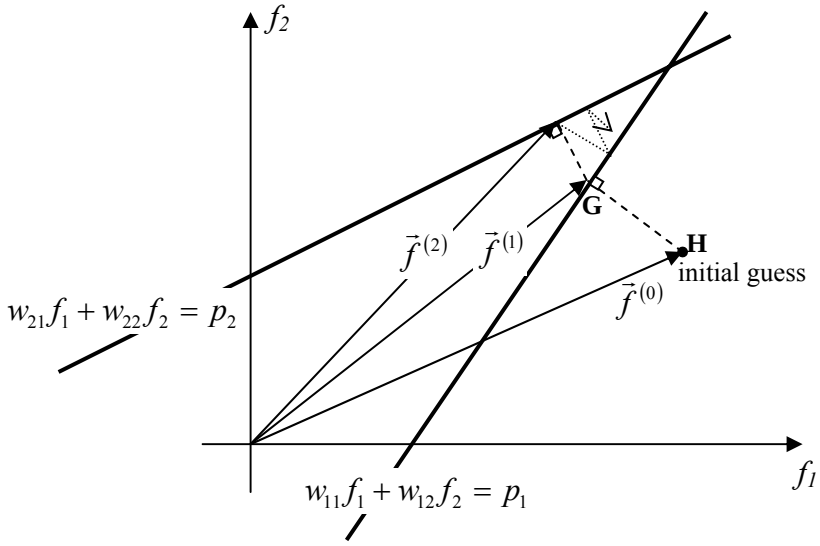

Figure 14: Illustration of the iterative nature of ART for a system with 2 degrees of freedom.

predicted measurements match the true measurements. The iterations are governed by a Jacobian matrix, which specifies how the predicted measurements change as the optical properties within the object change. As such the slope of the Jacobian is used to update the optical properties map. Iterations continue until the error between the predicted values and the measured values is minimized.[13] These types of iterative tomographic algorithms require optimization techniques and are typically computationally expensive. Their viability and accuracy in tomographic reconstruction largely depends on the physical model used to predict the propagation of light through the tissue. In optical tomography, the forward problems most commonly used are the radiative transport equation and the diffusion approximation.

Literature Review

A variety of approaches to the optical tomography problem have been taken in the literature. These range from simple backprojection with CW light sources to complex inverse algorithms implementing the RTE as the forward and inverse model. Table 1 presents a summary of the work specifically related to small volumes and/or small animals. While many different approaches have be taken, none have undertaken the development of a radiative transport based fluorescence enhanced small animal optical tomography system as presented in this dissertation.

Table 1: Summary of the literature on small volume/animal research (reproduced with permission from Rasmussen *et al*. [55])

Reference	Imaging System	Contrast[+]	Forward Model	Reconstruction Algorithm	Model/ Phantom	Simulated/ Measured	Optical Properties[*]	Comments
Hielscher *et al.* 1998[40]	CW	Endo.	Diffusion and RTE using DANTSYS with diamond-differencing and DSA	--	a) 2D and 3D simulations b) 2D MRI brain slice (simulated)	Simulated	a) μ_s' = 5 μ_a = 0.05-2.5 g = 0 b) μ_s' = 0.1-18.0 μ_a= 0.01-3.0 g = 0	Demonstrated need for RTE by comparing to diffusion over broad range of optical properties, including a 2D MRI slice of a human brain.
Klose *et al.* 1999,[56] 2002,[57] 2002,[58]	CW	Endo.	RTE with discrete ordinates and upwind-step differencing	MOBIIR adjoint differentiation with gradient based optimization	a) 3x3x14 cm SiO_2 in resin b) 4x4x14 cm SiO_2 in resin with void c) 3x3x14 cm SiO_2 in resin with 3 cylindrical voids	Measured	a) μ_s = 58 μ_a = 0.35 g = 0.8 b) μ_s = 58 μ_a = 0.35 g = 0.8 c) μ_s = 50 μ_a = 0.62 g = 0.85	Developed a 2D RTE algorithm; compared results to 3D exper-imental data; performed 2D reconstruction.

Table 1 continued

Reference	Imaging System	Contrast[+]	Forward Model	Reconstruction Algorithm	Model/ Phantom	Simulated/ Measured	Optical Properties[*]	Comments
Ntziachristos *et al.* 2001[59]	CW	Fluor.	Diffusion using Born type approx-imation	ART	2.5x10 cm cylinder with 2 fluorescent targets	Measured	μ_s' = 7cm μ_a = 0.05 target = 0.5-0.75μM Cy5.5	Demonstrated the 2D reconstruct-tion of two fluorescent targets in phantom with homogeneous endogenous background.
Abdoulaev *et al.* 2003[60]	CW	Endo.	Reduced RTE to 2nd order PDE's using an even parity approach and solved with finite element methods	MOBIIR adjoint differentiation with gradient based optimization	a) 3x3x3 cm simulation with 2 absorbing targets b) simulated human fore-head with 1 absorbing target	Simulated	a_1) μ_s = 5 μ_a = 0.1 μ_{a_target} = 0.5 a_2) μ_s = 1 μ_a = 0.1 $\mu_{s_}$target = 3 b) μ_s = 5 μ_a = 1 $\mu_{a_}$target = 2	Developed a 3D RTE algorithm by using an even-parity approach, thereby reducing the RTE to a system of PDE's.
Culver *et al.* 2003[61]	FD	Endo.	Diffusion	Diffusion with Tikhonov regularization and Moore-Penrose inverse of a Rytov formulation	Rat cranium	Measured	Not specified, refers reader to the literature	Demonstrated reconstruction of hemodynamic activity in rat brain.

Table 1 continued

Reference	Imaging System	Contrast[+]	Forward Model	Reconstruction Algorithm	Model/ Phantom	Simulated/ Measured	Optical Properties[*]	Comments
Das *et al.* 2003,[62] 2003[63]	TD	Endo.	RTE using a piecewise parabolic advection scheme	--	2.5x10x0.8 cm TiO_2	Measured	μ_s = 2-20 μ_a = 0.01-0.9 μ_{s_targ} = 30-40 μ_{a_targ} =0.01-0.5	Compared the transient RTE solution to experimental short-pulse laser propagation data.
Klose *et al.* 2003[37]	CW	Fluor.	RTE with discrete ordinates, source iteration, and step differencing	RTE based on a limited memory Broyden-Fletcher-Goldfarb-Shanno technique with adjoint differentiation	3x3 cm simulation	Simulated	μ_s = 10 μ_a =0.1 μ_{axf} = 0.01-0.3 QE=0.02-0.1	Demonstrated the 2D solution of the fluorescence radiative transport equation and 2D reconstruction based on fluorescence yield and fluorescence absorption in homogeneous endogenous background.
Ripoll *et al.* 2003[64]	CW	Endo.	Diffusion with Green's theorem and a diffuse-reflection boundary method.	ART	Simulation of complex semi-elliptical 2D shape ~2.5x1.5cm	Simulated	μ_s' = 10 μ_a = 0.02-0.2 μ_{atarg} = 0.2-0.4	Demonstrated use of a diffuse-reflection boundary method to efficiently model complex diffuse/nondiffuse boundaries.

Table 1 continued

Reference	Imaging System	Contrast[+]	Forward Model	Reconstruction Algorithm	Model/ Phantom	Simulated/ Measured	Optical Properties[*]	Comments
Schultz *et al.* 2003,[65] 2004[66]	CW	Fluor.	Diffusion with Green's theorem, Kirchoff's approximation, and a free space propagation model.	ART	a) Semi-cylindrical phantom simulation b) Mouse	a) Simulated b) Measured	a) $\mu_s' = 10$ $\mu_a = 0.3$ 0.5-1.0uM Cy5.5 targets b) 2 mm diameter tube with 2μM Cy5.5 in esophagus	Demonstrated use of surface rendering techniques to facilitate noncontact instrumentation and reconstruction requirements; assumed homogeneous endogenous background.
Bluestone *et al.* 2004,[22] 2004[23]	CW	Endo.	Diffusion	MOBIIR adjoint differentiation with gradient based optimization	Rat cranium	Measured	D = 0.45-1.46 μ_a = 0.05-0.22	Used a priori structural information and experimental data to reconstruct hemodynamic changes in rat brain.
Kim *et al.* 2004,[67] Kim 2004[68]	CW	Endo.	RTE with Green's function and plane wave mode expansion Fokker-Planck Leakeas-Larsen	--	2D 10x10 cm simulation	Simulated	g = 0.0-0.95 all other properties dimensionless	Solved the RTE using Green's function for isotropic scatter; replaced RTE with the Fokker-Planck or Leakeas-Larsen equation for forward peaked scatter.

Table 1 continued

Reference	Imaging System	Contrast[+]	Forward Model	Reconstruction Algorithm	Model/ Phantom	Simulated/ Measured	Optical Properties[*]	Comments
Quan *et al.* 2004[69]	TD	Fluor.	Coupled RTE with discrete ordinates, unspecified differencing scheme	Form of ART using fluorescence flight time	Simulated a 2 cm cube with 4 mm cubic target with uptake ratio from 15:1 to 100:1	Simulated	μ_{sx} = 10.18 μ_{ax} = 0.023 μ_{sm}=8.64 μ_{am} = 0.031	Demonstrated reconstruction based on fluorescent time of flight from simulated time domain data.
Ren *et al.* 2004[38]	FD	Endo.	RTE with discrete ordinates, source iteration, and upwind-step differencing	--	a) 2D 5x5 cm simulations b) simulated 2 cm diameter cylinder with void target	Simulated	a) μ_s = 50-100 μ_a = 0.5-1 g = 0.9 ω = 200 b) μ_s = 120 μ_a = 0.1 g = 0.9 ω = 200-600	Developed an RTE algorithm in the frequency domain.
Abdoulaev *et al.* 2005[70]	FD	Endo.	RTE with discrete ordinates and upwind-step differencing	1st order PDE constrained optimization via an augmented Lagrangian method	2 x 2 cm cylinder simulation	Simulated	μ_s = 10 μ_a = 0.1-0.5 g=0-0.9 μ_{s_targ} = 10-15 μ_{a_targ} = 0.2-1	Demonstrated the use of constrained PDE's to solve the forward and inverse of the frequency domain RTE simultaneously.

Table 1 continued

Reference	Imaging System	Contrast[+]	Forward Model	Reconstruction Algorithm	Model/ Phantom	Simulated/ Measured	Optical Properties[*]	Comments
Klose *et al.* 2005[36]	CW	Fluor.	3D RTE with discrete ordinates, source iteration, and upwind-step differencing	MOBIIR adjoint differentiation with gradient based optimization	4x4x1.3 cm with 2 fluorescent targets and 1 absorbing target	Measured	$\mu_s = 30$ $\mu_a = 0.4$ $g = 0.8$ fl target = 0.2 μM Cy5.5 $\mu_{a\_axf} = 0.05$	Extended 2D code to 3D and reconstructed experimental data using homogeneous endogenous background.
Patwardhan *et al.* 2005[71]	CW	Fluor.	Diffusion	Diffusion based ART	Mouse in intralipid	Measured	$\mu_s' = 10$ $\mu_a = 0.3$	Demonstrated scanning time-dependent measurements to assess bio-distribution of contrast agent.
Turner *et al.* 2005[72]	TD	Endo.	--	a) Filtered back-projection b) LSQR conjugate gradient with generalized Tikhonov regularization	1.5 cm thick intralipid chamber with 2 TiO_2 in resin targets	Measured	$\mu_s' = 7$ $\mu_a = 0.1$ $\mu_{a\_targ} = 0.8$	Examined use of complete angle projection data in reconstruction algorithms similar to those found in x-ray computed tomography.

Table 1 continued

Reference	Imaging System	Contrast[+]	Forward Model	Reconstruction Algorithm	Model/ Phantom	Simulated/ Measured	Optical Properties[*]	Comments
Xu *et al.* 2005[73]	FD	Endo.	Diffusion using second-differential spectral analysis	Diffusion based MOBIIR utilizing Levenburg-Marquardt algorithm	a) TiO_2 in gelatin b) mouse	Measured	a) contrast ratios: μ_s'= 0.64-1.55, μ_a =1.03-1.44 b) unspecified initial assumption	Implemented *a priori* information from MRI to improve spatial resolution and quantitative accuracy in reconstructions.

[+] Endogenous (Endo.), Fluorescence (Fluor.); * units are cm^{-1}

III. METHODS AND MATERIALS*

In this section, we discuss in detail the instrumentation used and developed in the course of this research as well as our approach to the simulation of photon transport. First, we describe the two main types of data acquisition approaches used to obtain frequency domain data, and the related instrumentation used to acquire the data in this dissertation. We then describe the basic phantoms used in these experiments and the models used to simulate the propagation of photons through the phantoms and tissues.

Data Acquisition and Instrumentation

The two major classifications of frequency domain instruments, homodyne and heterodyne, are distinguished by the manner in which the time dependent data is obtained. Homodyne data is obtained using a single frequency to acquire frequency-domain data, while heterodyne data is acquired by mixing two frequencies to obtain the frequency-domain data. In this section a description of each of these techniques as well as the associated instrumentation is presented.

Homodyne Technique

One of the major methods used to obtain the time dependent properties from frequency domain data is the homodyne technique.[74, 75] In this technique, a sinusoidally modulated image intensifier is phase locked with a modulated laser. A

* Reprinted with permission from "Radiative transport in fluorescence-enhanced frequency domain photon migration" by Rasmussen *et al.*, 2006. *Medical Physics*, accepted for publication, 2006 by American Association of Physicists in Medicine.

set of N evenly spaced phase delays from 0 to 2π relative to the phase of the modulated laser are introduced at the image intensifier. At each phase delay, a phase sensitive image is acquired. After N delays, the images are averaged to calculate the mean intensity (I_{DC}). I_{DC} contains information about the noise introduced to the phase sensitive images due to ambient light and the dark current or thermal noise inherent to the detection system. The mean intensity is subtracted from the phase sensitive images and the corrected images are arranged in the order of acquisition. The intensity at each pixel is followed through the set of images to obtain the modulated output as illustrated in Figure 15. A fast Fourier transform (FFT) is performed for each pixel (i, j), and the maximum frequency obtained for each pixel is used to calculate the phase ($\theta(i, j)$) and amplitude ($I_{AC}(i, j)$) as shown in equation (50).[74]

$$\theta(i,j) = \arctan\left(\frac{\mathrm{Im}\left[I(f_{\max})_{i,j}\right]}{\mathrm{Re}\left[I(f_{\max})_{i,j}\right]}\right)$$
$$I_{AC}(i,j) = \frac{\left(\left\{\mathrm{Re}\left[I(f_{\max})_{i,j}\right]\right\}^2 + \left\{\mathrm{Im}\left[I(f_{\max})_{i,j}\right]\right\}^2\right)^{1/2}}{N/2} \quad \textbf{(50)}$$

An instrument was assembled to collect data for comparison with the RTE forward solver. Figure 16 shows the basic schematic of the setup. The major components of the system include a charge coupled device (CCD) camera, an image intensifier, two frequency synthesizers, an NIR light source, a phantom, and some optical accessories. The intensity modulated laser light is delivered via a source fiber to the phantom. A set of fibers carry the detected excitation and emission light to the

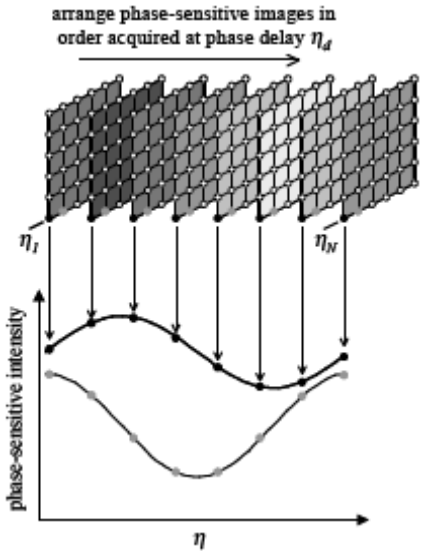

Figure 15: Illustration of the homodyne data acquisition method. (Reproduced with permission from Thompson et al.[75])

bundle faceplate where a Nikon lens focuses the image onto the photocathode of the image intensifier. The intensifier multiplies the detected photons, and the resultant light exiting the image intensifier is imaged by the CCD camera. The images are stored and processed on a 3.6 GHz personal computer with 2 GB of RAM. More detailed information is provided below for the major components of the homodyne instruments.

CCD Camera

The CCD camera system (Princeton Instruments PI-SCX, Roper Scientific) consists of the CCD camera, a controller, and a cooling unit. The CCD itself is an E2V 47-20 Grade 1 device with a 1024 x 1024 pixel active imaging area. The pixel size is 13 μm. The camera is a frame transfer camera and has a 1024 x 1024 frame storage area to store an image during transfer to the acquisition computer, while a

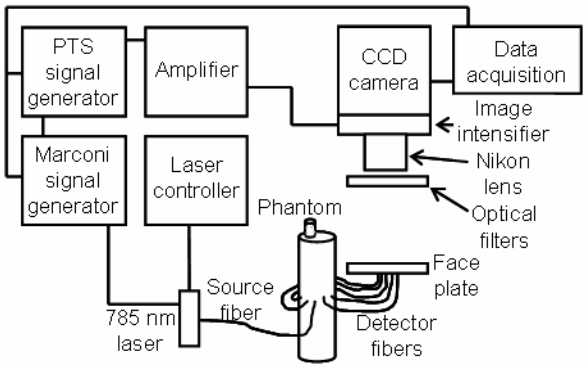

Figure 16: Schematic of instrumentation associated with the homodyne frequency domain system (reproduced with permission from Rasmussen *et al*.[55])

second image is being acquired, resulting in faster frame acquisition times. The camera is a 16 bit camera with 65,536 levels of digitization and two A/D converters operating at 100 kHz and 1 MHz. The camera has a 1.3:1 fiber taper to permit the fiber optical coupling of the image intensifier which allows for approximately 60% better light throughput as compared to lens coupled systems.[76] Another important feature of the CCD camera is the ability to integrate the image over time. As will be shown below, the ability to adjust the exposure time is particularly important when imaging low fluorescence signals. During data acquisition, the 1024x1024 pixel image is binned to 256 x 256 pixels to decrease memory requirements and increase data acquisition rates. The camera system is controlled via V++® software and the controller unit provided by Roper Scientific. The camera is cooled to -30°C with a combination of a thermoelectric Peltier device and a 50/50 ethylene glycol/water mixture.

Image Intensifier

A generation III image intensifier tube was coupled directly to the fiber taper on the CCD camera. When photons come into contact with the photocathode, they are converted into electrons. The electrons pass through a thin ion-barrier film to the microchannel plate (MCP) where they are multiplied. The multiplied electrons exit the MCP where they encounter the phosphor screen and are converted back to photons for detection by the CCD camera.[76] Some intensifier tubes are intended for use in night vision goggles and as such have an inverting fiber taper coupled to the phosphor screen. This taper rotates the image 180° prior to detection by the CCD. Figure 17 is a schematic illustrating the operation of an inverting image intensifier.

The ion-barrier film is located between the photocathode and the MCP and has the primary responsibility to protect the gallium arsenide (GaAs) photocathode from ionized gases present in the image intensifier. A portion of the electrons produced by the photocathode are absorbed by the film prior to reaching the MCP. There are often small holes or other defects present in the film due to the manufacturing process which permit electrons to pass through the film unimpeded. Typically these variations are not a concern, however when the image intensifier is operated in ultra-low light levels they start to show up as hot pixels, due to the higher percentage of electrons passing through the holes in the film compared to the surrounding area. Depending on the severity of the hot pixels, these variations can render the ICCD system useless at ultra-low light levels.

A micro power supply (GBS 20065400) provides the required voltages (see Figure 17) to operate the intensifier via a custom circuit. The circuit provides a means to introduce a 22 V radio frequency (RF) signal to the photocathode. The circuit, shown in Figure 18, essentially contains two electronic filters which isolate the RF signal from the micro power supply and the high dc voltages from the RF source.

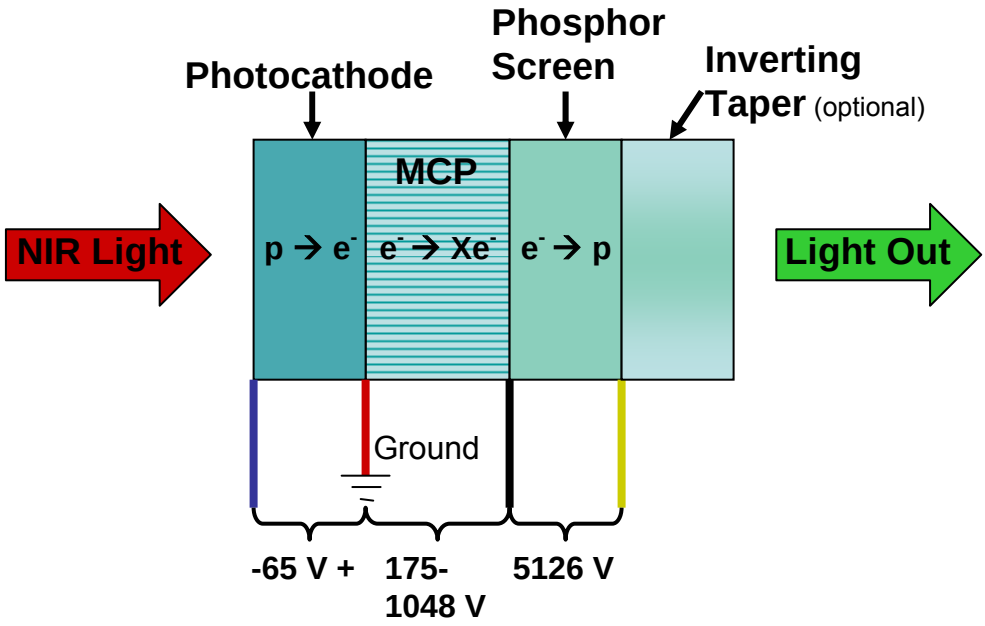

Figure 17: Schematic illustrating the internal operation of the intensifier. p represents a photon, e^- represents an electron, and Xe^- represents the multiplied electrons. Also shown are the voltages between the sections of the intensifier.

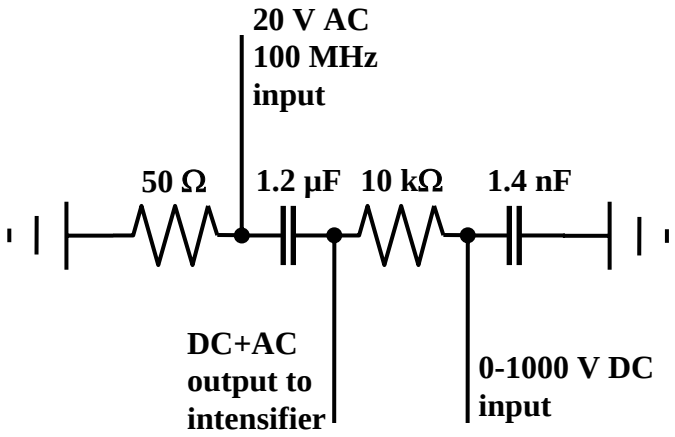

Figure 18: Schematic of custom circuit used to modulate the image intensifier for frequency domain measurements.

Frequency Synthesizers

Two frequency synthesizers are used to provide the needed sinusoidal signals for the homodyne data acquisition process. The master synthesizer is a Marconi 2022D which produces sinusoidal signals in the range of 10 kHz – 1 GHz. In these studies it typically modulates the laser diode at 100 MHz and supplies a 10 MHz standard signal to the second synthesizer.

The second (or slave) synthesizer, a PTS-310, is phase locked with the Marconi via the 10 MHz signal. To obtain homodyne data, a series of phase delays from 0 to 2π are introduced to the output of the PTS. The 13 dBm PTS signal is amplified using an ENI 604L RF amplifier and attenuated by a 20 dB attenuator to provide a 22V modulated signal to the image intensifier.

Light Source

In this proposal, an 80 mW, 785 nm laser diode (LD7140-201S, Thorlabs, Inc.) is used to provide the light required to excite the NIR fluorophores in the phantom. A diode controller (LDC 500, Thorlabs, Inc.) is used to provide a constant current and a temperature controller (TEC 200, Thorlabs, Inc.) maintains the diode at a constant temperature during operation. A 13 dBm, 100 MHz RF signal is superimposed onto the constant current to modulate the intensity of the laser diode output.

Optical Accessories

A Nikon lens (50 mm AF Nikkor) is used to focus the light from the faceplate onto the photocathode of the image intensifier. A combination of a bandpass filter (F10-830.0-4-2.0, CVI Laser Corp.) and a holographic filter (HNPF-785.0-2.0, Kaiser Optical Systems Inc.) are used to reject the excitation light while collecting the emitted light.

Heterodyne

The second common technique used to obtain frequency domain data is the heterodyne method. Figure 19 shows a schematic of the heterodyne instrumentation. In this method, a modulated (at frequency ω=100 MHz) laser beam is split into two beams, one of which is sent via fiber optics to a phantom containing the sample of interest and the second is sent directly to a photomultiplier tube (PMT) which is modulated at frequency $\omega+\Delta\omega$ ($\Delta\omega$=100 Hz). A collection fiber delivers the attenuated light from the sample to a second PMT where it also is amplified and mixed with a $\omega+\Delta\omega$ signal. The resulting amplified, superimposed signals pass through

transimpedance amplifiers which filter out the higher frequency (ω). The remaining Δω signals are digitized and collected on a computer using custom LabView® programs and the amplitude and phase shift of the sample signal are measured with respect to the reference signal as illustrated in Figure 9b. The major components of this setup include the light source, signal generators, PMT's, amplifier, transimpedance filters, and a computer for data acquisition.

Light Source

The light source used in this experiment is identical to the source used in the homodyne technique.

Signal Generators

The heterodyne setup uses two phase locked Marconi 2022d signal generators. The master generator produces a 100 MHz frequency signal which is used to modulate

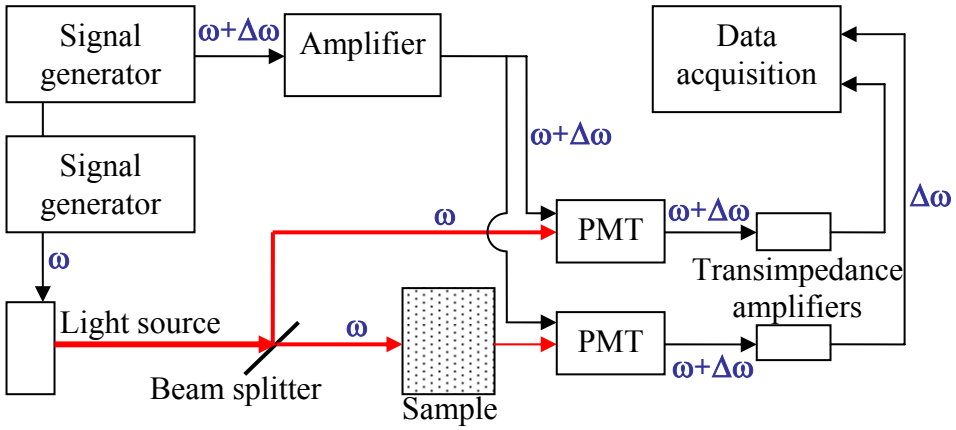

Figure 19: Schematic of a heterodyne instrumentation setup used to obtain frequency domain data.

the intensity of the light source. The secondary or slave generator produces a 100 MHz + 100 Hz signal which is amplified (ENI X), split, and sent to the PMT's.

Photomultiplier Tubes

The photomultiplier tubes are light detectors that have been designed to detect and amplify low light signals. When an incoming photon strikes the photocathode of the PMT, it is converted into an electron. As the electron travels down the tube, it encounters a series of dynodes where additional electrons are produced as illustrated in Figure 20. The overall gain or increase in electrons is related to the number of stages or dynodes and the voltage across each of the dynodes, and the newest designs have electron gains that can exceed 100 million. PMT's are typically very fast, have low noise with response times in the nanosecond range providing the capacity of amplifying modulated optical signals in the 100's of MHz range in real time. These attributes allow PMT's to produce precise frequency domain data, particularly in phase as long as the incoming optical signal is sufficiently strong. However, PMT's can only obtain one optical signal (or data point) at a time and when multiple data points are needed an optical switch or multiple PMT's are needed.

In the heterodyne setup, the PMT circuitry also provides an electronic mixer where the modulated signal detected by the PMT is mixed with the RF signal from the slave generator. The resulting signal is a 100 MHz signal on top of the 100 Hz offset as illustrated in Figure 21.

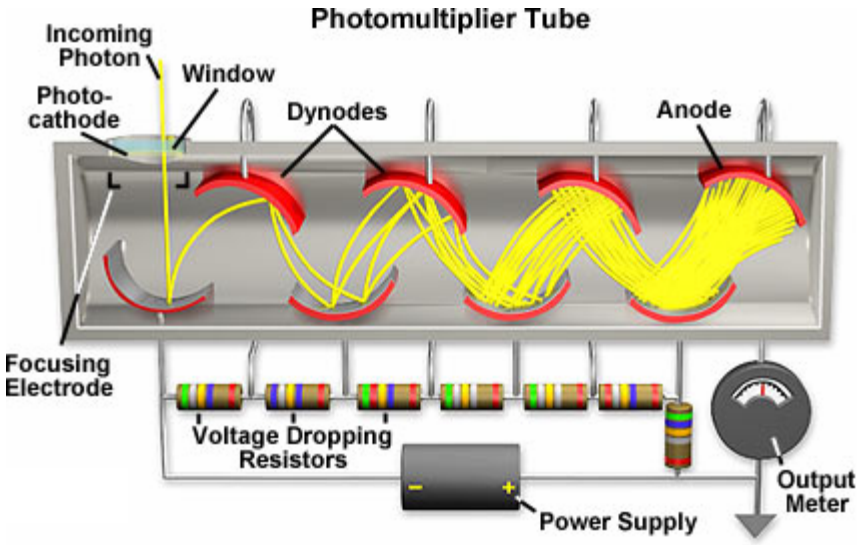

Figure 20: Schematic of a photomultiplier tube. As electrons propagate from one dynode to the other, additional electrons are produced. (reproduced with permission from http://micro.magnet.fsu.edu/primer/digitalimaging/concepts/photomultipliers.html)

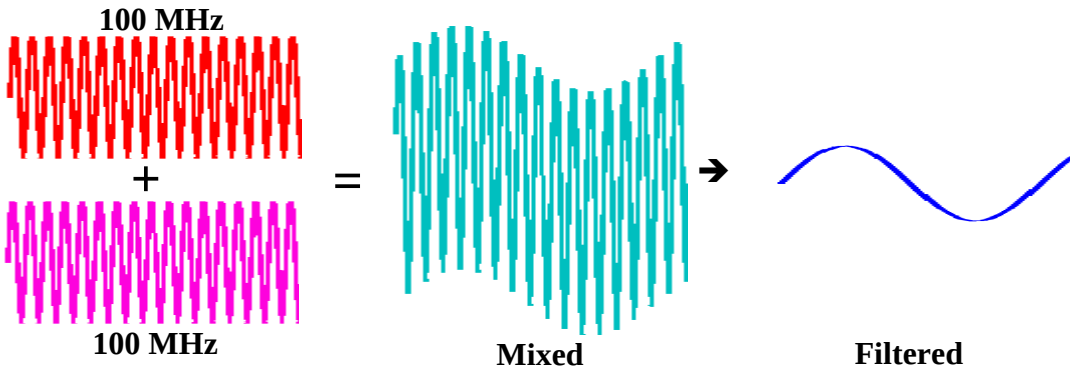

Figure 21: Illustration of the mixing and filtering of the heterodyne radio frequencies.

Transimpedance Amplifiers

The transimpedance amplifiers (Oriel 70710) serve as low pass electronic filters which remove the 100 MHz portion of the detected signals prior to data acquisition. This serves to reduce the frequency of the modulated signal to one that the computer can accurately sample. The transimpedance amplifiers also provide additional amplification of the detected signals.

Phantoms

The phantoms used in this dissertation were designed to represent the size and volume of a mouse. A one inch hole was typically drilled 4 inches deep in the center of a 3 inch diameter delrin® rod. The delrin® was black in color to inhibit the reflection of photons at the boundary of the phantom. Additional holes were drilled circumferentially around the plane two inches from the top of the cylinder and optical fibers were inserted and glued such that the polished tip of the fiber was flush with the inner wall of the delrin®. The large hole was then filled with different solutions of varying concentrations of intralipid to provide the desired scattering properties in the phantom. The optical properties of the intralipid solutions were measured using the heterodyne system in a technique described previously.[77]

While the specific details of each phantom will be described in the appropriate section, the desired contrast in optical properties were introduced into the system by inserting glass balls and/or glass NMR tubes filled with the desired contrasting intralipid solution. Absorbing targets were made by adding India ink to the intralipid solution. For void-like heterogeneities the glass targets were empty (air) or filled with

water. Fluorescent targets were made by diluting indocyanine green (ICG) in deionized water until the desired concentration was obtained (typically 1 μM). Figure 22 shows the chemical structure of ICG, while Figure 23 shows the excitation and emission spectra of ICG. In these studies, we excited the fluorophore at 785 nm and detected its emission at 830 nm. ICG is unique among all the fluorophores available for fluorescence imaging in that it has been approved for use in humans, and as such provides opportunities for bench to bedside translational studies. However, one of the major drawbacks to ICG is the lack of a functional group for attaching a peptide or antibody which prevents its use as a label for drug discovery or target efficacy studies. However, ICG is readily available and thus was used for the feasibility studies presented herein. There are other fluorophores with functional groups currently available and in the development phases for use in future targeting studies.

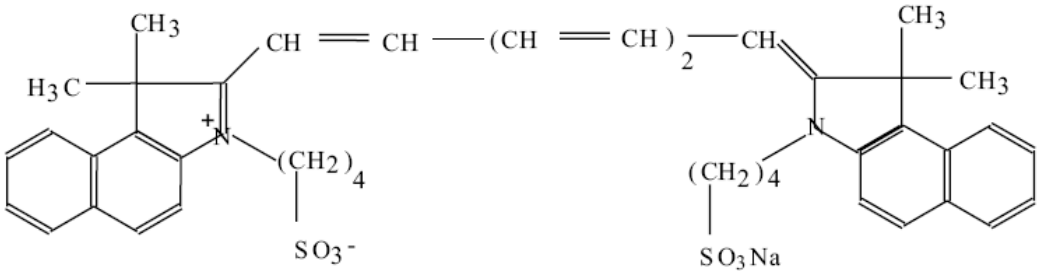

Figure 22: Chemical structure of indocyanine green. (Reprinted with permission from Urbanska *et al*.[78])

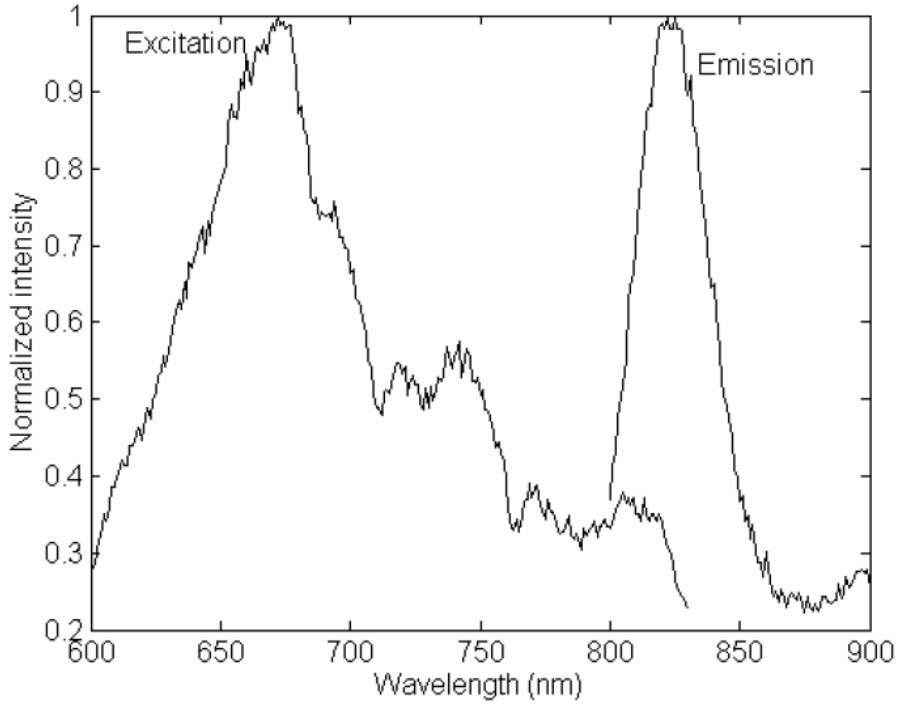

Figure 23: Excitation and emission spectra of indocyanine green.

Simulation of Photon Propagation

The general techniques used to model the forward propagation of photons in media were described in section II. In this section we describe in more detail how the RTE, Monte Carlo, and diffusion techniques are applied and used to obtain the predicted photon fluence in these studies.

Radiative Transport Equation

As discussed in section II the radiative transport equation is the general equation which describes the propagation of light in media. Typically, only one or two wavelengths or energies of light are used in small animal tomography, and equation (2) is simplified to the one energy form as shown below:

$$\frac{\partial\tilde{\phi}(\vec{r},\hat{\Omega},t)}{\partial t}+v\hat{\Omega}\cdot\nabla\tilde{\phi}(\vec{r},\hat{\Omega},t)+v\Sigma_t(\vec{r})\tilde{\phi}(\vec{r},\hat{\Omega},t)= \int_{4\pi}d\hat{\Omega}'v'\Sigma_s(\vec{r},\hat{\Omega}'\to\hat{\Omega})\tilde{\phi}(\vec{r},\hat{\Omega}',t)+s(\vec{r},\hat{\Omega}',t) \quad \textbf{(51)}$$

$\tilde{\phi}$ is the photon fluence and Σ_t is the total cross section of the media and is the sum of the scattering coefficient μ_s and the absorption coefficient, μ_a; Σ_s is the scattering cross section and describes both the distribution of the scattering properties as well as the directionality associated with the scattering events.

Equation (51) is the basis for all RTE based forward models in optical imaging. When continuous wave or time-invariant measurements are available, the steady-state form of equation (51) is used. For frequency-domain measurements, the fast Fourier transform of the RTE (equation (52)) is used

$$\frac{j\omega}{c}\tilde{\phi}(\vec{r},\hat{\Omega},\omega)+\hat{\Omega}\cdot\nabla\tilde{\phi}(\vec{r},\hat{\Omega},\omega)+\Sigma_t(\vec{r})\tilde{\phi}(\vec{r},\hat{\Omega},\omega)= \int_{4\pi}d\hat{\Omega}'\Sigma_s(\vec{r},\hat{\Omega}'\to\hat{\Omega})\tilde{\phi}(\vec{r},\hat{\Omega}',\omega)+s(\vec{r},\hat{\Omega}',\omega) \quad \textbf{(52)}$$

When fluorescence-enhanced techniques are employed, two equations are needed to describe the propagation of the excitation and emission wavelengths. Because the generation of fluorescence is dependent on the excitation fluence, these equations are coupled in the emission source term as shown below:

$$\begin{aligned}\frac{j\omega}{c_x}\tilde{\phi}_x+\hat{\Omega}\cdot\nabla\tilde{\phi}_x+\mu_t^x\tilde{\phi}_x&=\mu_s^x\int_{4\pi}p(\hat{\Omega}\to\hat{\Omega}')\tilde{\phi}_x d\hat{\Omega}'+s_x\\ \frac{j\omega}{c_m}\tilde{\phi}_m+\hat{\Omega}\cdot\nabla\tilde{\phi}_m+\mu_t^m\tilde{\phi}_m&=\mu_s^m\int_{4\pi}p(\hat{\Omega}\to\hat{\Omega}')\tilde{\phi}_m d\hat{\Omega}'+\frac{\varepsilon\mu_{a_{xf}}}{1+j\omega\tau}\phi_x.\end{aligned} \quad \textbf{(53)}$$

The subscripts and superscripts x and m represent excitation and emission wavelengths respectively and the dummy variable, *i*, is used below to represent *x* or *m* as appropriate. The term $\tilde{\phi}_i$ is the angular light fluence and is complex with amplitude and phase components; $j=\sqrt{-1}$; ω is the frequency at which the light is modulated; c is the speed of light in the medium; ε is the quantum efficiency of the fluorophore used; τ is the lifetime of the fluorophore. The total cross section, Σ_t^i now includes the absorption due to the fluorescent agent ($\mu_{a,fi}$) as well as the absorption and scattering of the surrounding tissue as shown in equation (54)

$$\Sigma_t^i = \mu_{a,fi}(\vec{r}) + \mu_{a,i}(\vec{r}) + \mu_s^i(\vec{r}). \tag{54}$$

$p(\hat{\Omega} \to \hat{\Omega}')$ characterizes the angular distribution of light as it is scattered throughout the medium. In this application, the Henyey-Greenstein function as shown in equation (55) is used,

$$p(\theta) = \frac{1}{4\pi}\frac{1-g^2}{\left(1+g^2-2g\cos\theta\right)^{3/2}} \tag{55}$$

where θ is the scattered angle (between $\hat{\Omega}'$ and $\hat{\Omega}$) and $g = \langle\cos\theta\rangle$ is the cosine of the average scattered angle and is called the anisotropy. The value of *g* is an indication of the forward peakedness of the scatter. When *g*=0 scatter is isotropic and when *g*=1 all photons are forward scattered (no scatter case).

One of the more powerful RTE solvers commercially available is the Attila® solver developed and marketed by Transpire, Inc. Originally developed at Los

Alamos National Laboratories, the Attila® solver typically uses discrete-ordinate angular discretization, linear discontinuous finite element method spatial differencing, and source iteration with a simplified diffusion synthetic acceleration techniques on three dimensional, unstructured meshes to obtain RTE solutions.[79, 80] The combination of these techniques has enabled Attila® to be adapted for use in a variety of applications including: nuclear reactor design and analysis, radiation shielding, medical radiation therapy, infrared radiative heat transfer, and charged particle calculations.

The Photon Migration Laboratory have collaborated with Transpire, Inc. to adapt the general framework of the Attila® solver for use in fluorescence-enhanced optical tomography. This collaboration has brought together Transpire's expertise in the numerical solution of the radiative transport equations and the Photon Migration Laboratory's expertise in optical physics, instrumentation, and tomographic techniques.

The original general solver framework is not capable of solving the coupled equations (equation (53)) directly because of the complex nature of the fluence ($\tilde{\phi}_i = \tilde{\phi}_i^{re} + j\tilde{\phi}_i^{im}$) in frequency domain. As such we split equation (53) into its real and imaginary components of angular fluence as shown below.

$$\begin{aligned}
&\frac{\omega}{c}\tilde{\phi}_x^{im} + \Omega\cdot\nabla\tilde{\phi}_x^{re} + \mu_t^x\tilde{\phi}_x^{re} = \mu_s^x\int_{4\pi} p\left(\hat{\Omega}\to\hat{\Omega}'\right)\tilde{\phi}_x^{re}d\hat{\Omega}' + S_x^{re}\\
&-\frac{\omega}{c}\tilde{\phi}_x^{re} + \Omega\cdot\nabla\tilde{\phi}_x^{im} + \mu_t^x\tilde{\phi}_x^{im} = \mu_s^x\int_{4\pi} p\left(\hat{\Omega}\to\hat{\Omega}'\right)\tilde{\phi}_x^{im}d\hat{\Omega}' + S_x^{im}\\
&\frac{\omega}{c}\tilde{\phi}_m^{im} + \Omega\cdot\nabla\tilde{\phi}_m^{re} + \mu_t^x\tilde{\phi}_m^{re} = \mu_s^m\int_{4\pi} p\left(\hat{\Omega}\to\hat{\Omega}'\right)\tilde{\phi}_m^{re}d\hat{\Omega}' + S_m^{re}\\
&-\frac{\omega}{c}\tilde{\phi}_m^{re} + \Omega\cdot\nabla\tilde{\phi}_m^{im} + \mu_t^x\tilde{\phi}_m^{im} = \mu_s^m\int_{4\pi} p\left(\hat{\Omega}\to\hat{\Omega}'\right)\tilde{\phi}_m^{im}d\hat{\Omega}' + S_m^{im}
\end{aligned} \tag{56}$$

where the real and imaginary components of the emission source

$$S_m = \frac{\varepsilon\mu_{a_{xf}}}{1+j\omega\tau}\phi_x \tag{57}$$

can be found by multiplying equation (57) by the complex conjugate $(1-j\omega\tau)$ and separating the real and imaginary components to obtain

$$\begin{aligned}
S_m^{re} &= \frac{\varepsilon\mu_{a_{xf}}}{1+\omega^2\tau^2}\left(\phi_x^{re} + \omega\tau\phi_x^{im}\right)\\
S_m^{im} &= \frac{\varepsilon\mu_{a_{xf}}}{1+\omega^2\tau^2}\left(\phi_x^{im} - \omega\tau\phi_x^{re}\right)
\end{aligned} \tag{58}$$

The real and imaginary equations described by equation (56) are solved using many of the same numerical methods described in section II. However, the one dimensional techniques have been extended to the full three dimensional problem. Summarizing these basic techniques, we use discrete ordinate techniques in which the angular propagation of the photons is restricted to a finite number of angles distributed on a unit sphere as defined by the angular quadrature or S_N order. The discrete ordinate equations are spatially discretized using a robust, 3-D linear discontinuous (LD) finite-element spatial differencing scheme to accurately predict the fluence across a wide array of optical properties while limiting refinement of the mesh to

regions where the solution is rapidly changing. The discretized RTE equations are solved by source iteration. A modified diffusion synthetic acceleration (DSA) method, specifically designed for the 3-D linear discontinuous finite differencing scheme, is used to accelerate the iterative convergence rate for scattering dominated problems.[81, 82] Scatter is modeled using the associated Legendre polynomial expansions (P_n) of the scattering cross sections.

A variety of angular quadrature sets are available in the Attila® software, including level symmetric, Chebyschev-Legendre, and Chebyschev-Lobatto quadratures. For most of the simulations presented here in, a triangular Chebyschev-Legendre quadrature was used. At this time, access to the research article (Technical Report LA-11342-C) containing the actual mathematical formulation of this quadrature is restricted by the federal government, therefore the details are not presented here. However, in this approach, N^2+2N quadrature angles are generally distributed uniformly around the unit sphere, with the exact orientation determined using Gauss-Legendre and Chebyschev polynomials.[79] User defined quadrature sets can also be entered as needed.

When the excitation light source is a point source, a first scattered distributed source (FSDS) method is used to solve the RTE equations. Using this technique, the transport problem is split into two components. First an analytic component determines the distribution of non-scattered photons by analytically 'ray tracing' photon paths from the source to each tetrahedron in the grid. During this process, a custom quadrature set containing only those ordinates whose direction falls within a

specified numerical aperture can be introduced. This allows the user to more realistically model the output of optical fibers and other light sources which emit light within a specified numerical aperture. The non-scattered flux, as determined in the 'ray tracing' step, is then used to create a new, first scattered source from which the remaining 'scattered' solution is obtained using the discrete ordinate techniques discussed above. The solutions to both parts are added to produce the full solution. To accurately model the numerical aperture of a detector, the Attila™ package provides a special purpose edit based upon integral transport theory.[33]

Unidirectional, collimated sources can be modeled with the FSDS approach by applying a narrow numerical aperture to the source and placing it far away from the grid, or alternatively, a planar source can be used in a standard discrete-ordinate calculation by making use of the Chebyschev-Lobatto quadrature sets.

In our simulated problems, the optical properties are assumed as knowns and the fluorescent RTE code solves the equations for the real and imaginary components of the fluence. The amplitude is then obtained by

$$I_{AC,i} = \sqrt{REAL(\phi_i)^2 + IMAG(\phi_i)^2} \tag{59}$$

and the phase by

$$\theta_i = \tan^{-1}\left(\frac{IMAG(\phi_i)}{REAL(\phi_i)}\right). \tag{60}$$

Monte Carlo

Monte Carlo techniques were also developed as a means to numerically verify the results obtained using the RTE solver. The Monte Carlo algorithm describing fluorescence generation and propagation was developed by Dr. Tianshu Pan and is based on an algorithm presented by Vishwanath *et al.*[83] Our algorithm along with some comparisons with RTE, diffusion, and heterodyne experimental data is in preparation for submission to *Medical Physics*[84] and is outlined below.

While many of the features of the basic Monte Carlo algorithm described in section II are also present in our Monte Carlo algorithm, the major distinction of this algorithm lies in the modeling of the generation and propagation of fluorescence light. Briefly, a packet of excitation photons with a unit of weight, *w*, is launched into the media. As the packet propagates through the media it undergoes a series of scattering and absorption interactions. We note upfront that unless otherwise stated, every appearance of ξ represents a new independently generated random number uniformly distributed between 0 and 1. Each random number is used once and discarded.

The scattering step size, s_i, for the i^{th} step is determined by

$$s_i = l_x\left[-\ln(\xi)\right] \tag{61}$$

where l_x is the average scattering path length between scattering events and is determined by

$$l_x = \frac{1-g}{\mu'_{s,x}}, \tag{62}$$

g is the anisotropic factor and $\mu'_{s,x}$ is the isotropic scattering coefficient of the media at excitation wavelength.

The probability, P, that the excitation photon package will convert to an emission photon packet during the i^{th} migration step is calculated by

$$P = 1 - \exp\left(-\mu_{a_{xf}} s_i\right), \tag{63}$$

where $\mu_{a_{xf}}$ is the absorption coefficient of the media due to fluorophore. Another random number, ζ, is generated and, depending on the comparison of ζ to P, one of two algorithmic paths are taken. When $\zeta \geq P$, no fluorescence is generated; when $\zeta \leq P$, the excitation packet is converted to fluorescence.

In the first scenario, $\zeta \geq P$, the excitation photon packet is not converted to emission photons and the excitation photon weight is attenuated by

$$w_i = w_{i-1} \exp\left(-\mu_{a_x} s_i\right), \tag{64}$$

where $w_{i\text{-}1}$ and w_i are the photon weights before and after the i^{th} step, and μ_{a_x} is the absorption coefficient of the media at the excitation wavelength.

The time increment due to the scattering is calculated by

$$t_i - t_{i-1} = \frac{s_i}{c/n}, \tag{65}$$

where c is the light speed in a vacuum and n is the refractive index.

The change in the photon packet's direction of travel due to scattering is determined by a deflection angle, θ, and an azimuthal angle, φ. The deflection angle ranges from 0 to π and is determined by the Henyey-Greenstein phase function[85],

$$\cos\theta = \frac{1}{2g}\left\{1 + g^2 - \left[\frac{1-g^2}{1-g+2g\xi}\right]^2\right\}. \tag{66}$$

The azimuthal angle ranges from 0 to 2π and is calculated by sampling

$$\varphi = 2\pi\xi\,. \tag{67}$$

It is important to note that the ξ's in equations (66) and (67) are independently generated random numbers uniformly distributed between 0 and 1.

When $\zeta \le P$, all the excitation photons are 'converted' to emission photons, and the weight of the emission photon packet is immediately attenuated by

$$w_i = w_{i-1}\varepsilon\exp\left(-\mu_{a_m} s_i\right), \tag{68}$$

where μ_{a_m} is the absorption coefficient at the emission wavelength and ε is the fluorophore quantum efficiency.

The time increment associated with this path includes the time lag due to both the flight time and fluorescence lifetime, τ, and is expressed as

$$t_i - t_{i-1} = \frac{s_i}{c/n} + \tau\left[-\ln\left(\xi\right)\right]. \tag{69}$$

The new travel direction, $\vec{v} = (v_x, v_y, v_z)$ can be in any direction due to the isotropic emission of fluorescent light and is determined by

$$\vec{v} = \begin{cases} \cos(2\pi\xi)\sqrt{1-(\xi')^2}, \\ \sin(2\pi\xi)\sqrt{1-(\xi')^2}, \\ 2\xi'-1 \end{cases} . \quad \textbf{(70)}$$

where ξ and ξ' are independently generated random numbers.

The subsequent migration of the emission photon package is similar to that of an excitation photon package, except that the optical properties at the emission wavelength are used for all subsequent steps. The overall process is outlined in Figure 24. Additional photon packets are launched until the stored solution reaches a statistically significant result, which due to the small volume and the generation of fluorescence can mean 600 million excitation photon packets are needed, requiring ~24 hours of computation time. After all packets have been processed, a FFT is taken on the resulting time domain data to obtain frequency domain amplitude and phase.

Diffusion Approximation

The diffusion approximation (equation (42)) is solved using finite element methods as developed and reported previously by members of the Photon Migration Laboratory and past collaboration with Dr. Eppstein and her laboratory at the University of Vermont.[86] Briefly, using the Galerkin approximation and standard finite element techniques,[87] each of the coupled diffusion equations were reduced to a set of equations which were then solved to obtain the real and imaginary parts of the

excitation and emission fluence. For detailed derivation of the finite element equations for the coupled diffusion equations, see Godavarty.[86]

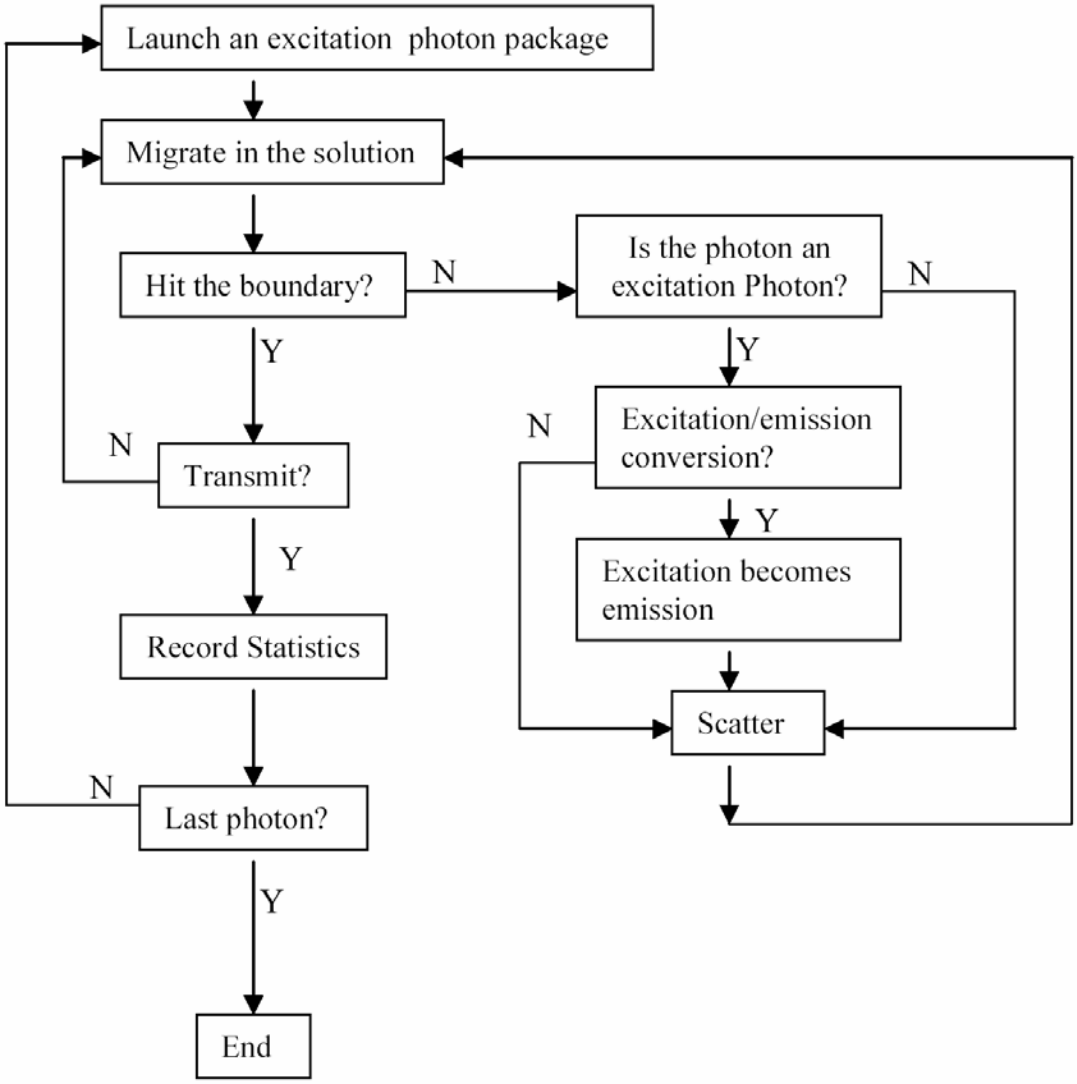

Figure 24: Flowchart of developed Monte Carlo algorithm for tracing both excitation and emission photon trajectories. (reproduced with permission from Pan *et al.*[84])

IV. INTRUMENTATION AND THE PHASE MEASUREMENT

In this section some of the challenges of acquiring frequency domain measurements are addressed. Particular emphasis is placed on the difficulties related to the phase measurement on the small volumes sampled in small animal optical tomography. Some comparative data between the homodyne and heterodyne instruments are also presented.

The Phase Measurement

One of the distinct advantages of optical tomography based on time-dependent measurements is the increased information the time or phase measurement provides. However, the phase measurement's usefulness is directly related to the noise levels of the instrument itself. Previous experiments using the ICCD homodyne instrument typically involved large diffusive volumes where the light was multiply scattered, resulting in a relatively large (as compared to the instrument noise) time lag between introduction and detection of the photons. In the small and non-diffusive volumes of interest in small animal tomography, however the time lag associated with the propagation of the light through the volume can be very small. Thus, the noise floor associated with instrumentation may begin to impact the quality of the phase measurement.

Sources of Noise in Phase Measurement

Instrumentation noise can often be classified as systematic or random. Systematic noise is introduced into the measurement consistently every time the instrument is used. Some sources of systematic noise in the phase measurement

include optical fiber length, position, and location, the phase offset between the signal generators, the drift of the phase during experiment due to instrument instabilities, and other small consistent deviations due to the nature of the instrumentation. When systematic error is constant, some of its effects can be calibrated out to improve the acquired data.

When errors are not consistent and appear randomly throughout the experiment, they are considered random errors. Some sources of this error can include the effects of RF leakage in the electronic components of the circuitry driving the instruments and the response of the detectors themselves. Due to its inconsistent and irregular nature, random noise is very difficult to account for in a way that reduces its affect on the acquired data.

Calibration of Phase Data

The type of noise and its impact on the acquired data varies from instrument to instrument. In our laboratory, we have generally observed that the homodyne system tends to have a higher noise floor than the heterodyne system. We have also observed that in some heterodyne systems that random noise tends to dominate the systematic noise. Although we can correct for the systematic errors,[75, 88] to date our efforts to account for and calibrate out the random noise has largely proved ineffective. The amount of random noise present in the homodyne phase measurement varies between intensifiers. While no one specific cause has been identified, it could due to inherent differences between the types of intensifiers, and/or the custom circuit built to drive the intensifiers. On the other hand, the systematic noise of the heterodyne system

dominates and efforts to calibrate the phase data have shown some success as discussed below.

Homodyne System

The major component of the systematic phase error of the homodyne system is the phase difference between the Marconi and PTS signal generators. The two generators are phase locked such that the phase difference between the two remains constant. However, the actual phase difference changes every time the instruments are turned off and on again resulting in arbitrary phase differences between data acquisition sessions. To verify that this was indeed the case, we set up a small experiment in which we turned the PTS signal generator off and back on three times and then collected frequency domain data from a 1.0% intralipid phantom. Figure 25 shows a log plot of the raw intensity versus phase delay as a function of PTS initialization. Each time the PTS was restarted, the phase of the homodyne data is shifted. When the FFT of the experimental data was taken, the difference in the starting location affected the detected phase (Figure 26) but not the detected amplitude (Figure 27).

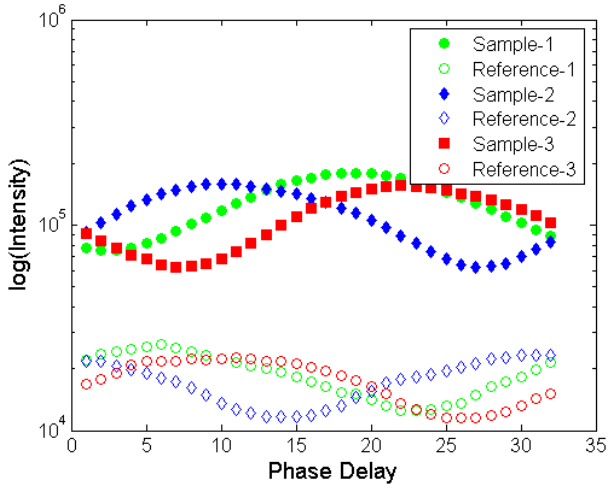

Figure 25: Intensity of the detected excitation light from a reference fiber and a sample fiber as a function of PTS initialization (turning off and on).

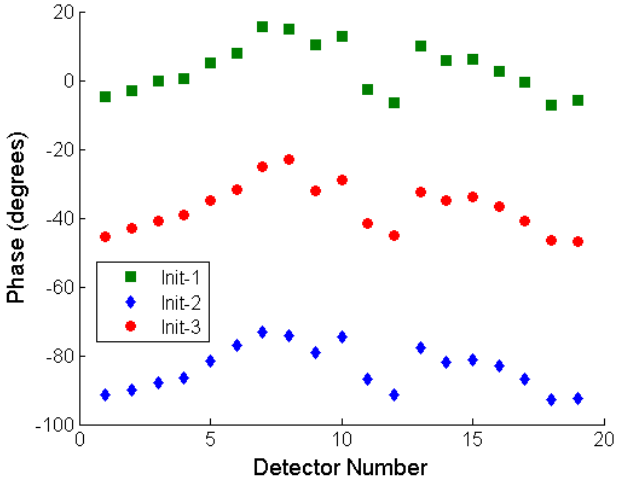

Figure 26: Phase versus detector number as a function of initialized phase difference between the PTS and Marconi signal generators in the homodyne system.

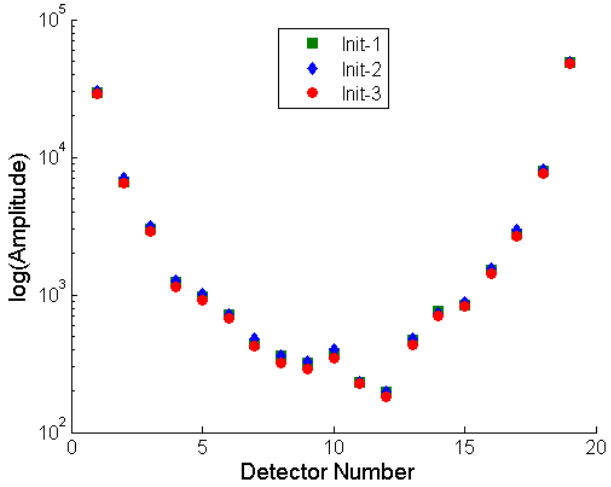

Figure 27: Amplitude versus detector number as a function of initialized phase difference between the PTS and Marconi signal generators in the homodyne system.

Typically we account for the difference in the phases by adding a constant to the measured phase to shift it up or down as needed to align it with the predicted phase of the forward model. While convenient, this technique did not permit us to experimentally verify that the absolute phase predicted by the forward models was correct. To verify that predicted phase was correct, we needed a way to experimentally remove the phase shift introduced by the signal generators. This was accomplished by performing another series of experiments (on a 0.5% intralipid phantom) in which the phase difference between the signal generators was actually measured prior to a obtaining the homodyne data. To do this, we first connected the outputs of the two signal generators to the inputs of an oscilloscope (Tectronixs. TDS 744A) and started the homodyne acquisition routine. Fifty phase difference measurements were acquired on the oscilloscope and the signal generator outputs were

then shifted to the laser and image intensifier prior to the image acquisition. During data acquisition, the average of the phase difference data obtained from the oscilloscope was subtracted from the measured data. Figure 28 and Figure 29 show the measured frequency domain phase before and after adjustment as compared to the phase predicted using the RTE solver. As can be seen, the measured phase differences correspond well with the constant phase offsets. The small constant difference between the adjusted phase and the predicted phase may be attributed to the phase lag due to the instrumentation, such as the intensifier circuitry, laser diode, and fiber optics, not included in the phase difference measurement. Thus we can justify adding or subtracting the arbitrary phase constant as needed to line up the measured phase with the absolute phase predictions of the forward models.

In Figure 29, the random nature of the phase measurement becomes apparent particularly in the measurements with lower light levels. This is evidenced in both the large error bars on the data as well as the scatter between the different sets of measurements. It is also noted, that the increase in random noise in Figure 29 as opposed to Figure 26 seems to be due to the use of a different image intensifier (the first being irreparably damaged during an experiment). The second intensifier has an inverting optical fiber plate, and seems to have an inherently higher random noise level than the original intensifier. Whether this increase in random noise is due to light losses associated with the additional inverting fiber optic plate, or whether it is just a characteristic of this particular intensifier is not known. However, the large random error inhibits the ability to calibrate out the systematic noises that may be

present. A different intensifier of the same type used to acquire the data in Figure 26 may decrease the random nature of the measurement, but was not available due to the manufacturer's limited supply during the course of this research.

In general, the lower the light signal being detected and/or the less phase contrast (phase shift due to light propagation) in the phantom, the more effect the random noise has on the system and the larger the error bars of the measurement.

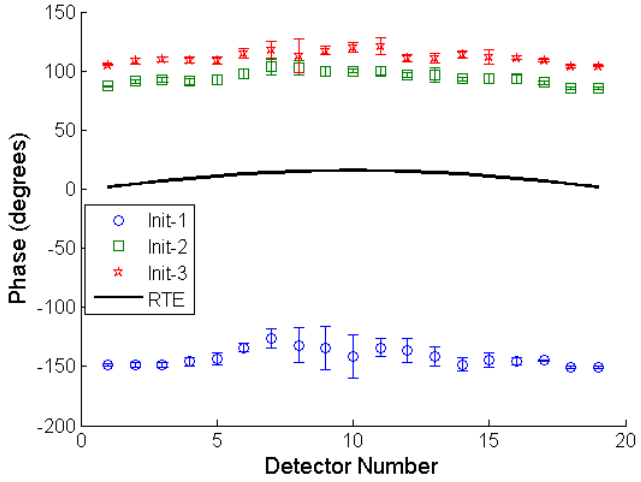

Figure 28: Phase offset of three sets of measurements as a function of initialized phase difference between the PTS and Marconi signal generators in the homodyne system.

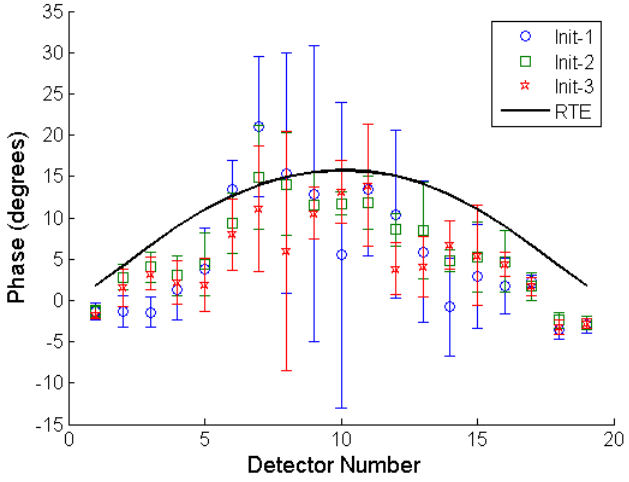

Figure 29: Adjusted phase offset of three sets of measurements as a function of initialized phase difference between the PTS and Marconi signal generators in the homodyne system. Init-1 was adjusted by 147.3°, Init-2 by -88.3°, and Init-3 by -106.8°.

Heterodyne System

The PMT detectors used in the heterodyne system were specially selected for their matched performance and low internal noise floors. As such, when they receive sufficient input signal, they are able to intensify the signal with relatively little distortion. Thus the random noise floor of the heterodyne system is extremely low and systematic errors in the phase measurements can more easily be accounted for.

For the heterodyne case, we performed a simple calibration step similar to that of Jiang *et al*.[89] In this scheme, we performed several experiments using 2% and 3% intralipid solutions with known optical properties in our 1 inch diameter phantom with nineteen detector fibers placed circumferentially about its middle. We chose these higher concentrations because we were confident that the diffusion equations would

accurately model the propagation of light to all nineteen fibers regardless of their proximity to the source fiber. The calibration factors ($\theta_{c,i}$) for each detector fiber (i) were then calculated as the difference between the actual measured phase ($\theta_{meas,i}$) and the prediction ($\theta_{diff,i}$) by the diffusion model as shown below.

$$\theta_{c,i} = \theta_{meas,i} - \theta_{diff,i} \quad \textbf{(71)}$$

The calibration factors obtained from the 2% and 3% intralipid solutions were averaged to obtain a calibration factor that would be used for all subsequent heterodyne phase measurements regardless of phantom composition. These calibration factors are applicable to all subsequent measurements, because they take into account only the phase change due to the instrumentation, which is the major source of systematic noise. Calibration is done by adding the calibration factor to the measured data. Figure 30 illustrates the effect of this calibration procedure on a data set obtained from a 1.0% intralipid solution. Calibration was not done for amplitude due to the low systematic noise in the intensity measurements of the PMT's.

Comparison of Homodyne and Heterodyne Measurements

Because of the difficulty we have in obtaining low noise phase data on the homodyne system we investigated the feasibility of constructing a PMT based system to obtain data for small animal tomography. In this section we present several examples of data that we obtained from both the heterodyne and homodyne systems.

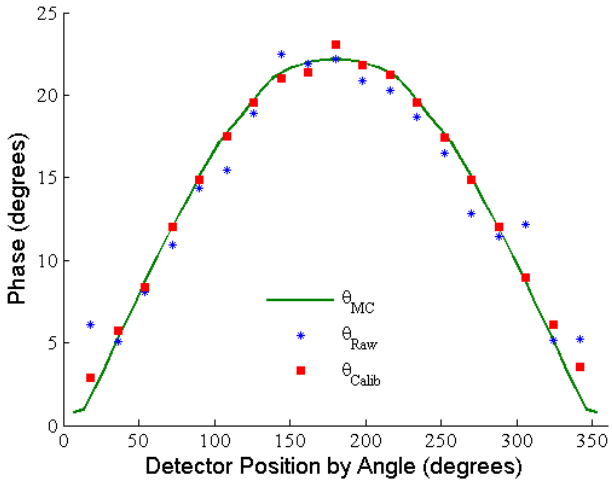

Figure 30: Comparison of a Monte Carlo prediction to raw and calibrated phase data obtained in a homogeneous 1.0% intralipid phantom.

The first comparison was of a homogeneous 1.0% intralipid solution with 1.0 μM ICG. We collected both excitation and emission data from the heterodyne and homodyne systems as shown in Figure 31. The amplitude data compares well with small error bars in both sets of measurements. The averaged phase data also compares well, but the error bar on for the homodyne system is quite large illustrating the higher noise floor in the homodyne system.

Additional experiments with ICG mixed homogeneously in different concentrations of intralipid were also performed. While not shown here, the data further illustrated the ability for the homodyne and heterodyne systems to obtain comparable amplitude and phase measurements in systems, with the homodyne system having consistently larger error bars in the phase measurements.

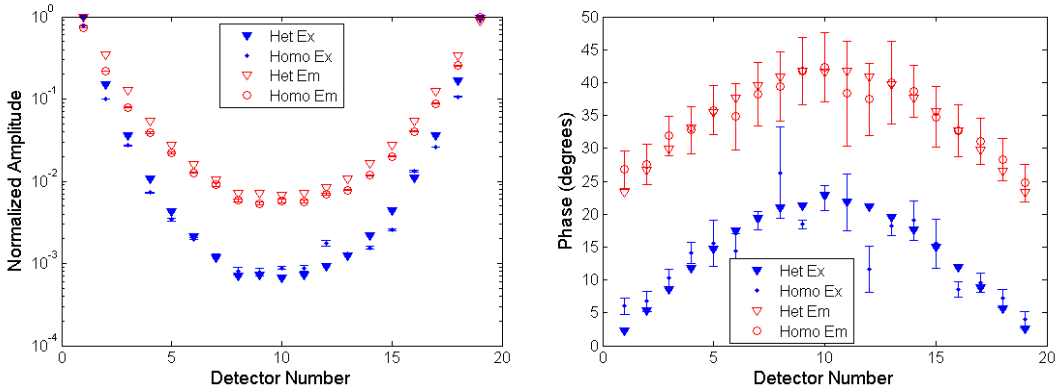

Figure 31: Comparison of (a) normalized excitation (Ex) and emission (Em) amplitude data and (b) excitation (Ex) and emission (Em) phase measurements obtained from the heterodyne (Het) and homodyne (Homo) systems. Phantom consisted of a homogeneous 1.0% intralipid solution with 1.0 µM ICG. The error bars for the heterodyne system are not shown as they are less than 0.1% for both amplitude and phase.

The next set of experiments was designed to compare the two systems was based on a phantom filled with a 0.5% intralipid solution containing a 3 mm diameter NMR tube filled with a 2.0 µM ICG solution. In this case, because the ultra low levels of emission light arriving at the PMT were below the noise floor of the PMT we were unable to obtain amplitude or phase data at the emission wavelength from the heterodyne system. On the other hand, because of our ability to adjust the exposure time of the images during data acquisition, we were able to obtain homodyne data for both the excitation and emission wavelengths as shown in Figure 32.

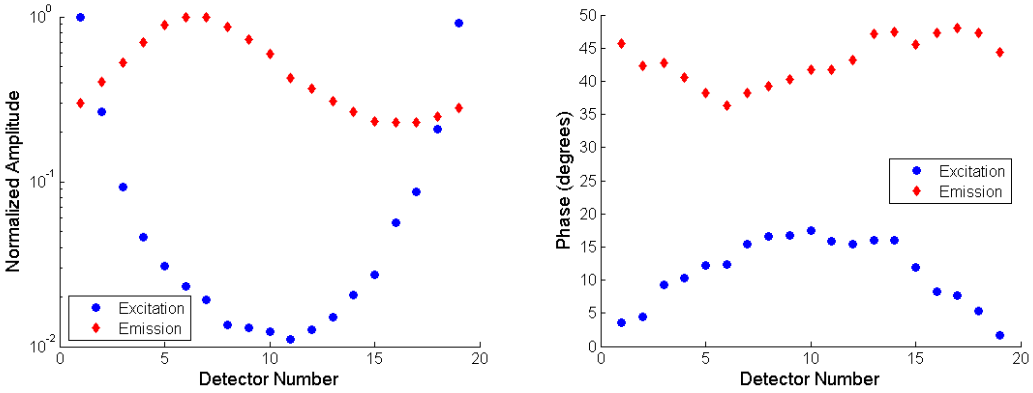

Figure 32: (a) Amplitude and (b) phase data collected using the homodyne system with a 0.5% intralipid solution containing a 3 mm diameter NMR tube.

Conclusions

While the heterodyne system typically has a lower noise floor and hence provides more accurate phase measurements as compared to the homodyne system, it can only provide useable data when the detected light level is above the noise floor of the PMT. The homodyne system's ability to integrate the detected signal with time is crucial in detecting the ultra low emission signals that will be present in small animal tomography data. Thus, in spite of its high noise floor in the phase measurements of this particular intensifier, we will continue to use homodyne system in the design and construction of a small animal tomography system.

V. COMPUTATIONAL VALIDATION OF RTE FORWARD

One of the major advantages of the radiative transport equation is the ability to accurately model the propagation of photons in the presence of both diffusive and transport limited optical properties. In this section, we examine the ability of our RTE solver to accurately account for (i) different modulation frequencies, (ii) different lifetimes, and (iii) the high anisotropy or forward peaked nature of light scattering in tissues. We also examine the ability of the solver adequately predict the fluence of photons in diffusion and transport limited systems. The predictions of the RTE solver were compared with the standard diffusion and Monte Carlo methods used in the optics community.

The phantom used in these studies was a cylinder 4 inch tall and 1 inch in diameter. A mesh consisting of 24,402 nodes and 124,881 elements as shown in Figure 33 is used for both RTE and diffusion simulations. The detector locations are equally spaced around the center plane in a counter-clockwise orientation. For simulations in which the RTE predictions are compared to Monte Carlo, the sources are modeled as point sources with a numerical aperture equivalent to 17°. Isotropic sources are used when RTE and diffusion predictions are compared. In figures containing experimental data, the detectors are numbered while for figures with no experimental data, the detector locations are plotted with respect to the angular location with respect to the center of the phantom and the source location.

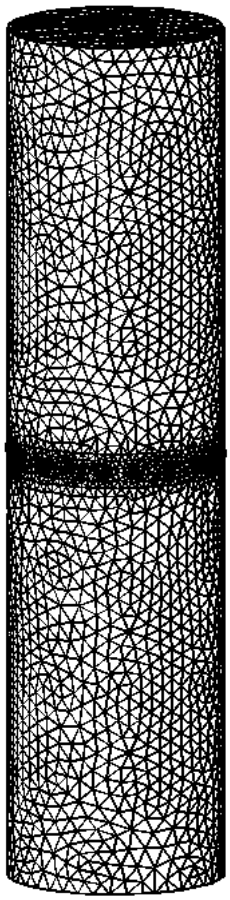

Figure 33: Illustration of the RTE and diffusion mesh used in these studies. The mesh contained 24,402 nodes and 124,881 tetrahedral.

Effect of Source Frequency

To verify that our RTE solver can accurately account for the modulation frequency of the incident light, we ran a series of simulations using Monte Carlo and the RTE solver simulations with modulation frequencies of 70, 80, 90, and 100 MHz. The excitation light was modeled as a point source with a numerical aperture of 0.39. The phantom was filled with a 1% intralipid solution with optical properties of $\mu'_{s,x}$ =

10.33 cm^{-1}, $\mu_{a,x}$ = 0.025 cm^{-1}, and g = 0.64. The Monte Carlo and RTE simulated phase data and experimental data from the heterodyne system are graphed in Figure 34 demonstrating the ability of the RTE solver to model the phase shift as a function of the modulation frequency of the incident light. The amplitude data was not affected by the incident frequency (data not shown).

Effect of Fluorophore Lifetime

We also ran different RTE and Monte Carlo simulations in which the lifetime (τ) of the fluorophore was varied to verify that the RTE solver could correctly account for the phase delay of the emission light due to changes in τ with different fluorescent contrast agents. For this study, the optical properties of the phantom were $\mu'_{s,x}$ = 6.84 cm^{-1}, $\mu_{a,x}$ = 0.027 cm^{-1}, $\mu_{a,xf}$ = 0.17 cm^{-1}, $\mu'_{s,m}$ = 5.7 cm^{-1}, $\mu_{a,m}$ = 0.026 cm^{-1}, $\mu_{a,mf}$ =

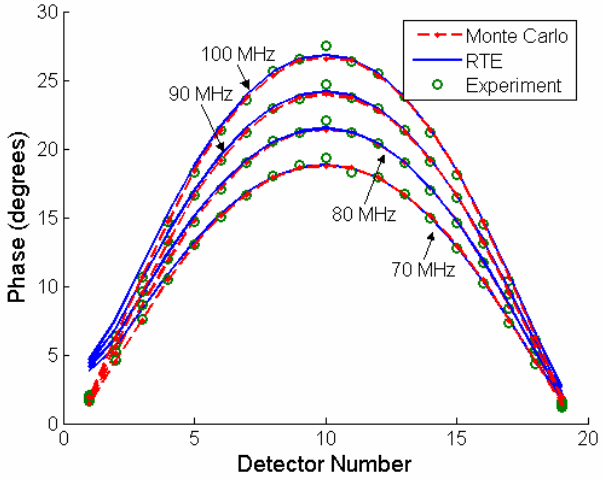

Figure 34: RTE and Monte Carlo phase predictions and experimental phase measurements as a function of the source modulation frequency in a 1.0% intralipid solution.

0.20 cm^{-1}, and g=0.64. The lifetime was simulated as 0.1, 0.56, and 1.0 ns. The Monte Carlo and RTE results are plotted as a function of τ in Figure 35, and demonstrate the ability of the RTE solver to accurately account for the changes in emission phase due to the lifetime of the fluorophore. While the Monte Carlo and RTE emission amplitude predictions due not coincide in this case, the predictions of each solver as a function of lifetime coincide demonstrating that τ only impacts phase.

Effect of Anisotropy

When photons interact with a material, they are absorbed or scattered. The anisotropic factor (g) is a measure of the forward scattering properties of the material, and is defined as the average cosine of the scattered angles. When g=0, the photons undergo pure isotropic scatter and when g=1, the photons are all forward scattered. Tissues typically have high anisotropic factors, ranging from g=0.74 in skin to g=0.98

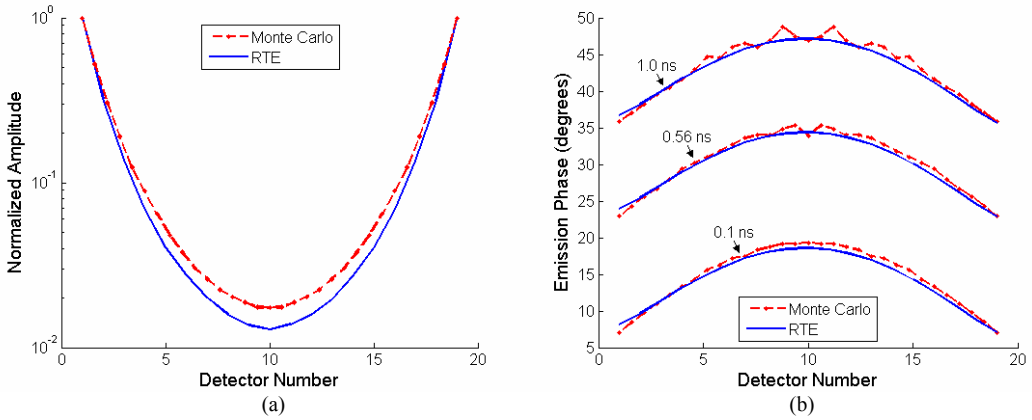

Figure 35: RTE and Monte Carlo simulation of emission (a) amplitude and (b) phase as a function of the lifetime of the fluorophore in a 0.5% intralipid solution. (part b is reproduced with permission from Pan *et al.*[84])

in the heart.[46] In the small volume of a mouse, photons may not undergo sufficient scattering events to loose the directionality associated with the incident light. Thus the impact of the anisotropic factor is important in the accurate modeling of light propagation particularly in those regions of the mouse that have a higher *g*. For validation, we investigated the effect of the anisotropic factor (*g*) on the solution of the RTE solver. To do this we modeled the propagation of light (ω = 100 MHz) through a cylindrical phantom with a height of four inches and a diameter of 1 inch. The phantom was assumed to be a scattering material containing a 1 μM ICG mixed homogeneously throughout with optical properties of $\mu_s' = 10$ cm^{-1}, $\mu_{a,x} = 0.0306$ cm^{-1}, $\mu_{a,xf} = 0.208$ cm^{-1}, and $\mu_{a,m} = 0.165$ cm^{-1}. The incident or source light was modeled as a point source with a numerical aperture of 0.39. For this study, the anisotropic factor was varied between 0.0 and 0.9. As *g* changes so does the isotropic scattering coefficient ($\mu_s' = \mu_s(1-g)$) which provides an indication of the distance photons must travel before being isotropically scattered. When $g = 0.0$, $\mu_s' = 10$ cm^{-1} which represents a mean isotropic scatter length of 0.1 cm. On the other hand, when g=0.9, $\mu_s' = 1$ cm^{-1} with a mean isotropic scatter length of 1 cm. One of the assumptions made in the derivation of the diffusion approximation was that the detectors must be at least 10 isotropic scattering path lengths from the source. Thus when g=0.9, the detectors need to be ~10 cm away from the source in order for the photons to be considered diffusive. RTE and Monte Carlo simulations were performed for *g* values

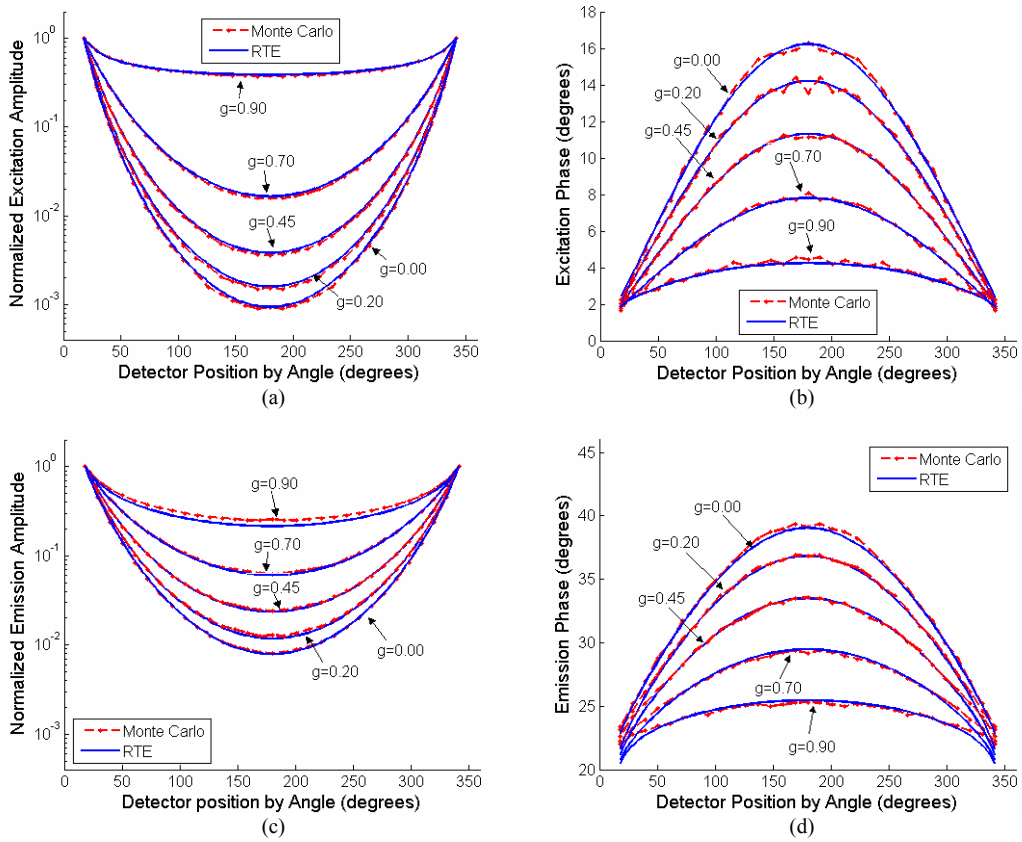

Figure 36: Predictions of (a) normalize excitation amplitude; (b) excitation phase; (c) normalized emission amplitude; and (d) emission phase versus detector position as a function of *g*. ω = 100 MHz with $\mu_{s,x} = \mu_{s,m} = 10$ cm^{-1}, $\mu_{a,x} = 0.0306$ cm^{-1}, $\mu_{a,xf} = 0.208$ cm^{-1}, $\mu_{a,m} = 0.165$ cm^{-1}, and NA = 0.39.(Reproduced with permission from Pan *et al.*[84])

of 0.0, 0.2, 0.45, 0.7, and 0.9. Figure 36 illustrates the resulting amplitudes and phase predictions for both the excitation and emission wavelengths. The predictions of the RTE solver and Monte Carlo correspond well, indicating the ability of the RTE to correctly account for the wide range of anisotropic properties of materials.

The Diffusion Limit

Because small animals possess both transport limited and diffusive regions, the RTE solver must have the ability to efficiently and accurately predict the fluence in both regions. It has been shown that, when the transport theory approaches a particular asymptotic limit, it transitions into diffusion theory.[34, 82] This asymptotic limit is known as the diffusion limit. When numerical techniques are employed to solve the RTE, there must be consistency in the discretization such that the solver maintains the diffusion limit and hence the ability to accurately predict the photon fluence in diffusive regimes.

The numerical techniques employed herein were derived and discretized such that the diffusion limit was maintained. To verify that we can accurately predict the photon fluence in highly diffusive media, we ran RTE and diffusion simulations of homogeneous 2% and 3% intralipid solutions. The isotropic scattering coefficients (μ_s') are 25.6 cm^{-1} and 38.4 cm^{-1} respectively for the 2% and 3% intralipid solutions and $\mu_{a,x} = 0.018$ cm^{-1} for both. The amplitude and phase predictions for both diffusion and RTE are shown in Figure 37 and demonstrate capability of the RTE solver to obtain accurate predictions in the diffusion limit.

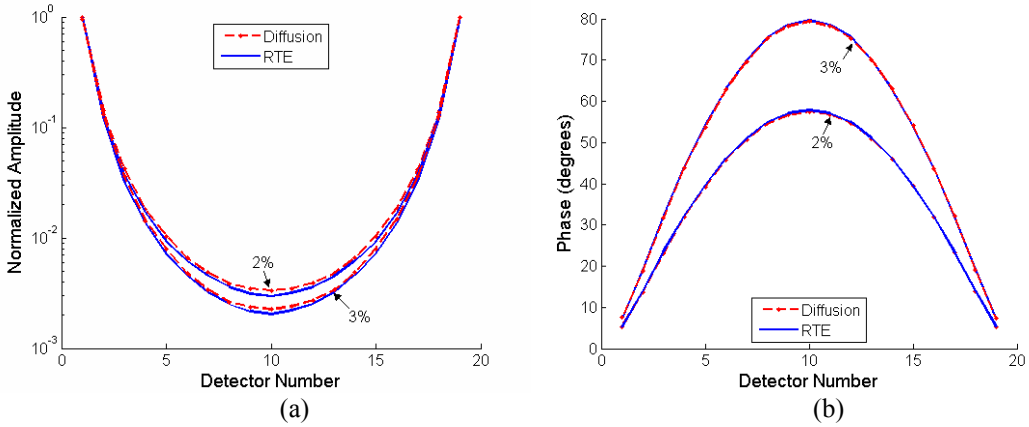

Figure 37: RTE and diffusion simulations of 2% and 3% intralipid solutions, where (a) is the amplitude and (b) is the phase.

The Transport Limit

One of the main advantages of the RTE equation over the diffusion equation is the ability to simulate the propagation of light through void-like volumes. To demonstrate the ability of the RTE solver to accurately simulate the photon fluence in a void, we simulated a cylindrical phantom (height is 4 inches and diameter is 1 inch) filled with water (μ_s' = 0.0 cm^{-1}, μ_a = 0.011 cm^{-1} as estimated from the spectrum of water at 785 nm). The source, modulated at 100 MHz, was again modeled as a point source with a numerical aperture of 0.39. For the RTE simulation, we used the analytic ray tracing techniques available as part of the FSDS method described in 0. The results obtained from both RTE and Monte Carlo are shown in Figure 38 for amplitude and phase. As can be seen, the predictions coincide, demonstrating the ability of the RTE solver to predict the fluence of photons in a void.

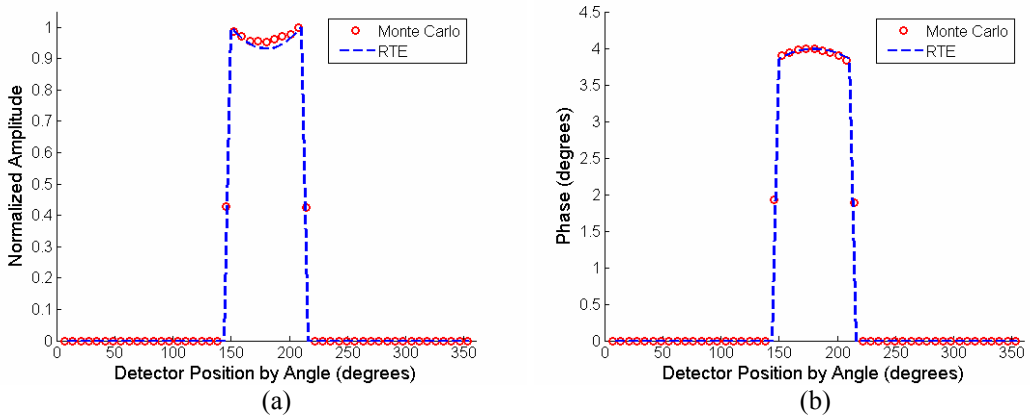

Figure 38: Plot of the (a) amplitude and (b) phase as predicted by the RTE solver and Monte Carlo for a phantom filled with water ($\mu_s' = 0.0$ cm^{-1} and $\mu_a = 0.011$ cm^{-1}).

Conclusions

In this section we validated the RTE solver against the diffusion and Monte Carlo methods. The RTE solver appropriately accounted for the incident frequency, fluorophore lifetime, and anisotropic factor and accurately predicted both amplitude and phase in the diffusion and transport limits. To further verify and quantify the accuracy of the RTE solver, a comparison of predictions to a series of experimental data obtained using the homodyne instrument is presented in the next section.

VI. EXPERIMENTAL VALIDATION OF THE RTE FORWARD SOLVER*

Introduction

The accurate modeling of photon propagation in tissue is an important step in optical tomography, where the internal optical properties of a tissue volume are reconstructed from experimental measurements taken at an external boundary. The region of interest in the target tissue generally has different or contrasting optical properties when compared to the surrounding tissues. Endogenous contrast occurs when the scattering and/or absorption properties of the target differ from the background and exogenous fluorescent contrast occurs when a fluorescent agent is introduced for preferential accumulation into the target tissue. In general, exogenous fluorescent agents result in greater contrast than absorption when time dependent measurements are used. Consequently fluorescent agents could provide enhanced tomographic delineation of target tissues.[85, 90]

In optical tomography, several classes of algorithms, ranging from filtered backprojection and algebraic reconstruction techniques (ART), to complex model based-iterative image reconstruction (MOBIIR), are typically used. Filtered backprojection is a simple image reconstruction algorithm that has been used in x-ray computed tomography, and is performed by attributing the attenuation of detected optical signals to the absorption coefficient along the geometric line connecting source

* Reprinted with permission from "Radiative transport in fluorescence-enhanced frequency domain photon migration" by Rasmussen *et al.*, 2006. *Medical Physics*, accepted for publication, 2006 by American Association of Physicists in Medicine.

and detector points.[49, 52] In ART, each measurement value is described by an equation which assigns a weight, as determined by a forward model, describing the probability of a photon crossing each pixel or voxel on its journey from source to detector; the resulting set of equations is then solved by direct or iterative techniques.[49, 91] MOBIIR interactively updates an assumed optical property map across the entire volume until measurements at the external boundary of the volume match those predicted by a model using the updated optical property map.

Historically, the diffusion equation, an approximation to the radiative transport equation, has been widely accepted as a means to describe the propagation of light through tissue volumes because of its ease of use and low computational cost. Its application has been documented in diverse tomographic applications involving absorption imaging to assess oxygenation status and blood flow [21, 92-94] and cancer detection from fluorescent contrast [95, 96] and absorption imaging. [94, 97, 98] However, the assumptions of the diffusion approximation require that the isotropic scattering coefficient ($\mu_s' = \mu_s(1-g)$) be much greater than the absorption coefficient and that the detectors be far away from the source (>10 mean free paths).[99-101]

In the past several years, great interest has been generated in the optical tomography of small animal volumes because of the potential imaging application for medical research and drug discovery. However, the small volumes (tens of milliliters) and the wide variety of optical properties resulting in diffusive transport, such as within the skin ($\mu_s' = 62\,cm^{-1}$, $\mu_a = 2.8\,cm^{-1}$, $g = 0.74$ at 488 nm), and in transport limited propagation, such as the highly absorptive liver ($\mu_s' = 5.8\,cm^{-1}$, $\mu_a = 5.7\,cm^{-1}$,

$g = 0.94$ at 800 nm)[46] make small animal optical tomography challenging. Because of the wide range of optical properties and the small volumes of interest, the diffusion approximation will likely not be valid for small animal imaging. In spite of these limitations, several researchers have, with some success, adapted the diffusion approximation for use in small volume tomography[22, 23, 59, 61, 64-66, 71, 73] due to its ability to qualitatively, if not quantitatively, predict the propagation of photons even if outside its fundamental assumptions. Others, including the present authors, have investigated the application of the radiation transport equation (RTE).[36-38, 40, 56-58, 60, 62, 63, 67-70] Unlike the diffusion approximation, the RTE can accurately predict the propagation of photons through highly absorptive and void-like tissues, and is not limited by practical separation distances between the source and detectors. Furthermore the directionality of incident light owing to fiber optic delivery and collection of light can be predicted. Hielscher *et al.* [40] demonstrated the increased accuracy of a certain RTE solver as compared to a diffusion solver for a variety of absorption to scattering ratios. Table 1 summarizes the literature results which employ diffusion or RTE for small animal tomography.

In this section we first present the governing RTE equations that describe the time-dependent propagation and attenuation of excitation and emission photons, as well as the decay kinetics associated with generation of fluorescence and then briefly describe their solution. Frequency-domain experimental data at excitation and emission wavelengths is acquired on a phantom, and the measured data is then

compared to RTE predictions of phase and amplitude, as well as with predictions from the diffusion approximation or Monte Carlo.

Materials and Methods

Forward Model

Governing Equations

The coupled fluorescent RTE equations in frequency space are written as:

$$\begin{aligned}
&\frac{i\omega}{c_x}\tilde{\phi}_x\left(\vec{r},\hat{\Omega},\omega\right)+\hat{\Omega}\cdot\nabla\tilde{\phi}_x\left(\vec{r},\hat{\Omega},\omega\right)+\Sigma_t^x\tilde{\phi}\left(\vec{r},\hat{\Omega},\omega\right)_x = \\
&\qquad S_x\left(\vec{r},\hat{\Omega},\omega\right)+\mu_s^x\int_{4\pi}p\left(\hat{\Omega}\rightarrow\hat{\Omega}'\right)\tilde{\phi}_x\left(\vec{r},\hat{\Omega},\omega\right)d\hat{\Omega}' \\
&\frac{i\omega}{c_m}\tilde{\phi}_m\left(\vec{r},\hat{\Omega},\omega\right)+\hat{\Omega}\cdot\nabla\tilde{\phi}_m\left(\vec{r},\hat{\Omega},\omega\right)+\Sigma_t^m\tilde{\phi}_m\left(\vec{r},\hat{\Omega},\omega\right)= \\
&\qquad \frac{\phi\mu_{a_{xf}}}{1+i\omega\tau}\phi_x+\mu_s^m\int_{4\pi}p\left(\hat{\Omega}\rightarrow\hat{\Omega}'\right)\tilde{\phi}_m\left(\vec{r},\hat{\Omega}',\omega\right)d\hat{\Omega}'
\end{aligned} \tag{72}$$

where the total cross section extinction at the excitation (x) and emission (m) wavelengths are given as:

$$\Sigma_t^x=\mu_{a,xf}\left(\vec{r}\right)+\mu_{a,x}\left(\vec{r}\right)+\mu_s^x\left(\vec{r}\right) \tag{73}$$

$$\Sigma_t^m=\mu_{a,m}\left(\vec{r}\right)+\mu_s^m\left(\vec{r}\right) \tag{74}$$

and $\phi_x=\int_{4\pi}\tilde{\phi}_x d\hat{\Omega}'$ is the angle integrated flux.

The term $\tilde{\phi}_i$ is the angular light flux (complex with amplitude and phase); ω is the frequency at which the incident excitation light is modulated; c is the speed of light in the medium; ϕ is the quantum efficiency of the fluorophore used; τ is its

lifetime; $\mu_{a,i}$ is the absorption coefficient of the medium; $\mu_{a,xf}$ is the absorption coefficient due to the absorption of excitation light by the fluorophore; S_x is the excitation source term; and μ_s^i is the scattering coefficient. The term $p\left(\hat{\Omega} \to \hat{\Omega}'\right)$ characterizes the angular distribution of light as it is scattered throughout the medium. In this application, the Henyey-Greenstein function shown is used:

$$p(\theta) = \frac{1}{4\pi} \frac{1-g^2}{\left(1+g^2-2g\cos\theta\right)^{3/2}} \tag{75}$$

where θ is the scattered angle (between $\hat{\Omega}$ and $\hat{\Omega}'$) and $g = \langle \cos\theta \rangle$ is the anisotropy parameter or the mean cosine of the scattering angles. In the simulated forward problems, the optical properties are known and the RTE equations are solved for $\tilde{\phi}_x$ and $\tilde{\phi}_m$.

To further validate the solutions provided by the RTE equations in diffusive media, simulations were also performed using RTE based Monte Carlo techniques [43, 83, 84] and the diffusion approximation.

Boundary Conditions

A vacuum boundary condition was used in the simulated forward problems. This boundary condition simulated no light to be reflected at the boundary and no photons to reenter the phantom. Experimentally, this corresponds to a black phantom wall which absorbs photons without back scatter.

In the studies presented herein, we modeled the fiber optic light source as an isotropic source, a unidirectional collimated source, or a source with a defined

numerical aperture (NA). As illustrated in Figure 39, isotropic sources launch light in all directions and the collimated source launches a unidirectional beam of light into the medium. The source with a defined NA is defined such that photons are launched into the medium based upon a user defined angular quadrature, permitting the half angle α, as shown in Figure 39, to be defined anywhere in the range of 0 to 180°. Consequently the numerical aperture of an optical fiber can be realistically modeled. In these studies, the numerical aperture of the optical fibers was 0.39, corresponding to an α of 17° in a medium with the refractive index of water.

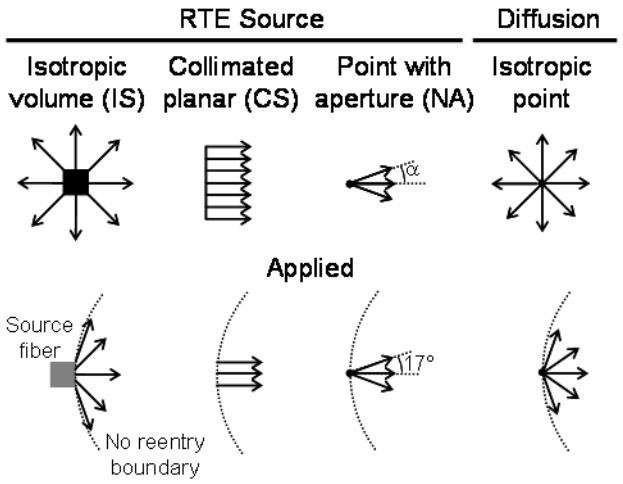

Figure 39: Illustration of the typical distribution of light emitted from an optical fiber and the source representations available in the RTE and diffusion solvers. The parameter α is the numerical aperture or half angle of the fiber and corresponds to 17° when the refractive index is 1.33 such as for water.

RTE Solution

The coupled RTE equations are solved within the general framework of the Attila transport software developed by Transpire, Inc. and previously described in detail by Wareing et al.[80] The solution was obtained using discrete-ordinate techniques as described in Section II.

To illustrate the robustness of the developed RTE solver, we comparatively evaluated step differencing (a simple and inefficient scheme previously used in optical tomography) and linear discontinuous (LD) spatial differencing (used in the Attila™ package) on a 4x4x1.3 cm^3 phantom with the source and detector planes on opposing sides as illustrated in Figure 40. An isotropic excitation source was placed at the center of the front 4x4 cm^2 source plane, with a 2.7x2.7 cm^2 array of 400 detectors on the opposing 4x4 cm^2 detector plane. The optical properties employed were marginally diffusive with a $\mu_s = 30.0\ cm^{-1}$, $\mu_a = 0.4\ cm^{-1}$, and $g = 0.8$. For both step and LD differencing, S_6 angular quadrature order (48 discrete angles) and transport corrected P_2 scattering were applied. We performed an initial mesh sensitivity study with a 0.2 cm maximum element edge length and then refined the mesh incrementally until a maximum element edge length of 0.0375 cm was achieved. The results are provided and discussed below.

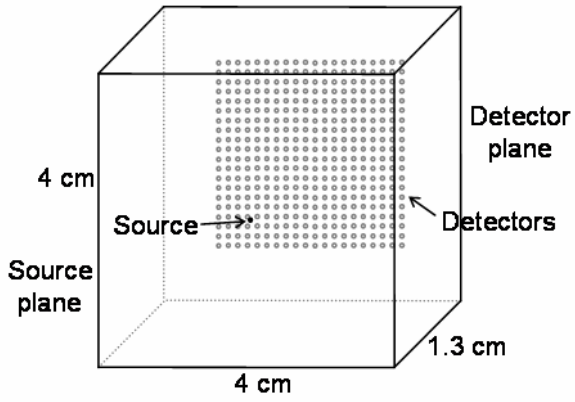

Figure 40: Illustration of phantom used in the analysis of mesh size and the step and linear discontinuous differencing schemes. The background optical properties were μ_s=30 cm^{-1}, μ_a=0.4 cm^{-1}, and g=0.8.

Experimental Procedures

Phantoms

RTE predictions of $\tilde{\phi}_x$ and $\tilde{\phi}_m$ were compared with experimental measurements conducted on a black cylindrical phantom with a 2.5 cm diameter and 10 cm height (see Figure 41a). Twenty multimodal fibers (model FT-1.0-EMT, Thorlabs Inc., Newton, NJ) with a core diameter of 1 mm and a numerical aperture of 0.39 were positioned eighteen degrees apart 5 cm from the phantom top. One fiber delivered excitation light and the remaining nineteen, numbered sequentially, collected propagated light. The phantom was filled with 1.0%, 0.5%, or 0.2% intralipid solutions made by diluting 20% Liposyn (Abbott Laboratories, Abbott Park, Illinois) with deionized water and added India ink, and desired targets were introduced as illustrated in Figure 41b and 42c.

Fluorescent solutions were made by dissolving indocyanine green (ICG) (Sigma-Aldrich, St. Louis, MO) in ultra-filtered, deionized water and adding sufficient quantities of the ICG stock solution to a portion of each intralipid solution to obtain 1 μM ICG concentrations. Optical properties of the solutions were measured using the method described by Sun *et al.* [77] at 785 and 830 nm. The absorption of the fluorophore ($\mu_{a,xf}$) was assumed to be the difference in $\mu_{a,x}$ measured with and without ICG. Table 2 details the various optical properties that were used in these studies including the mean isotropic scattering path length ($l_s=1/(\mu_s')$) which serves as an indicator of the distance ($10l_s$) a photon must travel prior to being considered diffuse. We assumed the refractive index of intralipid to be that of water and the anisotropy to be 0.64. From the literature, we assumed the lifetime of the ICG as 0.56 ns and the quantum efficiency as 0.016.[102] Targets were constructed from 0.3, 0.5, or 1 cm diameter NMR tubes filled with a intralipid solution. Figure 41 details the location of the targets employed in these studies. The specific experimental phantoms presented herein, and detailed in Table 3, were designed to test the RTE forward model predictions in the diffusion and transport limits as determined by the optical properties of the phantoms.

Table 2: Optical properties of solutions used in these studies as measured using single pixel techniques.[77]

Material	μ_{ax} (cm^{-1})	μ_{afx} (cm^{-1})	μ_{sx}' (cm^{-1})	μ_{am} (cm^{-1})	μ_{afm} (cm^{-1})	μ_{sm}' (cm^{-1})	g	$l_{s,x}$ (cm)
1% intralipid	0.025	0	10.33	0.022	0	9.56	0.64	0.097
1% intralipid with 1μM ICG	0.025	0.15	14.08	0.022	0.14	14.68	0.64	0.071
0.5% intralipid	0.027	0	4.81	0.026	0	5.23	0.64	0.21
0.5% intralipid with 1μM ICG	0.027	0.17	6.84	0.026	0.20	5.70	0.64	0.15
0.2% intralipid	0.033	0	1.83	0.031	0	2.08	0.64	0.55
0.2% intralipid with India ink	0.91	0	3.26	0.71	0	3.66	0.64	0.31
Water*	0.011	0	0	0.012	0	0	1	-
Fiber/Air+	0	0	0	0	0	0	1	-

*estimated from water spectrum; +assumed

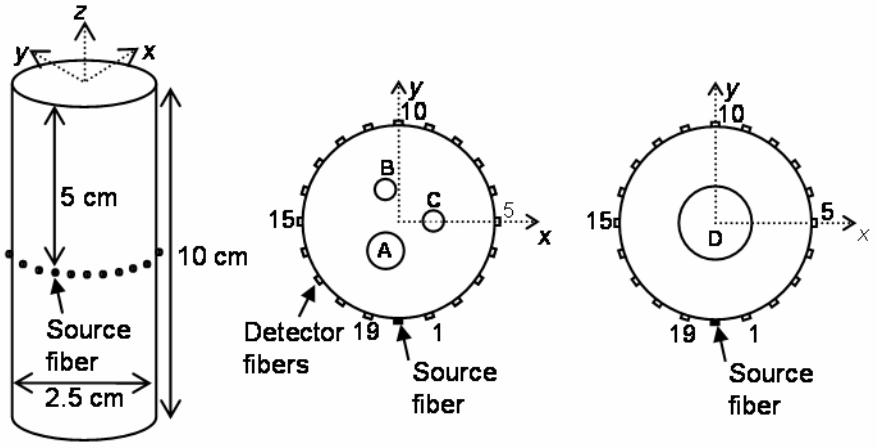

(a) (b) (c)

Figure 41: (a) Schematic of phantom used in studies, (b) heterogeneities locations A (-1.83, -4.11)mm, B (-1.83, 4.11)mm, and C (4.5, 0)mm, (c) heterogeneity location D (0, 0)mm.

Table 3: Table summarizing the phantom setup of experiments performed. See Table 2 for optical properties of solutions, and Figure 41 for location of target positions A, B, C, and D.

Background Media	Experiment Setup
Approaching Diffusion Limit	
1% intralipid	a) Homogeneous
	b) 1 μM ICG at A
	c) Homogeneous 1 μM ICG
0.5% intralipid	a) Homogeneous
	b) 1 μM ICG at A
	c) Homogeneous 1 μM ICG
Transport Limited	
1.0% intralipid	Void at A
0.5% intralipid	Void at A
0.2% intralipid	1 μM ICG at A, absorber at B, void at C
Water	a) Homogeneous
	b) 1.0% intralipid at D

Instrumentation

As illustrated in Figure 19, frequency domain data was obtained using a system in which a 785 nm laser diode (Sanyo DL7140-201S, Thorlabs Inc., Newton, NJ) was modulated at 100 MHz with a Marconi 2022D signal generator to deliver intensity modulated excitation light to the phantom surface via a fiber optic. The 19 collecting fibers carried the propagated light (excitation and emission) to a bundle faceplate where a lens (50 AF Nikkor) focused the emitted light onto the photocathode of the image intensifier (ITT Night Vision, Roanoke, VA). For excitation light detection, a 5 OD neutral density filter was inserted in front of the lens to attenuate the excitation signal. A 830 nm bandpass filter (Andover Corp., Salem, NH) and a 785 nm

SuperNotch-Plus™ holographic filter (Kaiser Optical Systems Inc., Ann Arbor, MI) were used to reject excitation light during emission measurements. The photocathode of the intensifier was modulated at 100 MHz by an amplified (ENI 304L amplifier) signal from a PTS 310 signal generator (Programmed Test Sources, Littleton, MA) which was phase locked with the Marconi signal generator. The image intensifier amplified the detected signals for delivery to a CCD camera (Princeton Instruments, Trenton, NJ). The CCD camera, which was optically coupled to the phosphor screen of the image intensifier, has a resolution of 1024x1024 pixels which was binned four times to obtain an image with 256x256 pixels. The images were acquired and stored on a personal computer.

Measurements

Frequency domain data were acquired by employing the homodyne technique described previously.[74, 75] At each phase delay, three time-integrated images of the fiber optic bundle were obtained at exposure times ranging from 100 ms for excitation measurements and up to 1,500 ms for emission measurements. After acquisition, the images for each phase delay were averaged and a fast Fourier transform (FFT) of the intensity at each detector fiber as a function of phase delay was performed to obtain the amplitude and phase of the collected signals. To account for unknown instrument responses, including attenuation of optical filters and fibers, the resulting amplitude data were normalized by the maximum amplitude, while a constant phase shift was added to the measured phase. The constant phase lag was introduced by the instrumentation with the major component coming from the initial phase difference

between the Marconi and the PTS signal generators used to drive the photocathode and the laser diode. Error bars show the standard deviation of at least three experimental data sets.

Simulations

For each experimental configuration, three RTE solutions were obtained by modeling the source fiber as an isotropic volume source (IS), a unidirectional collimated source (CS), and a source with a numerical aperture (NA). All RTE simulations, except the water phantom, were done with the S_6 Chebyschev-Legdendre angular quadrature set with transport corrected P_3 scattering on a mesh with 124,966 elements and 24,413 nodes. A typical processing run took about 45 minutes on a workstation with two 2.6 GHz dual core Opteron processors and 16 GB of memory. Diffusion simulations were performed on the same mesh using an isotropic point source with a typical run time of approximately 30 seconds on a workstation with two Xeon 3.0 GHz processors with 3 GB of memory. The simulation of the water phantom was done on a mesh with 110,696 cells and 19,716 nodes using FSDS and integral transport theory to calculate the incident light and well as the detected light. After simulation, the amplitude was normalized by the maximum amplitude.

Data Analysis

To quantitatively compare the forward model predictions with experimental measurements, the average simulation errors with respect to the experimental measurements were calculated using the following equation:

$$Error = \frac{100}{N}\sqrt{\sum_{i}^{N}\frac{(m_i - c_i)^2}{m_i^2}} \quad \textbf{(76)}$$

where N is the number of collecting fibers, m_i is the measured experimental value and c_i is the simulated value respectively for collecting fiber i.

Results and Discussion

Effect of Edge Length and Spatial Differencing Method

Table 4 tabulates the average RMS error of the LD and step differencing schemes with respect to the LD solution with the smallest element edge length. As shown, the average RMS error of the LD differencing solution with the largest element edge length is less than 5.0%, while that of step differencing is 257%. Even at the smallest element edge length, the average RMS error of step differencing is 122% of the LD differencing solution. These results are significant, considering that the experimental conditions are only moderately diffusive and as the scattering coefficient increases, the numerical inaccuracies of step differencing will be magnified. They further illustrate the robust nature of the linear discontinuous finite differencing scheme employed in the RTE forward model and the ability to accurately predict the photon flux across relatively large spatial elements, ultimately decreasing the computational burden sustained by the solver.

Table 4: Mesh sensitivity studies comparing STEP and linear discontinuous (LD) spatial differencing schemes.

		RMS Error from Reference Solution	
Element Edge Length (cm)	Mesh Element Count	Linear Discontinuous (LD) Differencing	STEP Differencing
0.2	7,500	4.90%	257%
0.15	17,000	4.00%	232%
0.1	42,000	2.50%	186%
0.075	98,000	1.20%	162%
0.05	270,000	0.90%	139%
0.0375	640,000	Reference Solution	122%

Approaching the Diffusion Limit

Figures 42a and 42b present the amplitude and phase results of the experimental data and the RTE and diffusion predictions of the homogeneous 1.0% intralipid phantom; Figures 42c and 42d present the corresponding results from the phantom with a 5 mm diameter target containing 1.0 μM ICG; and Figures 42e and 42f present those results obtained from the phantom with 1.0 μM ICG throughout. The mean free scattering path of 1.0% intralipid is 0.097 which is sufficient for the collected photons to be diffusive at all but the closest detectors. As such, it is not surprising that the amplitude and phase predictions from diffusion and the RTE isotropic volume (IS), numerical aperture (NA), and collimated (CS) source representations coincide making it is difficult to distinguish them in the figure. The average error for the RTE source representations ranges from 4.1% to 8.4% in amplitude and from 0.7% to 6.7% in phase, while the average error of the diffusion prediction ranges from 4.1% to 7.8% in amplitude and 1.0% to 6.8% in phase. The

good agreement between the RTE and diffusion predictions and the experimental data corroborate the accuracy of the prediction of the diffusion limit using the RTE solver.

Figures 43a and 43b present the amplitude and phase results of the experimental data and the RTE and diffusion predictions of the homogeneous 0.5% intralipid phantom; Figures 43c and 43d present the corresponding results from the phantom with a 5 mm diameter target containing 1.0 μM ICG; and Figures 43e and 43f present those results obtained from the phantom with homogeneous 1.0 μM ICG throughout. As can be seen, the excitation amplitude predictions of the RTE CS and NA source representations do not coincide with the diffusion and RTE IS predictions. This may be due to the relatively high mean free scattering path of 0.5% intralipid which requires the photons travel ~2 cm before they are considered diffuse. Because of the small source and collector fiber separations, the forward peakedness of the incident light due to the numerical aperture of the source fiber is still present when the photons reach the collection fibers. When isotropic sources were employed, the forward peaked nature of the source was lost, and the artificial increase in detected signal near the source resulted in a greater relative amplitude attenuation across the phantom. This effect was not present in the emission amplitude due to the isotropic nature of fluorescence emission. The range (2.1% to 6.5%) of average error (Table 5) of the RTE IS and diffusion amplitude predictions were approximately twice the average error of the amplitude predictions of the RTE CS and NA. The phase predictions of the RTE source representations coincide at all detectors except those nearest to the source. The larger phase predicted by the RTE CS may be a result of the

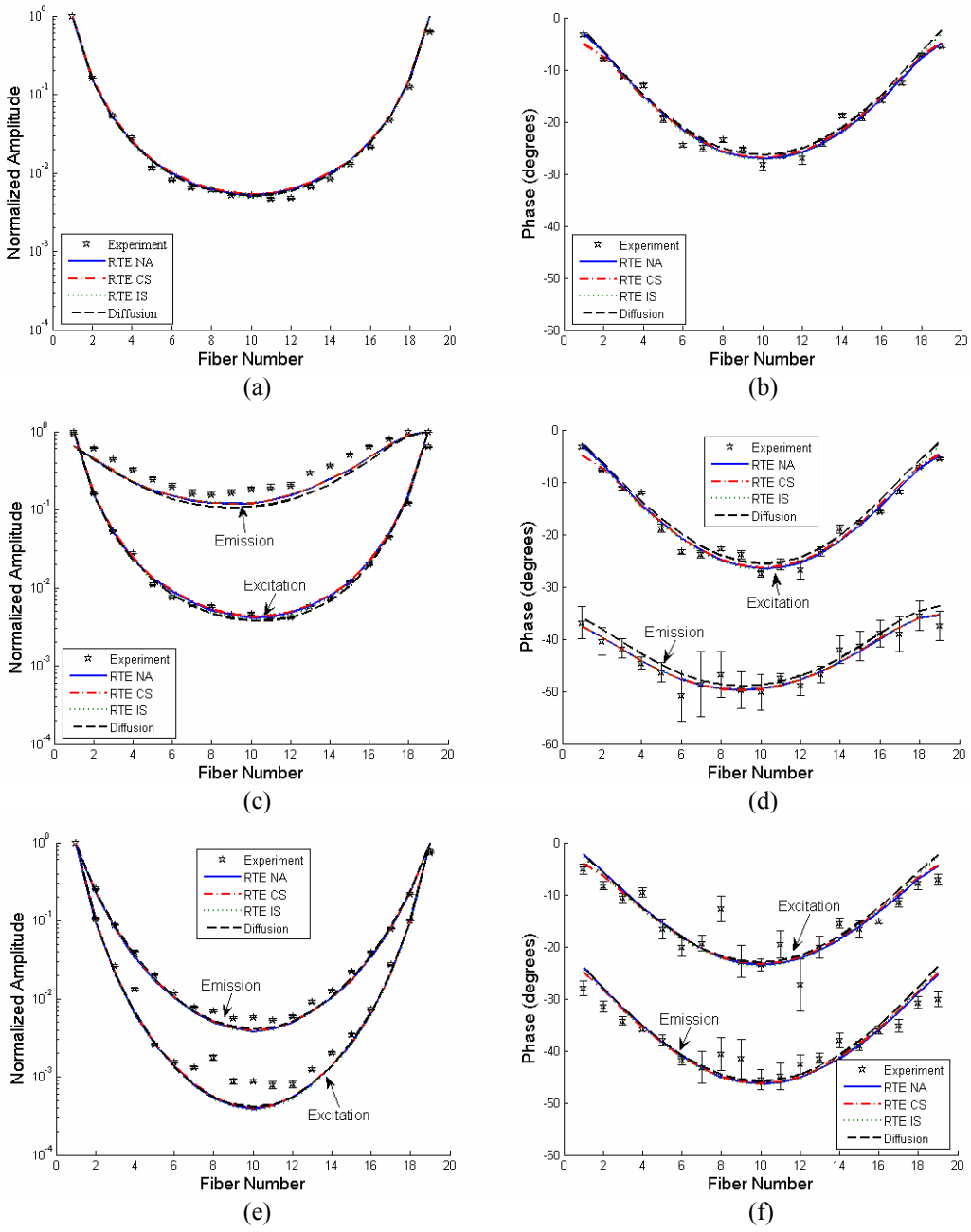

Figure 42: Comparison of RTE and diffusion predictions and experiment data at 1.0% intralipid. (a) and (b) are the amplitude and phase data for homogenous 1.0% intralipid. (c) and (d) are the amplitude and phase data for 1.0% intralipid with a 5 mm diameter target containing a 1 μM ICG solution. (e) and (f) are the amplitude and phase data for a homogeneous 1 μM ICG solution in 1.0% intralipid. The RTE NA, RTE CS, and RTE IS curves represent the solution of the radiative transport equation when a point source with a numerical aperture, a collimated planar source, or an isotropic volume source excitation source respectively was used as the excitation source.

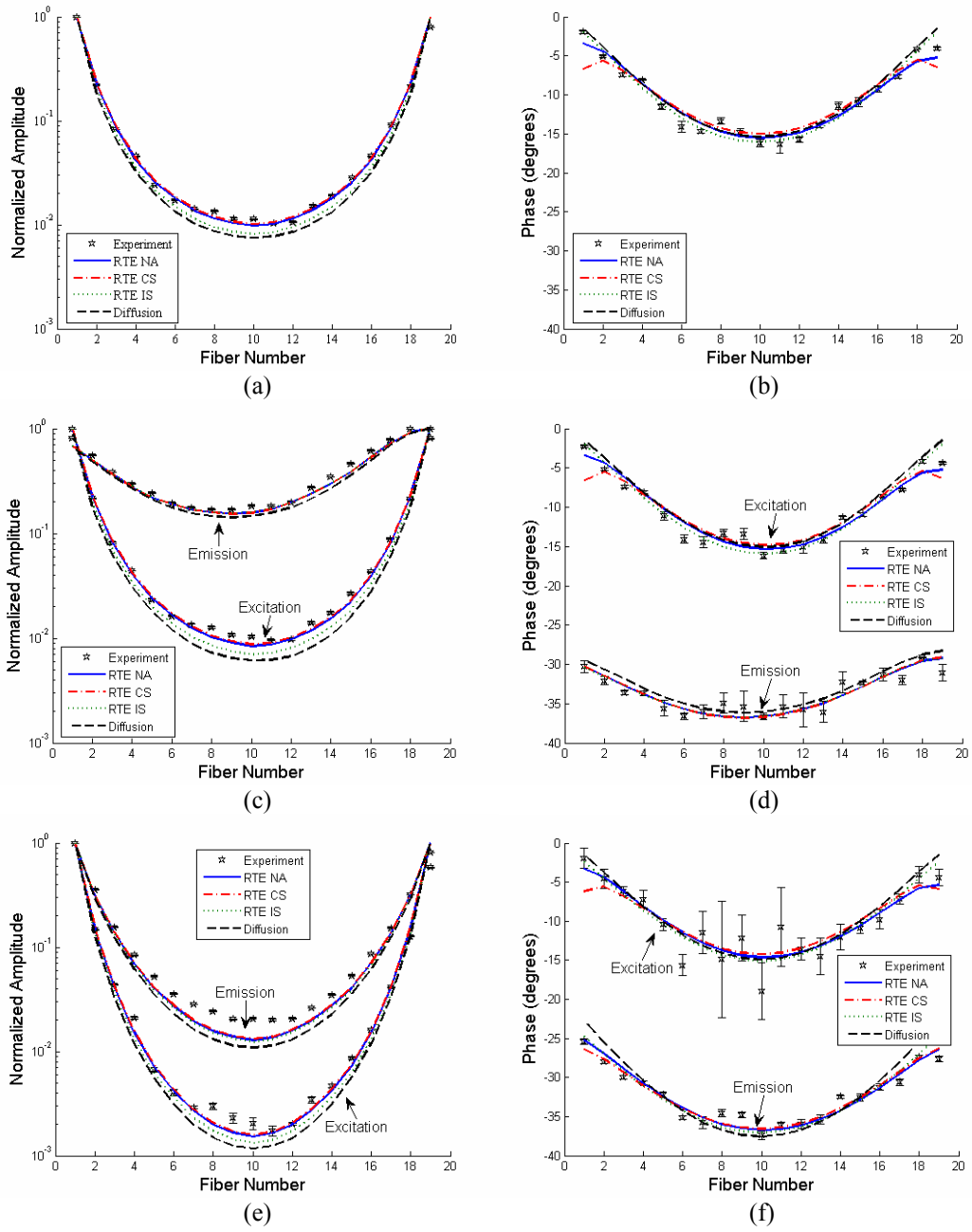

Figure 43: Comparison of RTE and diffusion predictions and experiment data at 0.5% intralipid. (a) and (b) are the amplitude and phase data for homogenous 0.5% intralipid. (c) and (d) are the amplitude and phase data for 0.5% intralipid with a 5 mm diameter target containing a 1 μM ICG solution. (e) and (f) are the amplitude and phase data for a homogeneous 1 μM ICG solution in 0.5% intralipid. The RTE NA, RTE CS, and RTE IS curves represent the solution of the radiative transport equation when a point source with a numerical aperture, a collimated planar source, or an isotropic volume source excitation source respectively was used as the excitation source.

Table 5: Average percent errors between the predicted and experimental amplitude.

			RTE						**Diffusion**	
			Collimated source		Numerical Aperture		Isotropic source			
	Phantom	Target(s)	Excitation	Emission	Excitation	Emission	Excitation	Emission	Excitation	Emission
Approaching Diffusion Limit	1.0% intralipid	Homogeneous	5.1%	--	4.8%	--	4.1%	--	4.3%	--
		ICG target	4.2%	6.0%	4.1%	6.1%	3.9%	6.0%	4.1%	7.3%
		ICG	7.7%	4.3%	8.0%	4.6%	8.4%	4.6%	7.8%	4.0%
	0.5% intralipid	Homogeneous	2.1%	--	2.2%	--	4.6%	--	6.1%	--
		ICG target	2.4%	2.2%	2.8%	2.2%	5.3%	2.1%	7.4%	3.4%
		ICG	5.0%	5.1%	5.2%	5.4%	6.5%	6.0%	8.0%	7.6%
Transport Limited	1.0% intralipid	Void	6.8%	--	6.4%	--	5.3%	--	12.2%	--
	0.5% intralipid	Void	3.0%	--	2.6%	--	3.7%	--	14.5%	--
	0.2% intralipid	ICG target, absorber, and void	7.1%	5.5%	10.2%	5.3%	10.9%	5.9%	19.8%	15.5%
									Monte Carlo	
									8.7%	5.9%
	Water	1.0% intralipid heterogeneity	--	--	14.9%	7.9%	--	--	13.9%	7.8%

Table 6: Average percent errors between the predicted and experimental phase

			RTE						Diffusion	
			Collimated source		Numerical Aperture		Isotropic source			
	Phantom	Target	Excitation	Emission	Excitation	Emission	Excitation	Emission	Excitation	Emission
Approaching Diffusion Limit	1.0% intralipid	Homogeneous	3.0%	--	2.5%	--	3.5%	--	3.7%	--
		ICG target	3.1%	0.7%	2.7%	0.7%	3.7%	0.7%	4.1%	1.0%
		ICG	5.6%	1.7%	6.4%	1.8%	6.7%	1.9%	6.8%	1.9%
	0.5% intralipid	Homogeneous	13.1%	--	4.8%	--	3.2%	--	4.1%	--
		ICG target	10.6%	0.7%	3.8%	0.7%	3.5%	0.7%	4.8%	0.9%
		ICG	12.1%	0.6%	5.3%	0.7%	4.4%	0.9%	5.0%	1.5%
Transport Limited	1.0% intralipid	Void	4.0%	--	2.3%	--	3.2%	--	5.7%	--
	0.5% intralipid	Void	15.4%	--	5.8%	--	3.3%	--	6.1%	--
	0.2% intralipid	ICG target, absorber, and void	19.9%	2.7%	20.6%	2.7%	14.9%	2.9%	12.4%	3.6%
									Monte Carlo	
									26.2%	3.5%
	Water	1.0% intralipid heterogeneity	--	--	7.7%	2.1%	--	--	8.8%	1.8%

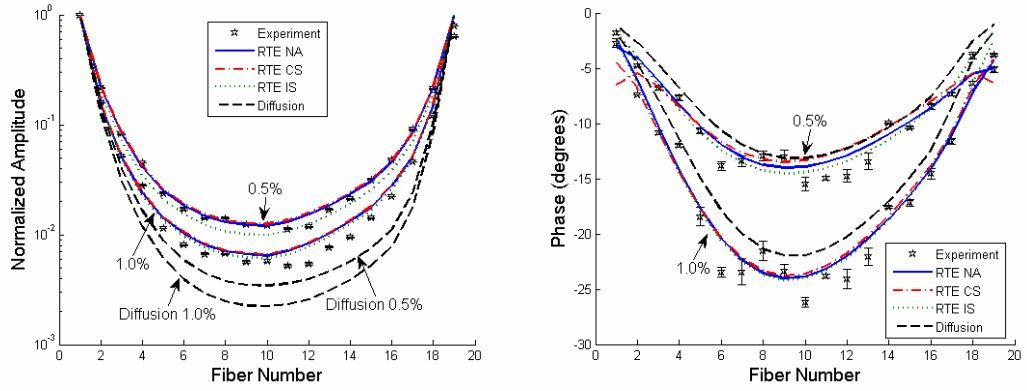

(a) (b)

Figure 44: Comparison of experiment and RTE data for 0.5% and 1.0% intralipid solutions containing a 5 mm diameter void at position A. (a) is the amplitude, and (b) is the phase. The RTE NA, RTE CS, and RTE IS curves represent the solution of the radiative transport equation when a point source with a numerical aperture, a collimated planar source, or an isotropic volume source excitation source respectively was used as the excitation source.

forward peakedness of the incident light. The average phase errors (Table 6) for all simulations range from 0.6% to 12.1% with the largest errors coming from the RTE CS representation.

Transport Limit

Figure 44 presents the amplitude and phase of a 1.0% and a 0.5% intralipid phantom with a 5 mm diameter void. As shown, the RTE CS and NA simulations coincide while the RTE IS predictions are more attenuated. The 1.0% intralipid phantom has an average error in the 5-7% range for amplitude while the 0.5% intralipid phantom has approximately 3-4% error for all RTE amplitude predictions as shown in Table 5. The average phase error (Table 6) for the RTE predictions ranges from 2-6% with the exception of the RTE CS prediction which has an error of 15.4%

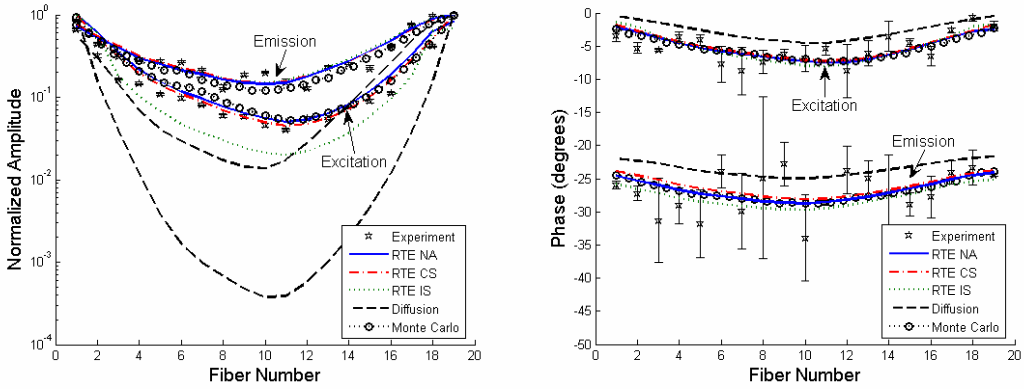

Figure 45: Comparison of RTE and diffusion prediction and experimental data for a 0.2% intralipid phantom containing a 5mm 1 μM ICG target. a 3 mm absorber, and a 3 mm void. (a) shows the amplitude, and (b) shows the phase.

due to the larger phase near the source. The results for diffusion are also shown in Figure 44 to illustrate the ability of diffusion to qualitatively predict the propagation of light through a non-diffuse medium. However, while diffusion correctly predicts the qualitative light propagation, its average amplitude error is 12-15% which is two to three times higher than the corresponding average RTE error.

Figure 45 presents the amplitude and phase for a 0.2% intralipid phantom containing a 5 mm diameter fluorescent target (0.5% intralipid with 1.0 μM ICG), a 3 mm diameter absorptive target (0.2% intralipid solution with India ink), and a 3 mm diameter void. The RTE CS and NA excitation amplitudes nearly coincided with average errors of 7.1% and 10.2% respectively, while the RTE IS predicted more attenuated excitation amplitude with an average error of 10.9%. This higher relative attenuation was again due the larger mean free scattering path (0.546 cm) and the isotropic nature of the source representation The emission amplitude for all three RTE

source representations coincided (average error of ~5.6%). The average errors of the RTE excitation phase predictions nearly coincide with an average errors ranging from 14.7% to 20.6%. However, the average emission phase error was ~2.7% for the RTE predictions. The diffusion predictions provided a poor match with errors as high as 19.8% for the excitation amplitude. Monte Carlo predictions using a point source with a numerical aperture is also shown in Figure 45, and its amplitude and phase predictions coincide with the RTE predictions. The large error bars on the experimental data are due to the small phase change of the propagated photons relative to the instrumentation noise in the phase measurement.

Figure 46 presents the amplitude and phase results of the experimental data and RTE NA prediction of a water filled phantom with a 1 cm diameter heterogeneity of 1.0% intralipid solution with 1.0 μM ICG. This phantom was specifically designed to test the ability of the RTE solver to correctly model the propagation of photons through void-like spaces prior to scattering. This latter ability is crucial to the implementation of the RTE forward model in practical, non-contact small animal tomography instrumentation and algorithms under implementation in our laboratory. The RTE NA prediction was obtained using the FSDS method and integral transport theory to model the numerical aperture of the detectors. Monte Carlo predictions are also shown and coincided with the RTE NA prediction except for a bump at the detector opposite the source indicating a higher predicted number of ballistic photons. The RTE NA prediction matched the experimental excitation and emission data with respective average errors of 14.9% and 7.9% in amplitude (Table 5) and 7.7% and

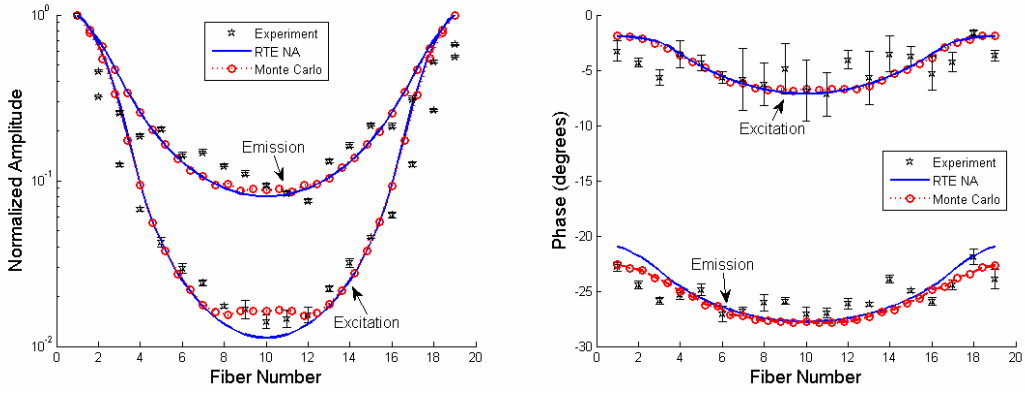

Figure 46: Comparison of RTE prediction utilizing a source with a numerical aperture and experimental data for a phantom of water with a 1 cm diameter heterogeneity of 1% intralipid with 1 μM ICG. (a) and (b) are the amplitude and phase respectively.

2.1% in phase (Table 6) while the Monte Carlos had similar average errors of 13.9% and 7.8% in amplitude and 8.1% and 1.8% in phase.

As demonstrated in the figures, the RTE solver is capable of predicting the time dependent excitation and emission photon flux in diffusive and transport limited phantoms with average errors typically less than 10% for amplitude and phase. Of particular note is the demonstrated need to accurately model the excitation source in the transport regime to prevent the apparent artificial diffusion of excitation photons. To our knowledge, this is the first fluorescence-enhanced, frequency-domain RTE based forward model to be developed and experimentally validated.

Summary and Conclusions

This work demonstrated the validity of a fluorescence-enhanced, time-dependent radiative transport based solver for modeling photon propagation. The coupled RTE equations were solved via a discrete ordinates method using the robust,

linear-discontinuous spatial differencing scheme. Source iteration with DSA provided both accurate and efficient amplitude and phase predictions for a variety of diffusive and transport limited phantoms using isotropic and unidirectional collimated sources as well as sources with a defined numerical aperture. Experimental data was obtained using a frequency-domain ICCD camera system from small phantoms (49 ml) with scattering properties ranging from 0 to 14.68 cm^{-1} and fluorescent targets containing 1 μM ICG. Comparison of experiment and simulated data has shown that the RTE based forward model can accurately predict time-dependent propagation of both excitation and emission light in both the diffusion and transport limits. Future work will involve the implementation of boundary conditions to allow realistic modeling of reflection and refraction, as well as optimization of the code to further reduce computation time. Based on the studies presented herein, this RTE solver may prove to be a vital component of a robust tomographic algorithm capable of obtaining quantitatively correct reconstructions of fluorescent regions within small animals, especially when using a non-contact fiber optic gantry positioned around the animal.

This work was supported by in part by the National Institutes of Health grants R41 CA 115028 (T. Wareing) and R01 EB003132 (E.M. Sevick-Muraca).

VII. OPTICAL TOMOGRAPHY RESULTS

The main objective of developing the fluorescence-enhanced, frequency-domain RTE solver was to implement it into a reconstruction algorithm suitable for small animal tomography. While the development of this reconstruction algorithm itself is not part of this dissertation, in this section we present the basis for the reconstruction algorithms, developed in the Division of Molecular Imaging, capable of using the RTE solver to reconstruct fluorescent targets from simulated and experimental data. We also demonstrate the reconstruction of synthetic mouse data produced using the RTE solver and the reconstruction of two sets of experimental data.

The Reconstruction Algorithms

The reconstruction algorithms are based on the coupled radiative transport equations which can be expressed in operator notation as:

$$\begin{aligned} H_x\tilde{\phi}_x &= S_x \\ H_m\tilde{\phi}_m &= B_{x\to m}\phi_x \end{aligned} \qquad \textbf{(77)}$$

where the subscripts x and m represent the excitation and emission wavelengths respectively; H_i is the radiative transport operator; $\tilde{\phi}_i$ is the complex angular fluence; S_x is the excitation source; ϕ_i is the complex scalar fluence ($\phi_i = \int \tilde{\phi}_i(\Omega)d\Omega$); and $B_{x\to m}\phi_x$ is the fluorescence source term. The algorithm is written in such a way that the diffusion approximation can be easily substituted in. This is done by replacing the

transport operator and complex angular fluence terms with the diffusion operator and complex scalar fluence terms respectively.

Two types of inverse algorithms were used to reconstruct the measured and synthetic data presented in this section. The simplest method uses the Born approximation to reduce the inverse problem to a set on linear equations which can be expressed as:

$$\begin{aligned} \phi_m - \phi_m^0 &= J \bullet \left(\mu_{a,xf} - \mu_{a,xf}^0 \right) \\ J &= \left\langle \left(H_m^* \right)^{-1} D, \frac{\partial B_{x \to m}}{\partial \mu_{a,xf}} \phi_x^0 \right\rangle \end{aligned} \qquad \textbf{(78)}$$

where ϕ_m is measured experimentally; ϕ_m^0 is the forward prediction based on an assumed map of fluorescence absorption ($\mu_{a,xf}^0$); J is the Jacobian matrix; H_m^* is the adjoint transport operator; D is the Dirac matrix and contains zeros everywhere except for a unity column corresponding to the detector location; and ϕ_x^0 is the excitation scalar flux predicted by the forward solver.[103] The orders of magnitudes of ϕ_m^0 and ϕ_m are typically different and the measured values must be scaled of referenced such that both the predicted and measured fluence are of the same order of magnitude. Scaling is accomplished by multiplying the measured fluence by some constant. Referencing is can be done by comparing the fluence to a reference point in the system, or by using the ration of the emission and excitation fluence. Of all the variables in equation (78) only $\mu_{a,xf}$ is unknown, and the set of linear equations can be solved using algebraic reconstruction techniques or by iteratively updating the fluorescence optical map until

the residual distance between the measured fluence and the predicted fluence is below a pre-specified tolerance.

Alternatively, the tomographic reconstruction algorithm was posed as an optimization problem wherein an error function, representing the mismatch between experimental measurements and the predictions of a photon transport model (RTE or diffusion based), is minimized. The error function can be written as:

$$E\left(\mu_{a,xf}\right)=\frac{1}{2}\sum_{k=1}^{K}\sum_{n=1}^{N}\left(\frac{\phi_{m,kn}^{0}-\sigma\phi_{m,kn}}{\sigma\phi_{m,kn}}\right)\left(\frac{\phi_{m,kn}^{0}-\sigma\phi_{m,kn}}{\sigma\phi_{m,kn}}\right)^{*} \quad \textbf{(79)}$$

where E is the error; K is the total number of sources; N is the total number of detectors, and σ is a scale factor used to adjust the order of magnitude of the measured fluence. This local optimization scheme requires either the computation of the gradient of an error function or a Jacobian sensitivity matrix. The gradient of the error function is the first derivative of the error function with respect to the unknown optical properties while the Jacobian matrix represents the sensitivity of the boundary fluorescence measurements to the unknown fluorescence absorption map. The information from the gradient or Jacobian is used to determine the updated optical map by:

$$\mu_{a,xf}^{i+1}=\mu_{a,xf}^{i}+\alpha^{i}d^{i} \quad \textbf{(80)}$$

where i indicates the iteration level, α is the step size chosen by a line search strategy, and d is the update direction. The update direction can be determined using a variety of ways including the conjugate gradient, Newton, Gauss-Newton, or Broyden-

Fletcher-Goldfarb-Shanno (BFGS) methods. The gradient and the Jacobian matrix are typically determined using adjoint differentiation.

For more detailed information on the derivation and application of these reconstruction algorithms, see Joshi.[103]

Synthetic Data Reconstructions

To test the feasibility of these reconstruction algorithms to for small animal tomography, we generated several simulated or synthetic data sets. To generate the most realistic synthetic data possible we constructed a virtual mouse based on the digital mouse phantom developed by Segars, *et al*.[104] Using CAD software (SolidWorks®) and the non-uniform rational B-spline (NURBS) data acquired from Dr. Segars we constructed a mouse phantom containing most of the major organs in a mouse including the heart, lungs, liver, stomach, spleen, kidneys, intestines, and bladder, as well as the body of the mouse as shown in Figure 47.

The virtual mouse was placed inside a cylinder which represented the imaging tube of the optical instrumentation. The cylinder and mouse were then meshed as shown in Figure 48 using the mesh generation utility included in the Attila® framework. Rings of alternating point sources (20) and detectors (20) were placed every 5 mm along the cylinder from the head to the tail. Each organ was assigned optical properties of corresponding organs as found in the literature and detailed in Table 7.[46] Also shown in Table 7 is the ratio of the isotropic scattering and absorption coefficients. This ratio serves as a measure of the diffusive nature of the tissue; a ratio of 10 satisfies the assumption that scattering dominates absorption made in the

derivation of the diffusion approximation. The body of the mouse was assigned the optical properties of muscle, and the cylinder was filled with water to maintain a void as would be present in a non-contact instrument. Because Snell's law is not yet implemented in the RTE solver, the index of refraction for all the tissues was assumed to be 1.33 thus avoiding an index of refraction mismatch at the tissue/water interface. We assumed that the fluorescence optical properties were the same as the excitation properties.

We considered the reconstruction of two sets of synthetic mouse data. In the first case, we set the fluorescent absorption coefficient ($\mu_{a,xf}$) to zero everywhere except for in the bladder where the fluorescence absorption was assumed to be equivalent to that of 10 nM ICG. The RTE solver was used to predict the excitation and fluorescent fluence for each excitation point source on the five rings nearest the bladder region. The remaining source and detector rings were neglected due to the

Table 7: The optical properties used in the virtual mouse phantom. When the ratio is ≥ 10 the tissue is considered diffusive. The refractive index of all tissues was assumed to be 1.33.

Organ/ Material	Absorption μ_a	Scattering μ_s	Anisotropy g	Ratio $\mu_s(1-g)/\mu_a$
Lungs	8.4	35.9	0.95	0.2137
Heart	0.35	167	0.98	8.114
Stomach	1.2	200	0.90	16.67
Intestine	1.2	200	0.90	16.67
Kidneys	0.01	73.3	0.85	1100
Spleen	2.8	13	0.78	1.024
Bladder	1.25	50.8	0.95	2.03
Liver	6.5	143.7	0.95	1.11
Body (muscle)	1	40	0.97	1.2
Water	0.011	0	1.00	0

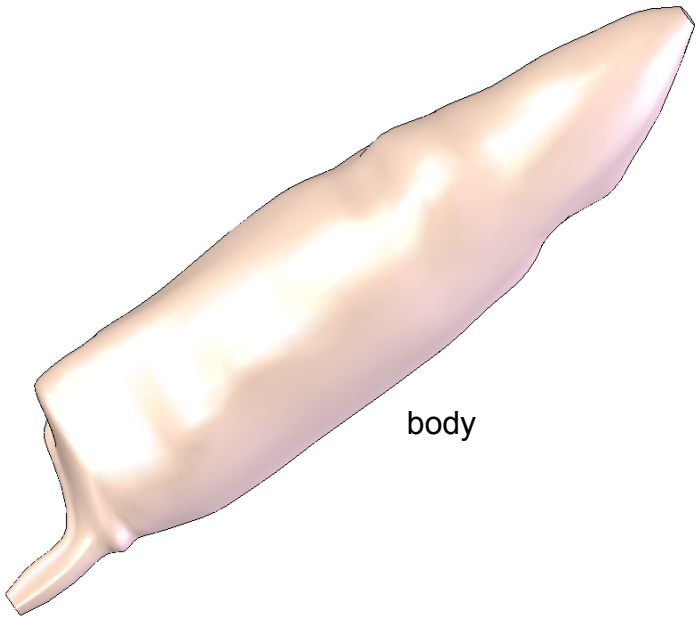

(a)

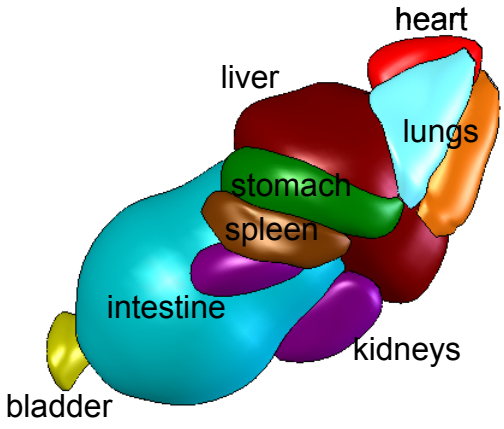

(b)

Figure 47: Schematic of (a) the mouse body and (b) the internal organs used in the virtual mouse phantom.

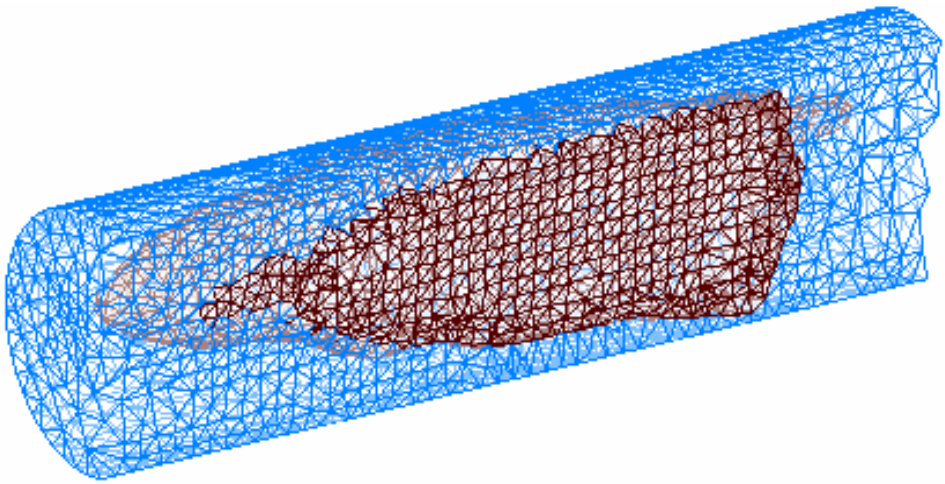

Figure 48: Mouse mesh used to generate the synthetic mouse data used to test the small animal reconstruction algorithm. A portion of the mesh was cut away to demonstrate the quality of the internal mesh.

attenuation of the excitation and fluorescent light through the gut. Each source and detector was modeled with a numerical aperture of 0.39 using the FSDS and integral transport techniques on a triangular Chebyschev-Legendre quadrature with S_N=6 and a scattering degree of 3. The incident light was modulated at 100 MHz. Figure 49 shows an example of how the excitation and emission light propagates through the phantom. As illustrated in Figure 49a, the excitation source must pass through the void-like water region prior to encountering the mouse, simulating a non-contact geometry where the source and detector fibers would be some distance from the surface of a real mouse.

The reconstruction of the fluorescence yield took place on an independent Cartesian mesh. The separate mesh served several purposes, first it prevented the 'inverse crime' where target location information in the forward mesh is passed to the

inverse mesh and also provided a mesh that was easily adaptable allowing the mesh resolution, and hence the number of unknowns, to be adjusted to minimize the ill-posedness of the inverse problem. It is also important to note that the current version of the RTE solver prevents us from performing multiple iterations per reconstruction due to the inability to update the map of fluorescence absorption during computations. Future versions of the solver will eliminate this limitation.

The excitation and emission predictions for each source detector pair were compiled and the bladder reconstructed using equation (78). The Jacobian matrix was calculated using the adjoint solution between each of the detector/source pairs on a homogeneous mouse phantom in which all organ optical properties were set to those of muscle. Figure 50 depicts the iso-surface of the reconstructed fluorescence contour drawn at 50% of the maximum contour level. Also shown is a slice of the fluorescent absorption map.

A second set of synthetic data was also obtained by simulating a 10 nM concentration of ICG in both kidneys of the mouse with no background fluorescence. Excitation and emission predictions were again obtained using the same parameters in the RTE solver as in the previous bladder case. However, this time the five source/detector rings closest to the kidneys were used to obtain the frequency domain data. Figure 51 depicts the iso-surfaces drawn at 50% of the maximum contour level as well as a slice through the fluorescence map.

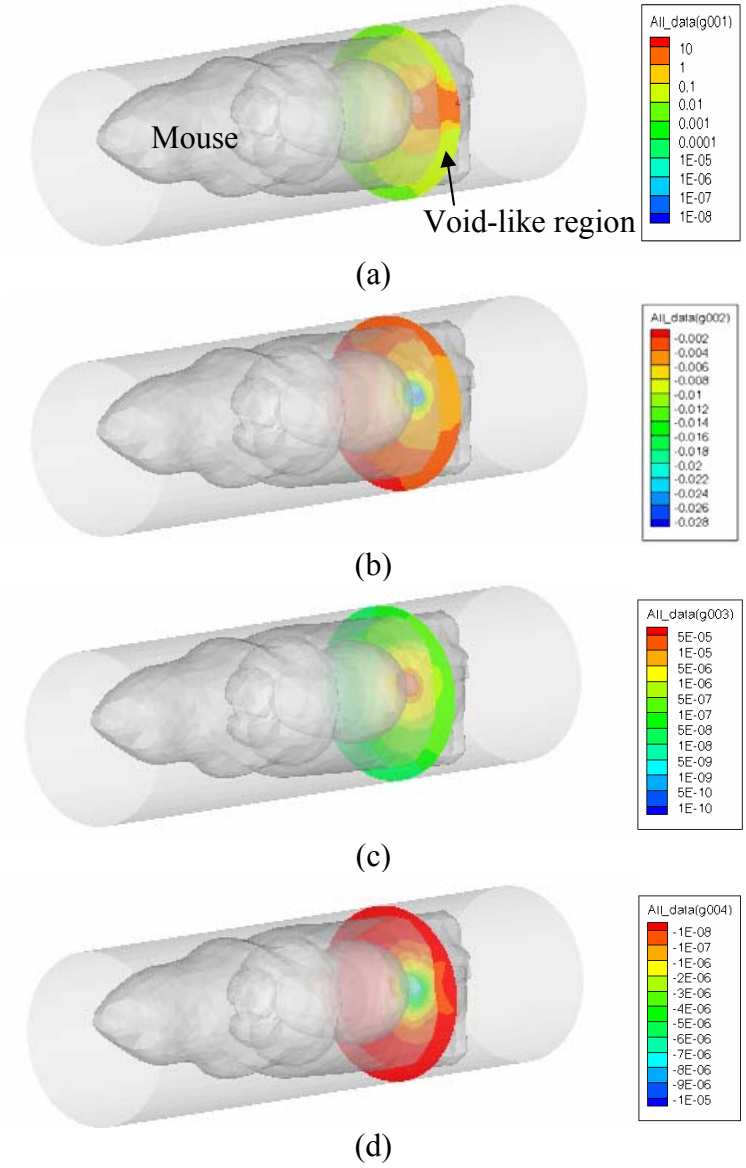

Figure 49: Illustrations depicting the predictions of the forward solution in the plane of an excitation source. (a) and (b) are the real and imaginary components of the complex excitation fluence of the forward solution, and (c) and (d) the real and imaginary components of the complex emission fluence.

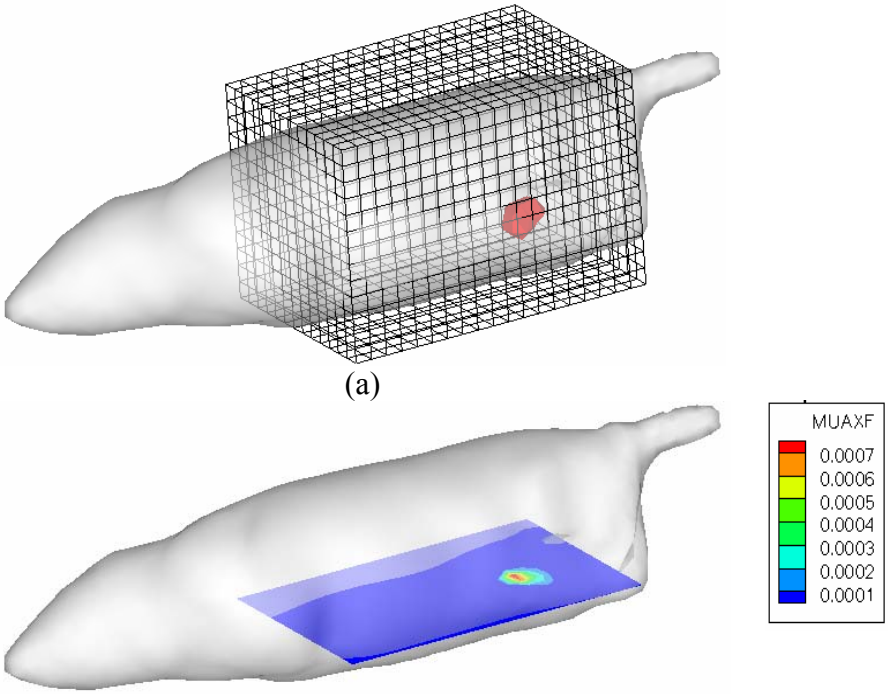

(a)

(b)

Figure 50: Reconstructed fluorescence absorption for a 10 nM concentration of ICG in the bladder. (a) is the iso-surface drawn at 50% of the maximum contour level as well as the reconstruction grid, (b) depicts a slice through the reconstructed fluorescence absorption map.

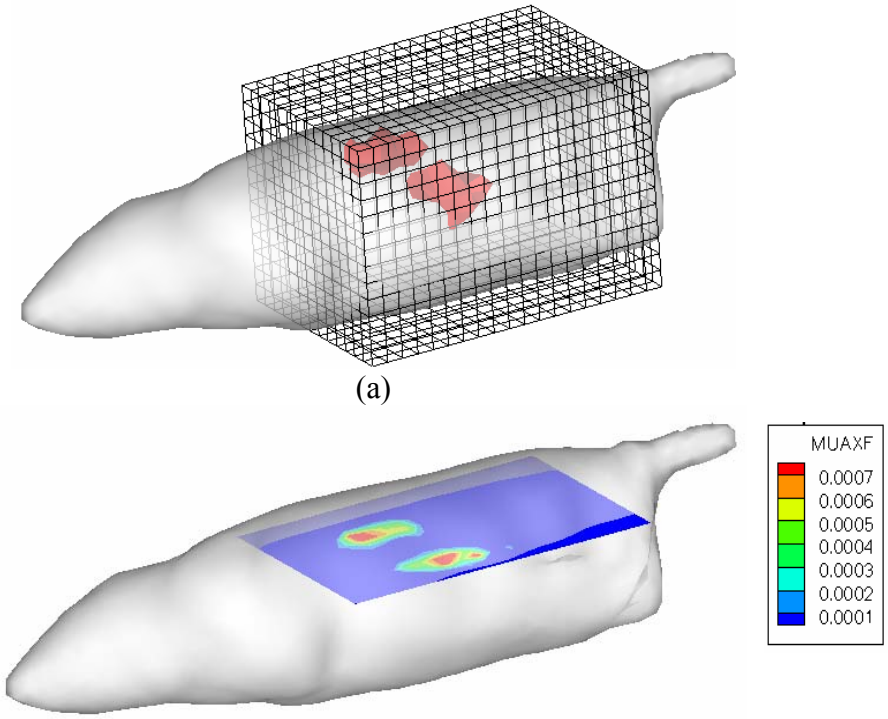

Figure 51: Reconstructed fluorescence absorption for a 10 nM concentration of ICG in the kidneys. (a) is the iso-surface drawn at 50% of the maximum contour level as well as the reconstruction grid, (b) depicts a slice through the reconstructed fluorescence absorption map.

As shown in Figure 50 and Figure 51 the RTE based algorithm can qualitatively reconstruct the location and size of fluorescent heterogeneities. However, the contour value of the reconstructed heterogeneity does not agree with the value of $\mu_{a,xf}$ in the original forward data. It is thought that additional iterations may improve the quantitative reconstruction of the fluorescence absorption map as well as the spatial characteristics of the reconstructed heterogeneities.

Experimental Data

We also wanted to verify that the RTE based reconstruction algorithm could reconstruct fluorescence heterogeneities from real experimental data. To do this, we assembled a new phantom nearly identical the phantoms used previously. However, on this phantom we placed five rings of fibers 5 mm apart in the x = 6.0 cm to x = 4.0 cm planes. The top and bottom rings consisted of twenty detector fibers each. The middle three rings contained both source and detector fibers (20 of each) placed alternately around each ring for a total of 100 detector fibers and 60 source fibers. An optical switch (custom built by LIGHTech Fiberoptics Inc.) was used to switch the 785 nm excitation light from one source to the next. Frequency domain data was obtained for all source/detector pairs using the homodyne ICCD system.

The first data set was obtained on a 0.5% intralipid phantom containing a 1 cm diameter glass sphere filled with a 1 μM ICG solution. The sphere was suspended in the 0.5% intralipid at ~(49, 4, 2,) mm with the z axis going down from the top of the phantom as shown in Figure 52a. The second phantom was also filled with a 0.5% intralipid solution but contained two 3 mm NMR tubes which were filled with a 1 μM ICG solution and placed at ~(4, 2) mm and ~(0, -4.5) mm as shown in Figure 52b.

Simulations were also run using the optical properties listed in Table 2. Figure 53 compares the experimental results of the phantom with the spherical fluorescent ball to those predicted using the RTE solver for the source fiber located at (5.0, -1.25, 0) cm. Figure 54 compares the experimental results of the second phantom containing two fluorescent NMR tubes with those predicted using the RTE solver for the source

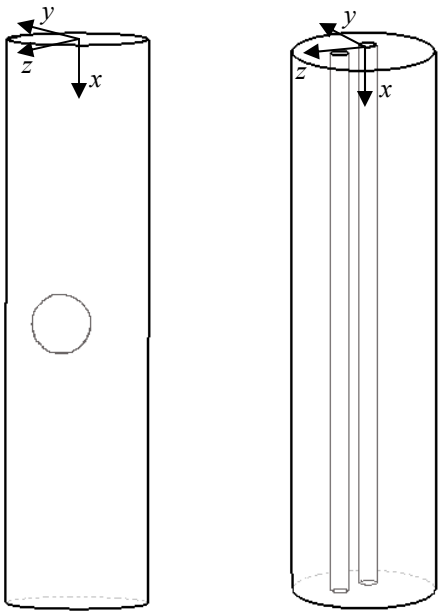

Figure 52: Illustration of the 0.5% intralipid phantoms used to obtain experimental data for tomographic reconstruction. (a) The first phantom contained a 1 cm diameter ball located at ~(49, 4, 2) mm and filled with a 1 μM ICG solution. (b) The second phantom contained two 3 mm diameter NMR tubes located at (y,z) = ~(0, -4.5) mm and ~(2, 4) mm which were also filled with a 1 μM ICG solution.

fiber located at (5.5, -1.25, 0) cm. The peak offsets in the fluorophore amplitude is most likely due to the uncertainty in the target location measurement. The phase measurements show a large amount of noise, particularly for the excitation wavelength.

Our attempts to reconstruct the heterogeneities using the experimental data and the RTE Jacobian sensitivity matrix were unsuccessful. We believe that this is primarily due to the one inverse iteration limit currently imposed by the RTE solver and the high noise floor in the phase data as compared to the simulated data. The solver itself was designed to be used with RTE and diffusion based gradients or

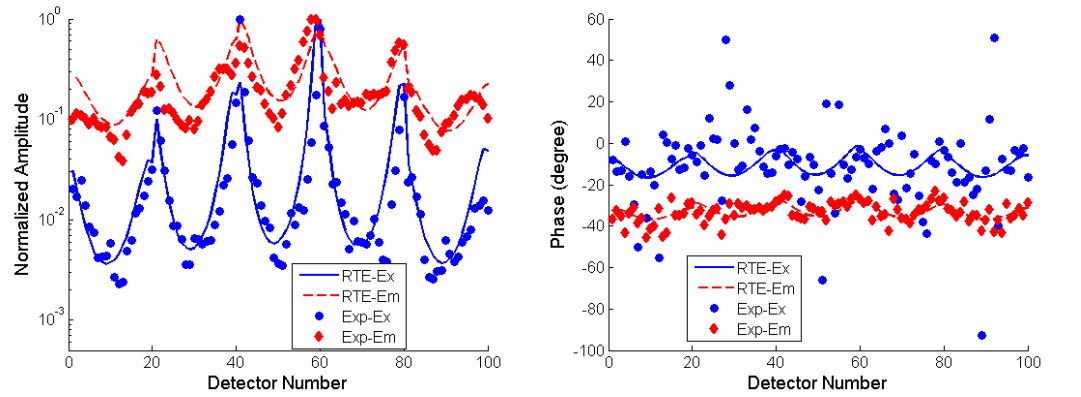

(a) (b)

Figure 53: Comparison of experimental data from phantom containing a 1 cm fluorescent spherical heterogeneity filled with 1 µM ICG. (a) is the normalized amplitude and (b) is the phase. The source fiber is located at (0, -1.25, 5.0) cm.

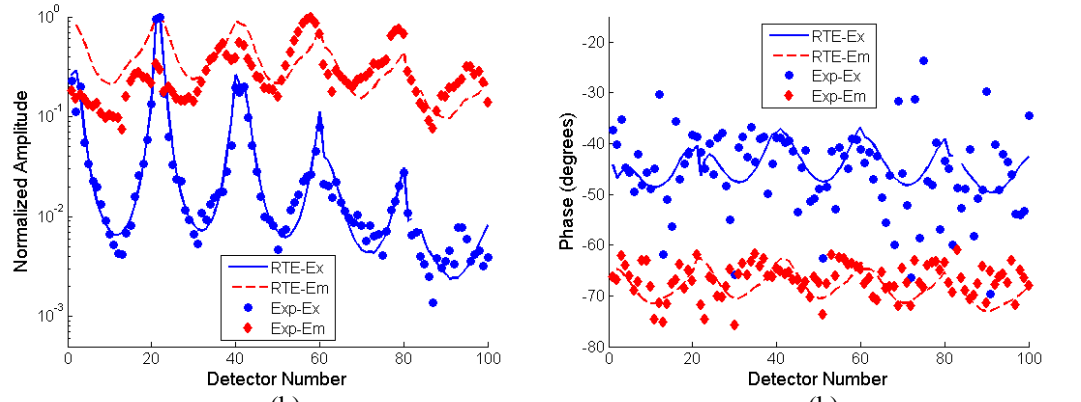

(b) (b)

Figure 54: Comparison of experimental data from phantom containing two 3 mm NMR tubes filled with 1 µM ICG. (a) is the normalized amplitude and (b) is the phase. The source fiber is located at (5.5, -1.25, 0) cm.

Jacobian sensitivity matrices, thus we elected to test the robustness of the solver by incorporating diffusion based gradients and Jacobian matrices. While the diffusion approximation slightly overpredicts the attenuation of excitation light due to the use of an isotropic source (see Figure 43), the information it provides should be similar to that provided by the RTE solver, thus allowing us to test whether additional RTE based iterations will permit the targets to be reconstructed. When non-diffusive optical properties (i.e. real mice and/or non-contact instrument geometries) are used, the diffusion approximation may not provide the needed information for reconstruction, and the gradient or Jacobian obtained from the RTE solver may be necessary.

Figure 55a shows the reconstruction of the spherical target using a diffusion based gradient of the error function (BFGS method). The cut-plane, located near the maximum reconstructed fluorescence absorption, is in the z = 4.0 cm plane, nearly 1 cm higher than the real position. This shift reconstructed bulb location may be due to the lower fluorescence amplitude measured from the lower detector ring (detectors numbers 1-20 in Figure 53). Figure 55b shows the reconstruction of two 3 mm NMR tubes after 30 reconstruction iterations using the same diffusion based gradient of the error function (BFGS method) used for the bulb. The cut-plane in this figure is located at x = 5.2 cm and demonstrates the ability of the reconstruction algorithm to reconstruct multiple targets using frequency-domain experimental measurements.

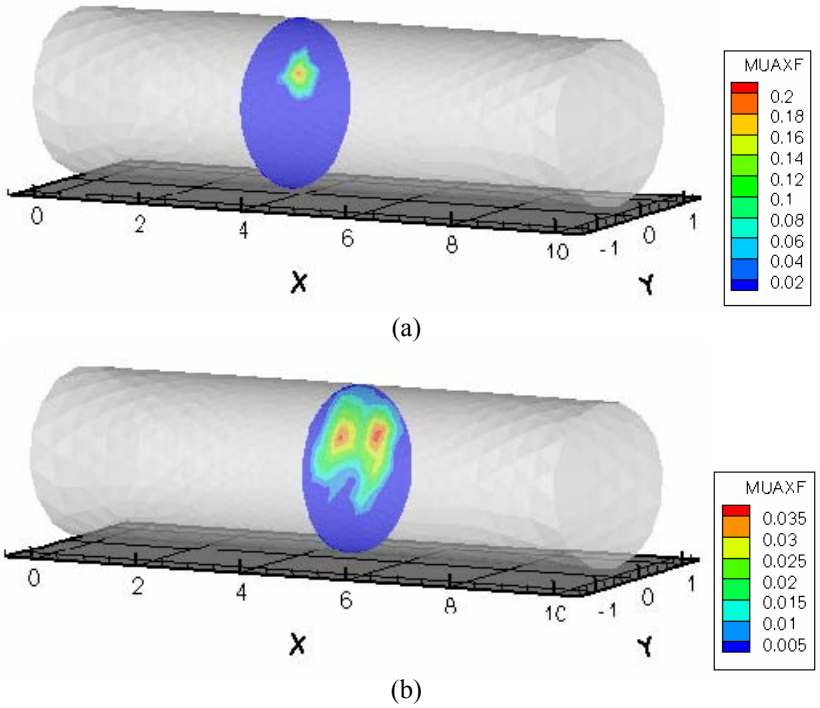

Figure 55: Reconstructed experimental fluorescence maps. (a) a 1 cm diameter bulb containing 1 μM ICG (cutplane at x = 4.0 cm) and (b) two 3 mm NMR tubes containing 1 μM ICG (cutplane at x = 5.2 cm).

Conclusions

In this section we have demonstrated the use of the RTE solver as an integral part of a small animal tomography algorithm. We have successfully reconstructed the location and size of simulated heterogeneities in a virtual mouse phantom. Due to the one iteration limit of the current version of the RTE solver, we were unable to reconstruct the real experimental data. However because the experimental data was obtained using marginally diffusive optical properties, additional studies in which the RTE inverse information was substituted with diffusion information were performed. The successful reconstruction of the experimental data using the diffusion information

and multiple iterations indicate that reconstructions of experimental data with additional RTE iterations should also be successful.

VIII. SUMMARY, CONCLUSIONS, AND FUTURE WORK

Molecular medicine, which may be individualized for each patient holds great promise for the future of medicine. However, the time and costs of associated with the timely discovery and marketing of new drugs is prohibitive. Small animal optical tomography may provide a quicker more cost effective way to screen and evaluate the efficacy of potential molecular drugs. However, the small volumes and absorptive properties of mice may inhibit the use of more established diffusion based optical tomography algorithms. This dissertation addresses the development of the instrumentation and associated algorithms which may provide more accurate small animal tomographic reconstructions for future application in drug discovery. The highlights of this work include:

1. As compared to continuous wave measurements, time dependent optical measurements include time of flight or phase information which can be incorporated into a tomographic algorithm thereby increasing the accuracy of the reconstruction. In this dissertation, we constructed an intensified CCD camera system designed to permit the collection of fluorescence-enhanced frequency-domain measurements from multiple locations around a small imaging tube of a suitable size for imaging mice. An optical switch was also incorporated into the design to permit the rapid switching of the modulated excitation light from one source optical fiber to another.
2. While the diffusion approximation has been widely used in optical tomography, there is some question concerning its validity in small animals

due to their small volumes and non-diffusive optical properties. The radiative transport equation (RTE) is the general equation which describes the transport of light through all types of media. Through collaboration with Transpire, Inc., we have developed the first documented RTE based solver which can solve the coupled fluorescence RTE equations in the frequency domain. This solver incorporates discrete ordinate techniques, source iteration with modified diffusion synthetic acceleration, and linear discontinuous finite element differencing methods to accurately predict the excitation and emission fluence across complex, unstructured meshes. These techniques, with the implementation of the first scattered distributed source and integral transport methods, enable the RTE solver to accurately predict photon fluence in both the diffusion and transport limits.

3. The RTE solver was validated to verify that its fluence predictions corresponded with widely accepted photon path prediction techniques such as diffusion and Monte Carlo in both the diffusion and transport limits. The solver was also validated against real frequency-domain data obtained using the fluorescence imaging system and a variety of phantoms. Typical errors between the RTE predictions and the experimental data were less than 8% for amplitude and 7% for phase.
4. To test the ability to perform reconstructions using the RTE solver as a forward model in a tomographic algorithm, synthetic data was generated using a virtual mouse. The mouse contained most of the major organs associated with the

trunk and the optical properties of each organ as determined from the literature were used. Single and dual fluorescent heterogeneities were successfully reconstructed in one iteration of the RTE forward solver. Tomographic experimental data was also obtained, using the ICCD system. However, the RTE based algorithm did not reconstruct the fluorescent heterogeneities due to the inability to perform more than one reconstruction iteration with the current version of the RTE solver. Because the experimental conditions were marginally diffusive, and the RTE and diffusion predictions should be comparable, we substituted a diffusion based forward model for the RTE model and successfully reconstructed the heterogeneities after several iterations. This indicates that the RTE solver should provide sufficient information when adapted for use directly with reconstruction algorithm.

Recommendations for future work include:

1. Further development needs to be done to adapt the instrumentation for use on live mice. While the use of fiber optic cables enables one to collect data from all sides of the mouse at once, they are bulky and if not perfectly aligned can introduce error in the measurements. An open system in which the entire mouse is within the view of the camera would significantly increase the amount of useful data for reconstruction, as well as increase the usability of the system in animal studies. Further work should also be done on ways to improve the phase data from the ICCD instrument such that the time-dependent information is more useful in reconstruction.

2. Further development is also needed on the RTE solver. For the solver to be more accurate particularly in open optical systems where tissue/air interfaces are present, Snell's law, which describes the propagation of photons across material interfaces, must be incorporated. Another significant modification that must be implemented is the ability to update the fluorescence optical map between iterations in the reconstruction algorithm. This would enable the RTE based solver to reconstruct heterogeneities that require multiple iterations to resolve.
3. Additional work on the reconstruction algorithm, such as the way in which the adjoint solutions to the RTE solver are generated and used may also reduce the computational requirements of the algorithm and improve the speed of the reconstruction.

REFERENCES

1. P. Landers, "Cost of developing a new drug increases to about $1.7 billion," The Wall Street Journal, December 8, 2003.

2. S. Kwon, S. Ke, M. Gurfinkel, W. Wang, Q. Wu, C. Li, and E. M. Sevick-Muraca, "Dose-dependent uptakes of an RGD-fluorescent dye-targeted to αvβ3 receptor expressed Kaposi's Sarcoma," Journal of Molecular Imaging, **4,** 75-88 (2005)

3. D. W. Holdsworth and M. M. Thornton, "Micro-CT in small animal and specimen imaging," Trends Biotechnol., **20,** S24-S39 (2002)

4. S. Robinson, A. Suomalainen, and M. Kortesniemi, "μ-CT," Eur. J. Radiol., **56,** 185-191 (2005)

5. B. M. Damon and J. C. Gore, "Biophysical basis of magnetic resonance imaging of small animals," Methods Enzymol., **385,** 19-40 (2004)

6. A. Heerschap, M. G. Sommers, H. J. A. i. t. Zandt, W. K. J. Renema, A. A. Veltien, and D. W. J. Klomp, "Nuclear magnetic resonance in laboratory animals," Methods Enzymol., **385,** 41-63 (2004)

7. F. S. Foster, M. Y. Zhang, Y. Q. Zhou, G. Liu, J. Mehi, E. Cherin, K. A. Harasiewicz, B. G. Starkoski, L. Zan, D. A. Knapik, and S. L. Adamson, "A new ultrasound instrument for in vivo microimaging of mice," Ultrasound in Medicine & Biology, **28,** 1165-1172 (2002)

8. M. V. Green, J. Seidel, J. J. Vaquero, E. Jagoda, I. Lee, and W. C. Eckelman, "High resolution PET, SPECT and projection imaging in small animals," Comput. Med. Imaging Graph., **25,** 79-86 (2001)

9. R. Lecomte, "Technology challenges in small animal PET imaging," Nuclear Instruments and Methods in Physics Research Section A: Accelerators, Spectrometers, Detectors and Associated Equipment, **527,** 157-165 (2004)

10. S. I. Ziegler, "Positron emission tomography: principles, technology, and recent developments," Nucl. Phys. A, **752,** 679-687 (2005)

11. Y. Yang, Y.-C. Tai, S. Siegel, D. F. Newport, B. Bai, Q. Li, R. M. Leahy, and S. R. Cherry, "Optimization and performance evaluation of the microPET II scanner for in vivo small-animal imaging," Phys. Med. Biol., **49,** 1527-2545 (2004)

12. A. H. Hielscher, "Optical tomographic imaging of small animals," Curr. Opin. Biotechnol., **16,** 79-88 (2005)

13. D. J. Hawrysz and E. M. Sevick-Muraca, "Developments toward diagnostic breast cancer imaging using near-infrared optical measurements and fluorescent contrast agents," Neoplasia, **2,** 388-417 (2000)

14. S. Ke, W. X., M. Gurfinkel, C. Charnsangavej, S. Wallace, E. M. Sevick-Muraca, and C. Li, "Near-infrared optical imaging of epidermal growth factor receptor in breast cancer xenografts," Cancer Res., **63,** 7870-7875 (2003)

15. A. Becker, C. Hessenius, K. Licha, B. Ebert, U. Sukowski, W. Semmler, B. Wiedenmann, and C. Grotzinger, "Receptor-targeted optical imaging of tumors with near-infrared fluorescent ligands," Nat. Biotechnol., **19,** 327-331 (2001)

16. J. Bugaj, S. Achilefu, R. Dorshow, and R. Rajogopalan, "Novel fluorescent contrast agents for optical imaging of in vivo tumors based on a receptor-targeted dye-peptide conjugate platform," J. Biomed. Opt., **6,** 122-133 (2001)

17. E. M. Sevick-Muraca, J. P. Houston, and M. Gurfinkel, "Florescence-enhanced, near infrared diagnostic imaging with constrast agents," Curr. Opin. Chem. Biol., **6,** 642-650 (2002)

18. B. H. Hasegawa, William C. Barber, Tobias Funk, Andrew B. Hwang, Carmen Taylor, Mingshan Sun and Youngho Seo, "Implementation and applications of dual-modality imaging," Nuclear Instruments and Methods in Physics Research Section A: Accelerators, Spectrometers, Detectors and Associated Equipment, **525,** 236-241 (2004)

19. B. H. Hasegawa, K. Iwata, K. H. Wong, M. C. Wu, A. J. Da Silva, H. R. Tang, W. C. Barber, A. H. Hwang, and A. E. Sakdinawat, "Dual-modality imaging of function and physiology," Acad. Radiol., **9,** 1305-1321 (2002)

20. L. V. Wang, "Ultrasound-mediated biophotonic imaging: A review of acousto-optical tomography and photo-acoustic tomography," Dis. Markers, **19,** 123-138 (2003,2004)

21. A. Y. Bluestone, G. Abdoulaev, C. H. Schmitz, R. L. Barbour, and A. H. Hielscher, "Three-dimensional optical tomography of hemodynamics in the human head," Optics Express, **9,** 272-286 (2001)

22. A. Y. Bluestone, M. Stewart, J. Lasker, G. S. Abdoulaev, and A. H. Hielscher, "Three-dimensional optical tomographic brain imaging in small animals, part 1: hypercapnia," J. Biomed. Opt., **9,** 1046-1062 (2004)

23. A. Y. Bluestone, M. Stewart, B. Lei, I. S. Kass, J. Lasker, G. S. Abdoulaev, and A. H. Hielscher, "Three-dimensional optical tomographic brain imaging in small animals, part 2: Unilateral carotid occlusion," J. Biomed. Opt., **9,** 1063-1073 (2004)

24. H. W. Lim and N. A. Soter, *Clinical Photomedicine*. (Marcel Dekker, New York, 1993).

25. X. Gu, Q. Zhang, L. Larcom, and H. Jiang, "Three-dimensional bioluminescence tomography with model-based reconstruction," Optics Express, **12,** 3996-4000 (2004)

26. E. Hecht, *Optics*. 4 ed. (Addison Wesley, San Francisco, 2002).

27. J. R. Mourant, J. P. Freyer, A. H. Hielscher, A. A. Eick, D. Shen, and T. M. Johnson, "Mechanisms of light scattering from biological cells relevant to noninvasive optical-tissue diagnostics," Appl. Opt., **37,** 3586-3593 (1998)

28. B. W. Pogue, S. P. Poplack, T. O. McBride, W. A. Wells, K. S. Osterman, U. L. Osterberg, and K. D. Paulsen, "Quantitative hemoglobin tomography with

diffuse near-infrared spectroscopy: pilot results in the breast," Radiology, **218,** 261-266 (2001)

29. A. H. Hielscher, A. D. Klose, A. K. Scheel, B. Moa-Anderson, M. Backhaus, U. Netz, and J. u. Beuthan, "Sagittal laser optical tomography for imaging of rheumatoid finger joints," Phys. Med. Biol., **49,** 1147-1163 (2004)

30. J. P. Houston, S. Ke, W. Wang, C. Li, and E. M. Sevick-Muraca, "Quality analysis of in vivo near-infrared fluorescence and conventional gamma images acquired using a dual-labeled tumor-targeting probe," J. Biomed. Opt., **10,** 054010 (2005)

31. K. Hwang, J. P. Houston, J. C. Rasmussen, A. Joshi, S. Ke, C. Li, and E. M. Sevick-Muraca, "Improved excitation light rejection enhances small animal fluorescent optical imaging," Molecular Imaging, **4,** 194-204 (2005)

32. J. J. Duderstadt and L. J. Hamilton, *Nuclear Reactor Analysis*. (John Wiley & Sons, New York, 1976).

33. E. E. Lewis and W. F. Miller, *Computational Methods of Neutron Transport*. (John Wiley & Sons, New York, 1984).

34. E. W. Larsen, J. E. Morel, and W. F. Miller, "Asymptotic solutions of numerical transport problems in optically thick, diffusive regions," J. Comput. Phys., **69,** 283-324 (1987)

35. E. W. Larsen and J. E. Morel, "Asymptotic solutions of numerical transport problems in optically thick, diffusive regions II," J. Comput. Phys., **91,** 246 (1990)

36. A. D. Klose, V. Ntziachristos, and A. H. Hielscher, "The inverse source problem based on the radiative transfer equation in optical molecular imaging," J. Comput. Phys., **202,** 323-345 (2005)

37. A. D. Klose and A. H. Hielscher, "Fluorescence tomography with simulated data based on the equation of radiative transfer," Opt. Lett., **28,** 1019-1021 (2003)

38. K. Ren, G. S. Abdoulaev, G. Bal, and A. H. Hielscher, "Algorithm for solving the equation of radiative transfer in the frequency domain," Opt. Lett., **29,** 578-580 (2004)

39. M. L. Adams, T. A. Wareing, and W. F. Walters, "Characteristic methods in thick diffusive problems," Nucl. Sci. Eng., **130,** 18-46 (1998)

40. A. H. Hielscher, R. E. Alcouffe, and R. L. Barbour, "Comparison of finite-difference transport and diffusion calculations for photon migration in homogeneous and heterogeneous tissues," Phys. Med. Biol., **43,** 1285-1302 (1998)

41. J. E. Morel, "A synthetic acceleration method for discrete ordinates calculations with highly anisotropic scattering," Nucl. Sci. Eng., **82,** 34-42 (1982)

42. S. L. Jacques and L. Wang, "Monte Carlo modeling of light transport in tissues", in *Optical-Thermal Response of Laser-Irradiated Tissue*, edited by A.J. Welch and M.J.C. van Gemert. Plenum Press, New York, 1995, pp. 73-100.

43. L. V. Wang, S. L. Jacques, and L. Zheng, "MCML – Monte Carlo modeling of light transport in multi-layered tissues," Comput. Methods Programs Biomed., **47,** 131-146 (1995)

44. A. Godavarty, D. J. Hawrysz, R. Roy, E. M. Sevick-Muraca, and M. J. Eppstein, "Influence of the refractive index-mismatch at the boundaries measured in fluorescence-enhanced frequency-domain photon migration imaging," Optics Express, **10,** 653-662 (2002)

45. R. C. Haskell, L. O. Svaasand, T.-T. Tsay, T.-C. Feng, M. S. McAdams, and B. J. Tromberg, "Boundary conditions for the diffusion equation in radiative transfer," J. Opt. Soc. Am. A, **11,** 2727-2741 (1994)

46. W.-F. Cheong, S. A. Prahl, and A. J. Welch, "A review of the optical properties of biological tissues," IEEE J. Quantum Electron., **26,** 2166-2185 (1990)

47. *Merriam-Webster's Medical Dictionary*. (cited May 19, 2005); from Dictionary.com website: http://dictionary.reference.com/browse/tomography.

48. J. Hsieh, *Computed Tomography: Principles, Design, Artifacts, and Recent Advances*. (SPIE Press, Bellingham, WA, 2003).

49. A. C. Kak and M. Slaney, *Principles of Computerized Tomographic Imaging*. (IEEE Press, New York, 1988).

50. S. B. Colak, G. W. t Hooft, D. G. Papaioannou, and M. B. van der Mark, "3D backprojection tomography for medical optical imaging", in *OSA TOPS on Advances in Optical Imaging and Photon Migration*, edited by R.R.a.J.G.F. Alfana. Optical Society of America, 1996, pp. 294-298.

51. S. B. Colak, D. G. Papaioannou, G. W. t Hooft, M. B. van der Mark, H. Schomberg, J. C. J. Paasschens, J. B. M. Melissen, and N. A. A. J. van Asten, "Tomographic image reconstruction from optical projections in light-diffusing media," Appl. Opt., **36,** 180-213 (1997)

52. C. L. Matson and H. Liu, "Backprojection in turbid media," J. Opt. Soc. Am. A, **16,** 1254-1265 (1999)

53. S. A. Walker, S. Fantini, and E. Gratton, "Image reconstruction by backprojection from frequency-domain optical measurements in highly scattering media," Appl. Opt., **36,** 170-174 (1997)

54. S. R. Arridge, "Optical tomography in medical imaging," Inverse Problems, **15,** R41-R93 (1999)

55. J. C. Rasmussen, A. Joshi, T. Pan, E. M. Sevick-Muraca, T. Wareing, and J. McGhee, "Radiative transport in fluorescence-enhanced frequency domain photon migration," Med. Phys., Accepted for publication**,** (2006)

56. A. D. Klose and A. H. Hielscher, "Iterative reconstruction scheme for optical tomography based on the equation of radiative transfer," Med. Phys., **26,** 1698-1707 (1999)

57. A. D. Klose and A. H. Hielscher, "Optical tomography using the time-independent equation of radiative transfer - Part 1: forward model," J. Quant. Spectrosc. Radiat. Transfer, **72,** 691-713 (2002)

58. A. D. Klose and A. H. Hielscher, "Optical tomography using the time-independent equation of radiative transfer - Part 2: inverse model," J. Quant. Spectrosc. Radiat. Transfer, **72,** 715-732 (2002)

59. V. Ntziachristos and R. Weissleder, "Experimental three-dimensional fluorescence reconstruction of diffuse media by use of a normalized Born approximation," Opt. Lett., **26,** 893-895 (2001)

60. G. S. Abdoulaev and A. H. Hielscher, "Three-dimensional optical tomography with the equation of radiative transfer," Journal of Electronic Imaging, **12,** 594-601 (2003)

61. J. P. Culver, T. Durduran, D. Furuya, C. Cheung, J. H. Greenberg, and A. G. Yodh, "Diffuse optical tomography of cerebral blood flow, oxygenation, and metabolism in rat during focal ischemia," J Cereb Blood Flow Metab, **23,** 911-924 (2003)

62. C. Das, A. Trivedi, K. Mitra, and T. Vo-Dinh, "Short pulse laser propagation through tissues for biomedical imaging," J. Phys. D: Appl. Phys., **36,** 1714-1721 (2003)

63. C. Das, A. Trivedi, K. Mitra, and T. Vo-Dinh, "Experimental and numerical analysis of short-pulse laser interaction with tissue phantoms containing inhomogeneities," Appl. Opt., **42,** 5173-5180 (2003)

64. J. Ripoll and V. Ntziachristos, "Iterative boundary method for diffuse optical tomography," J. Opt. Soc. Am. A, **20,** 1103-1110 (2003)

65. R. B. Schultz, J. Ripoll, and V. Ntziachristos, "Noncontact optical tomography of turbid media," Opt. Lett., **28,** 1701-1703 (2003)

66. R. B. Schultz, J. Ripoll, and V. Ntziachristos, "Experimental fluorescence tomography of tissues with noncontact measurements," IEEE Trans. Med. Imaging, **23,** 492-500 (2004)

67. A. D. Kim and M. Moscoco, "Beam propagation in sharply peaked forward scattering media," J. Opt. Soc. Am. A, **21,** 797-803 (2004)

68. A. D. Kim, "Transport theory for light propagation in biological tissue," J. Opt. Soc. Am. A, **21,** 820-827 (2004)

69. H. Quan and Z. Guo, "Fast 3-D optical imaging with transient fluorescence signals," Optics Express, **12,** 449-457 (2004)

70. G. S. Abdoulaev, K. Ren, and A. H. Hielscher, "Optical tomography as a PDE-constrained optimization problem," Inverse Problems, **21,** 1507-1530 (2005)

71. S. V. Patwardhan, S. R. Bloch, S. Achilefu, and J. P. Culver, "Time-dependent whole-body fluorescence tomography of probe bio-distributions in mice," Optics Express, **13,** 2564-2577 (2005)

72. G. M. Turner, G. Zacharakis, A. Soubret, J. Ripoll, and V. Ntziachristos, "Complete-angle projection diffuse optical tomography by use of early photons," Opt. Lett., **30,** 409-411 (2005)

73. H. Xu, R. Springett, H. Dehghani, B. W. Pogue, K. D. Paulsen, and J. F. Dunn, "Magnetic-resonance-imaging coupled broadband near-infrared tomography system for small animal brain studies," Appl. Opt., **44,** 2177-2188 (2005)

74. J. S. Reynolds, T. L. Troy, and E. M. Sevick-Muraca, "Multi-pixel techniques for frequency-domain photon migration imaging," Biotechnol. Prog., **13,** 669-680 (1997)

75. A. B. Thompson and E. M. Sevick-Muraca, "NIR fluorescence contrast-enhanced imaging with ICCD homodyne detection: measurement precision and accuracy," J. Biomed. Opt., **8,** 111-120 (2003)

76. "Introduction to Image Intensifiers for Scientific Imaging," Roper Scientific Technical Notes, (Roper Scientific, New Jersey, 2002).

77. Z. Sun, Y. Huang, and E. M. Sevick-Muraca, "Precise analysis of frequency domain migration measurement for characterization of concentrated colloidal suspensions," Rev. Sci. Instrum., **73,** 383-393 (2002)

78. K. Urbanska, B. Romanowska-Dixon, Z. Matuszak, J. Oszajca, P. Nowak-Sliwinska, and G. Stochel, "Indocyanine green as a prospective sensitizer for photodynamic therapy of melanomas," Acta Biochemica Polonica, **49,** 387-391 (2002)

79. J. M. McGhee, T. A. Wareing, and D. A. Barnett Jr., *Attila Version 5: User's Manual*. (Transpire Inc., January 23, 2006).

80. T. A. Wareing, J. M. McGhee, J. E. Morel, and S. D. Pautz, "Discontinuous finite element Sn methods on three-dimensional unstructured grids," Nucl. Sci. Eng., **138,** 256-268 (2001)

81. M. L. Adams and E. W. Larsen, "Fast iterative methods for discrete-ordinates particle transport calculations," Process in Nuclear Energy, **40,** 3-159 (2002)

82. T. A. Wareing, *Asymptotic Diffusion Accelerated Discontinuous Finite Element Methods for Transport Problems*. a Ph.D. Dissertation in the Dept. of Nuclear Engineering. (University of Michigan at Ann Arbor, 1992).

83. K. Vishwanath, B. W. Pogue, and M.-A. Mycek, "Quantitative fluorescence lifetime spectroscopy in turbid media: comparison of theoretical, experimental, and computational methods," Phys. Med. Biol., **47,** 3387-3405 (2002)

84. T. Pan, J. C. Rasmussen, J. H. Lee, and E. M. Sevick-Muraca, "Diffusion, radiative transport, and Monte Carlo simulation of fluorescence generation and propagation for small animal imaging.," Med. Phys., Submitted 2006**,**

85. E. M. Sevick-Muraca, G. Lopez, T. L. Troy, J. S. Reynolds, and C. L. Hutchinson, "Fluorescence and absorption contrast mechanisms for biomedical optical imaging using frequency domain techniques," Photochem. Photobiol., **66,** 55-64 (1997)

86. A. Godavarty, *Fluorescence enhanced optical tomography on breast phantoms with measurements using a gain modulated intensified CCD imaging system*. a Ph.D. Dissertation in the Dept. Chemical Engineering. (Texas A&M University, College Station, TX, 2003).

87. J. N. Reddy, *An Introduction to the Finite Element Method*. 2 ed. (McGraw-Hill, New York, 1993).

88. K. Hwang, T. Pan, A. Joshi, J. C. Rasmussen, and E. M. Sevick-Muraca, "Influence of excitation light rejection on forward model mismatch in optical tomography," Phys. Med. Biol., Accepted for Publication**,** (2006)

89. S. Jiang, B. W. Pogue, T. O. McBride, and K. D. Paulsen, "Quantitative analysis of near-infrared tomography: sensitivity to the tissue-simulating precalibration phantom," J. Biomed. Opt., **8,** 308-315 (2003)

90. X. Li, B. Chance, and A. G. Yodh, "Fluorescent heterogeneities in turbid media: limits for detection, characteristic comparison with absorption," Appl. Opt., **37,** 6833-6844 (1998)

91. M. A. O'Leary, D. A. Boas, B. Chance, and A. G. Yodh, "Experimental images of heterogeneous turbid media by frequency-domain diffusing-photon tomography," Opt. Lett., **20,** 426-428 (1995)

92. S. Srinivasan, B. W. Pogue, B. Brooksby, S. Jiang, H. Dehghani, C. Kogel, W. A. Wells, S. P. Poplack, and K. D. Paulsen, "Near-infrared characterization of breast tumors *in vivo* using spectrally-constrained reconstruction," Technology in Cancer Research & Treatment, **4,** 513-526 (2005)

93. D. A. Benaron, S. R. Hintz, A. Villringer, D. Boas, A. Kleinschmidt, J. Frahm, C. Hirth, H. Obrig, J. C. van Houten, E. L. Kermit, W.-F. Cheong, and D. K. Stevenson, "Noninvasive functional imaging of human brain using light," J Cereb Blood Flow Metab, **20,** 469-477 (2000)

94. H. Dehghani, B. W. Pogue, S. P. Poplack, and K. D. Paulsen, "Multiwavelength three-dimensional near-infrared tomography of the breast: initial simulation, phantom, and clinical results," Appl. Opt., **42,** 135-145 (2003)

95. A. Godavarty, M. J. Eppstein, C. Zhang, and E. M. Sevick-Muraca, "Detection of multiple targets in breast phantoms using fluorescence enhanced optical imaging," Radiology, **235,** 148-154 (2005)

96. A. Joshi, W. Bangerth, K. Hwang, J. C. Rasmussen, and E. M. Sevick-Muraca, "Plane wave fluorescence tomography with adaptive finite elements," Opt. Lett., **31,** 193-195 (2006)

97. S. B. Colak, M. B. van der Mark, G. W. 't Hooft, J. H. Hoogenraad, E. S. va der Linden, and F. A. Kuijpers, "Clinical optical tomography and NIR spectroscopy for breast cancer detection," IEEE J. Sel. Top. Quantum Electron., **5,** 1143-1158 (1999)

98. V. Ntziachristos, A. G. Yodh, M. D. Schnall, and B. Chance, "MRI-guided diffuse optical spectroscopy of malignant and benign breast lesions," Neoplasia, **4,** 347-354 (2002)

99. A. Ishimaru, *Wave Propagation and Scattering in Random Media*. (Academic, San Diego, 1978).

100. K. M. Yoo, F. Liu, and R. R. Alfano, "When does the diffusion approximation fail to describe photon transport in random media?," Phys. Rev. Lett., **64,** 2647-2650 (1990)

101. S. Chandrasekhar, *Radiative Transfer*. (Dover, 1960).

102. A. Godavarty, Eva M. Sevick-Muraca, and Margaret J. Eppstein, "Three-dimensional fluorescence lifetime tomography," Med. Phys., **32,** 992-1000 (2005)

103. A. Joshi, *Adaptive finite element methods for fluorescence enhanced optical tomography*. a Ph.D. in the Department of Chemical Engineering. (Texas A&M University, College Station, 2005).

104. W. P. Segars, B. M. W. Tsui, E. C. Frey, G. A. Johnson, and S. S. Berr, "Development of a 4-D digital mouse phantom for molecular imaging research," Molecular Imaging and Biology, **6,** 149-159 (2004)

VITA

NAME:	John C. Rasmussen
Address:	Department of Radiology, Baylor College of Medicine, One Baylor Plaza, Houston, TX 77030
Email Address:	johnras@gmail.com
Education:	B.S., Chemical Engineering, The University of Oklahoma, 2000 PH.D. Chemical Engineering, Texas A&M University, 2006